

# Nanoscale thin-body MOSFET design and applications

*Sriram Balasubramanian*



Electrical Engineering and Computer Sciences  
University of California at Berkeley

Technical Report No. UCB/EECS-2006-138

<http://www.eecs.berkeley.edu/Pubs/TechRpts/2006/EECS-2006-138.html>

October 29, 2006

Copyright © 2006, by the author(s).  
All rights reserved.

Permission to make digital or hard copies of all or part of this work for personal or classroom use is granted without fee provided that copies are not made or distributed for profit or commercial advantage and that copies bear this notice and the full citation on the first page. To copy otherwise, to republish, to post on servers or to redistribute to lists, requires prior specific permission.

Nanoscale thin-body MOSFET design and applications

by

Sriram Balasubramanian

B.Tech. (Indian Institute of Technology, Madras) 1998

M.S. (University of California, Berkeley) 2002

A dissertation submitted in partial satisfaction of the

requirements for the degree of

Doctor of Philosophy

in

Engineering – Electrical Engineering  
and Computer Sciences

in the

GRADUATE DIVISION

of the

UNIVERSITY OF CALIFORNIA, BERKELEY

Committee in charge:

Professor Tsu-Jae King Liu, Chair

Professor Borivoje Nikolic'

Professor Eugene Haller

Fall 2006

The dissertation of Sriram Balasubramanian is approved:

---

Chair	Date
-------	------

---

	Date
--	------

---

	Date
--	------

University of California, Berkeley

Fall 2006

Nanoscale thin-body MOSFET design and applications

Copyright 2006

by

Sriram Balasubramanian

# ABSTRACT

Nanoscale thin-body MOSFET design and applications

by

Sriram Balasubramanian

Doctor of Philosophy in Engineering – Electrical Engineering and Computer Sciences

University of California, Berkeley

Professor Tsu-Jae King Liu, Chair

The silicon-based microelectronics industry has been growing rapidly for the past four decades following Moore's law of scaling. However, fundamental physical limits have heralded the end of conventional linear scaling of transistor dimensions, and a new era of MOSFET scaling constrained by power dissipation and process-induced variations is already here. Fundamental changes in device architecture may be necessary to continue scaling trends with thin-body MOSFETs such as UTB-FETs and FinFETs emerging as leading contenders. This dissertation has addressed many of the key scaling issues involved in the design and performance optimization of thin-body MOSFETs, and highlights applications that take advantage of these projected benefits.

Given the difficulties in shrinking transistor dimensions, application-specific device optimization becomes critical for maximizing the benefits in transitioning to these new transistor designs. In this work, the device optimization methodology has been detailed to optimize thin-body FET performance taking into account circuit performance implications such as power, speed and robustness to process-induced variations through

the use of device simulation and mathematical modeling to better understand the degree of performance enhancement that can be provided by these new device structures.

Back-gated thin-body MOSFETs (BG-FETs) with the capability of dynamic  $V_{TH}$  control have great promise in controlling power dissipation as well as in compensating for process-induced variations. The gate delay versus energy consumption tradeoffs study shows that adaptive  $V_{TH}$  control in BG-FETs makes them span a wider range in energy-delay space over FinFETs. To further refine the design of BG-FETS, a back-gate bias dependent scale length has been derived and shows that reverse-back gate biasing can be used to extend the scalability of the BG-FET.

Designing large SRAM arrays is getting harder due to lowered cell stability with technology scaling and increased degree of process-induced variations. FinFET-based SRAM designs exhibit improved cell stability and can help continue SRAM scaling into sub-45nm technology nodes. A new FinFET-based SRAM cell design with dynamic feedback is shown to provide significant improvement in cell static noise margin, without area or leakage penalty. Process modules required to integrate these SRAM designs such as resist planarization, etch-back and selective gate separation have been demonstrated.

---

Professor Tsu-Jae King Liu

Committee Chair

To my family, for their love and encouragement



# Table of Contents

Chapter 1 : Introduction .....	1
1.1 Benefits of MOSFET Scaling .....	1
1.2 Issues in Planar Bulk-Si MOSFET Scaling .....	2
1.3 Process-induced Variations .....	5
1.4 Thin-body MOSFETs .....	7
1.5 SRAM Scaling Issues .....	14
1.6 Summary .....	16
1.7 Research Objectives and Dissertation Outline .....	17
1.8 References.....	19
Chapter 2 : Circuit design implications of scaling sub-25 nm double-gate MOSFETs ...	26
2.1 Introduction.....	26
2.2 Device Design Optimization.....	27
2.3 Effect of Parasitic Capacitances .....	32
2.4 Circuit Simulations .....	34
2.5 Device Optimization under constant DIBL constraint .....	36
2.6 Conclusions.....	38
2.7 References.....	38
Chapter 3 : Energy-delay optimization of multi-gate FETs in the sub-25nm era.....	42
3.1 Introduction.....	42
3.2 Adaptive $V_{TH}$ in FDSOI MOSFETs .....	45
3.3 Transistor Design Optimization.....	47

3.4 Comparison of DG-FETs and BG-FETs .....	49
3.5 Circuit design benefits of BG-FETs .....	53
3.6 Conclusions.....	57
3.7 References.....	58
Chapter 4 : Design of back-gated FDSOI devices .....	61
4.1 Introduction.....	61
4.2 Background - Scale length of Thin-Body MOSFETs.....	62
4.3 Derivation of Quantum-Corrected Effective Conduction Path .....	63
4.4 Scale Length Derivation for BG-FDSOI devices .....	67
4.5 Implications of Scale length on BG-FDSOI Device Design .....	72
4.6 Relaxed Body-Thickness Scaling in BG-FDSOI MOSFETs .....	76
4.7 BG-FDSOI MOSFET Design Considerations.....	77
4.8 Effect of Parasitic Capacitances .....	81
4.9 Back-gate Biasing to Limit the Impact of Process Induced Variations.....	82
4.10 Conclusions.....	84
4.11 References.....	85
Chapter 5 : FinFET based SRAM design .....	89
5.1 Introduction.....	89
5.2 Challenges in Bulk-Si SRAM Scaling.....	90
5.3 6-T SRAM DESIGN TRADEOFFS.....	90
5.3.1 Area vs. Yield .....	91
5.3.2 Hold Margin.....	91
5.3.3 Read Margin.....	92

5.3.4 Write Margin.....	93
5.3.5 Access Time.....	94
5.3.6 Power .....	94
5.4 FinFET design for SRAMs.....	95
5.5 Simulation of FinFET-Based SRAM Cell Designs .....	96
5.6 FinFET based SRAM - Technology Considerations .....	99
5.6.1 Gate workfunction ( $\phi_G$ ).....	99
5.6.2 Channel doping .....	101
5.6.3 Body thickness.....	101
5.6.4 Fin surface orientation .....	102
5.6.5 Sensitivity of FinFET performance to process-induced variations.....	103
5.7 FinFET SRAM Cell Designs .....	104
5.7.1 Conventional Double-Gated (DG) Designs.....	105
5.7.2 FinFET-based 6-T SRAMs w/dynamic feedback.....	110
5.7.3 4-T FinFET SRAM Cell Design with Dynamic Feedback.....	113
5.7.4 Effect of Process-Induced Variations .....	116
5.8 Conclusions.....	117
5.9 References: .....	118
Chapter 6 : : FinFET SRAM process development .....	126
6.1 Introduction.....	126
6.2 FinFET SRAM fabrication .....	127
6.2.1 Cone defects formed during fin etching.....	128
6.2.2 Gate stack deposition .....	133

6.2.3 Gate patterning.....	136
6.2.4 Gate Planarization and Selective Gate Separation.....	139
6.2.5 Problems encountered in gate separation etch.....	146
6.2.6 Metallization .....	147
6.3 Summary.....	148
6.4 References.....	149
6.5 Appendix : Process Flow for FinFET-based SRAMs.....	152
Chapter 7 : Conclusions .....	155
7.1 Summary.....	155
7.2 Suggestions for Future Research .....	157
7.3 Conclusions.....	158
Appendix - Sample simulation input files.....	160

## Acknowledgements

I am deeply indebted to my research advisor, Prof Tsu-Jae King, for her advice, mentoring and encouragement during my graduate studies. Her vast technical expertise and insight have given me an excellent background in the field of semiconductor device physics. She has been a great advisor, constantly urged me to explore new ideas, and always been there to offer guidance and answer questions along the way. Her support and encouragement have made my stay a very pleasant and fruitful one, for which I am very thankful to her.

I would like to thank Prof Borivoje Nikolic' for being my co-advisor and his valuable feedback as a member of my qualifying exam and dissertation committee. His advice and insight into the future of semiconductor device technology from a circuit design perspective have been invaluable and helped me keep my work relevant. I would also like to thank Professor Eugene Haller and Vivek Subramanian for serving on my qualifying examination committee. I owe my understanding of semiconductor devices to Professor Chenming Hu and thank him for inculcating in me an appreciation for the quantitative aspects of device physics.

I would like to thank all the staff at the UC Microfabrication facility for their timely equipment fixes and tool upgrades to keep the lab functional. I would especially like to thank Sia Parsa and Evan Stateler for their efforts in battling the ASML stepper and helping me with the critical parts of my fabrication.

I am fortunate to have the opportunity to work with a group of very knowledgeable and friendly people who have made my experience at Berkeley most special. I would like to express my deep gratitude to Hideki Takeuchi, who helped

understand the nuances of microfabrication principles and troubleshooting tricks that have been invaluable for device processing in the Berkeley Microlab. I would also like to thank my seniors in the group especially Yang-Kyu Choi, Leland Chang, Daewon Ha, Pushkar Ranade, Kevin Cao, Charles Kuo, Igor Polishchuk, Yee-Chia Yeo and others who spent a lot of time in bringing me up to speed in the basics of my research, fabrication and simulation techniques that were central to this research. I would like to thank all my fellow graduate students Vidya Varadarajan, Mohan Dunga, Kyoungsub Shin, Hiu Yung Wong, Andrew Carlson, Joanna Lai, Chung-Hsun Lin, Alvaro Padilla, for helping me out at various points with research related issues. The people in the device group have managed to strike a good balance between work and play and made my stay at Berkeley both intellectually stimulating and fun at the same time.

I am thankful to Zheng Guo, Joshua Garrett and Radu Zlatanovici, who were also my research collaborators, for helping me get a better feel and understanding for digital design related issues. I must also give my sincerest thanks to the visiting industrial fellows to the Device Group, Akira Hokazono, Takuro Matsutoya, Yuri Masuoka and Koichi Fukoda for their sharing their experience and educating me about real world device design and processing challenges. I must thank Ruth Gjerde, who has been a very caring and helpful graduate assistant, always ready to answer questions with a smile and also Linda Manly and Judy Fong for being very helpful with administrative matters.

Thanks to Dr. Leo Matthew, Bich-Yen Nguyen, and Dr. Aaron Thean at Freescale Semiconductor Inc. for providing me with a great opportunity to gain valuable industrial experience and insight into numerous real world problems in transistor research.

I would like to express my utmost gratitude to my parents for their guidance and their immense sacrifices to ensure I received the best possible education. The tremendous encouragement from my parents, and my brother have been vital in my writing this thesis. I am deeply grateful to my grandparents for raising me through my high school and undergraduate years. Lastly, my wife, Akanksha, holds a special place in my heart and her support throughout my PhD work has meant so much to me. I am especially thankful to her for making sure that I stayed on course while writing my thesis and could not have finished writing this thesis without her support and encouragement.

# Chapter 1 : Introduction

## 1.1 Benefits of MOSFET Scaling

Computing capability has increased dramatically over the decades, enabled by significant advances in silicon integrated circuit (IC) technology led by the continued miniaturization of the MOS transistor. The rapid progress in the semiconductor industry has been driven by improved circuit performance and functionality together with reduced manufacturing costs. Since the 1960s, transistor dimensions have been shrinking 30% every 3 years, as predicted by Moore's law [1] depicted in Figure 1.1 [2] and scaling has in fact accelerated recently [3].

While Moore's law only describes the rate of increase in transistor density, reduction of the physical MOS device dimensions has improved both circuit speed and density in the following ways: a) Circuit operational frequency increases with a reduction in gate length,  $L_G$ , as  $\sim 1/L_G$ ; allowing for faster circuits, b) Chip area decreases  $\sim L_G^2$ ; enabling higher transistor density and cheaper ICs. c) Switching power density  $\sim$  constant; allows lower power per function or more circuits at the same power.

Device scaling has been a relatively straightforward affair thus far, but physical limits are fast being approached, and new materials and device structures are needed to continue scaling trends.



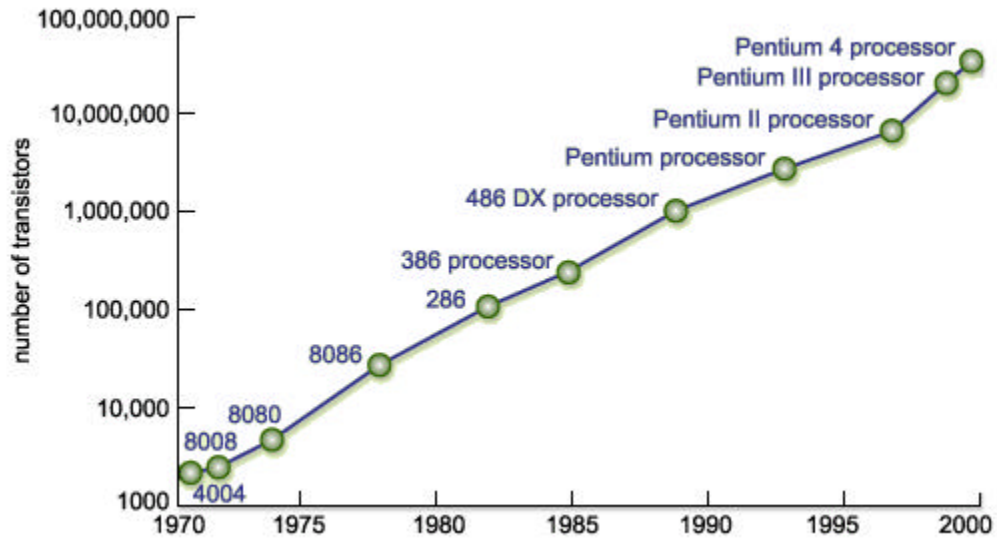


Figure 1.1: Moore's law of scaling. The number of transistors on a chip has been increasing exponentially (adapted from [1, 2])

## 1.2 Issues in Planar Bulk-Si MOSFET Scaling

The planar bulk-silicon MOSFET has been the workhorse of the semiconductor industry over the last 40 years. However, the scaling of bulk MOSFETs becomes increasingly difficult for gate lengths below  $\sim 20\text{nm}$  (sub-45 nm half-pitch technology node) expected by the year 2009. As the gate length is reduced, the capacitive coupling of the channel potential to the source and drain increases relative to the gate, leading to significantly degraded short-channel effects (SCE). This manifests itself as a) increased off-state leakage, b) threshold voltage ( $V_{\text{TH}}$ ) roll-off, i.e., smaller  $V_{\text{TH}}$  at shorter gate lengths, and c) reduction of  $V_{\text{TH}}$  with increasing drain bias due to a modulation of the source-channel potential barrier by the drain voltage, also called drain-induced barrier lowering (DIBL). In order to maintain the relatively strong gate control of the channel potential in bulk devices, various technological improvements such as ultra-thin gate

dielectrics, ultra-shallow source/drain junctions, halo implants and advance channel dopant profile engineering techniques such as super-steep retrograde wells have been necessary. Each of these technologies is now approaching fundamental physical limitations which may, in turn, limit further scaling of device dimensions.

In MOS devices, the gate dielectric thickness is the single most important device dimension to enable device scaling and has also been the most aggressively scaled one. A thin gate dielectric increases capacitive coupling from the gate to the channel, thereby reducing the source/drain influence on the channel. A larger gate capacitance also leads to a larger inversion charge density, or increased ON-state drive current. However, gate dielectrics are already so thin that quantum mechanical direct tunneling through them results in significant gate leakage currents below  $\sim 20\text{\AA}$ . The use of alternative high- $\kappa$  gate dielectric materials can provide a small effective oxide thickness to maintain adequate gate control needed for  $L_G$  scaling while providing a large physical barrier to gate-oxide tunneling, thereby reducing gate leakage.

Reduction of the source/drain extension junction depth directly decreases capacitive coupling of the drain to the channel, thus also reduces drain-induced short-channel effects. Shallow source/drain junction formation requires that low-energy ion implantation together with low thermal budget dopant activation to minimize dopant diffusion. The downside to this is the increase in the parasitic series resistance of the source and drain extension regions. Raised source/drain technologies can alleviate the extrinsic resistance problem while maintaining shallow junctions. The contact resistance associated with the metallic contacts to the source/drain regions is another source for

parasitic series resistance and is expected to dominate the total parasitic resistance of the device.

In order to scale bulk-Si transistors, heavy body doping is also necessary to eliminate leakage paths far from the gate dielectric interface and to increase back-gate (substrate) control of the body. For sub-100nm gate length devices, a strong halo implant is generally used to suppress sub-surface leakage, but this tends to increase the average channel doping in small  $L_G$  devices. High channel doping concentration, however, reduces carrier mobility due to impurity scattering and increased transverse electric field, increases subthreshold slope, enhances band-to-band tunneling leakage, and increases depletion and junction capacitances. These factors may combine to significantly degrade device performance.

In summary, from a device design point of view, in order to achieve good electrostatic integrity or good control of short-channel effects (SCE), the gate dielectric thickness,  $T_{OX}$ , the source/drain junction depth,  $X_J$ , and the channel depletion depth  $X_{DEP}$ , need to be scaled down. The scale length for a bulk device,  $I_{BULK}$ , is an indication of how short  $L_G$  can be made before the SCE are excessive, and is quantitatively expressed in Eq. 1-1. For good electrostatic control, the minimum  $L_G$  should be no less than  $\sim 5I_{BULK}$ . [4]

$$I_{BULK} = 0.1(T_{OX} X_J X_{DEP}^2)^{1/3} \quad \text{Eq. 1-1}$$

For a bulk MOSFET, gate leakage limits  $T_{OX}$  scaling,  $X_{DEP}$  scaling is limited to about 10 nm due to substrate-to-drain band-to-band tunneling current limitations on body doping, and  $X_J$  is limited by process limits for forming ultra shallow junctions with abrupt doping profiles. Experimental bulk MOSFETs have been demonstrated down to 5nm  $L_G$  [5]. However, the performance did not meet industry roadmap specifications [6],

especially for low power applications. Continued device scaling will require new materials and/or alternative MOSFET structures. Therefore bulk MOSFET scaling is becoming increasingly harder and new transistor designs offering better scalability are needed. These are introduced in the next section.

The IC industry has started to deploy circuit design and architectural techniques such as multiple cores and multiple threads that exploit parallelism to improve the overall chip performance, enhance the chip functionality while maintaining chip power density and total chip power dissipation at a manageable level. With more than one central processing unit (CPU) core on chip, the cores can each be clocked at a lower frequency while still providing for better overall chip performance. In addition, ever more cache memory is being added onto the processor chip in order to minimize the system performance penalty associated with finite-cache effects. With the shift to multi-core processing becoming increasingly important, the performance of each core can be correspondingly lower, meaning that lower leakage (vs. high performance) MOSFET designs will become increasingly important because the desired overall chip performance can be achieved through parallelism. The high drive currents needed for driving long interconnects will have to come from performance enhancement techniques such as strained silicon while maintaining low leakage.

### **1.3 Process-induced Variations**

Control of critical dimensions (CDs) such as  $L_G$  continues to be a difficult challenge, as the physical gate length is considerably smaller than the lithography printed linewidth. Controlling the lithography and etch processes to achieve critical dimension control to within 10% ( $3\sigma$ ), as prescribed in the 2003 International Roadmap for

Semiconductors (ITRS) [7] is almost universally unachievable, so the CD tolerance has been increased to 12% ( $3\sigma$ ) in 2005[6]; there might be a need to relax this requirement further in the future.

In order to limit the impact of variations, the semiconductor industry is actually using slightly larger physical gate lengths than those specified in the *ITRS*, especially for memory applications [8]. The slowing down of  $L_G$  scaling may be unavoidable in the future since the control of process variables does not track the scaling of minimum feature sizes. This is of particular importance for memory arrays, because if the desired degree of dimensional control were not achievable, design margins would need to be relaxed to achieve large functional memory arrays. This slowdown in technology scaling will probably be application specific, and is unavoidable if process-control is not robust enough.

While advanced process control can minimize systematic shifts in the CD, the role of random variations arising from statistical dopant fluctuations and line edge roughness is expected to increase, so that variations will impact the overall power dissipation and performance [9]. Therefore, statistical treatment of random variation of circuits (statistical design) is becoming increasingly important. New transistor structures should have better immunity to process variations, and devices with tunable  $V_{TH}$  are beneficial to counter any systematic shifts in transistor characteristics.

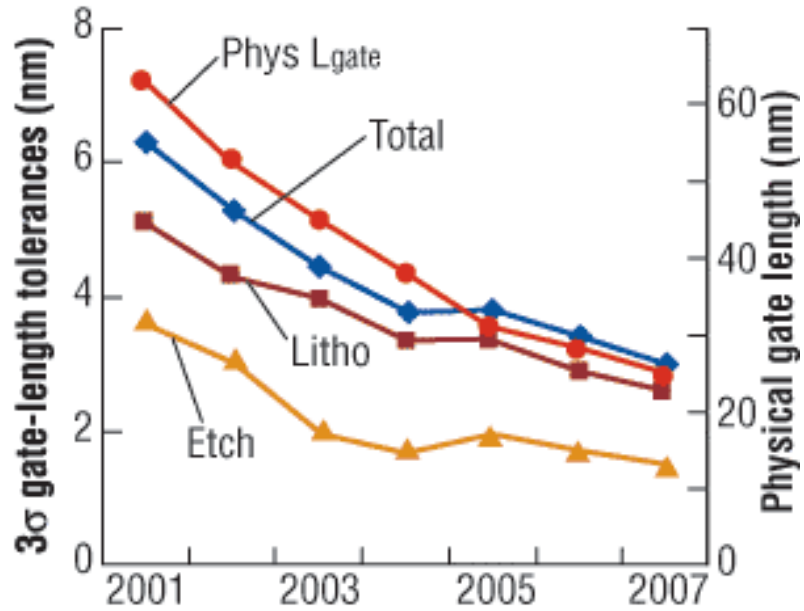


Figure 1.2: Changes in physical gate length, lithography tolerance, and etch tolerance over the years. The physical gate length tolerance has been relaxed to 12%, and this trend is expected to continue. [10]

### 1.4 Thin-body MOSFETs

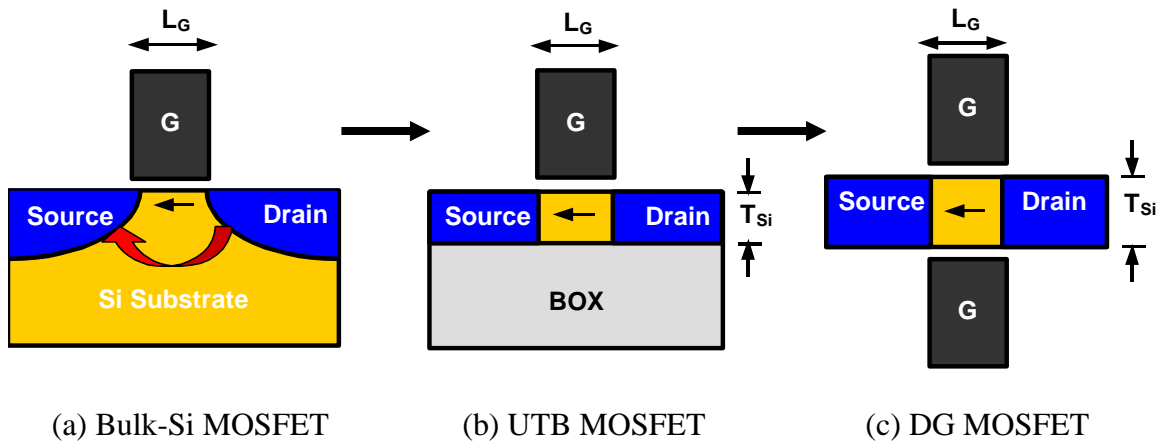


Figure 1.3: Advanced transistor structures such as the UTB and the DG-MOSFET eliminate sub-surface leakage paths and extend the scalability of Si CMOS technology.

As the bulk MOSFET is scaled down, the control of short channel effects becomes increasingly difficult leading to increased subthreshold leakage current. This is because the source/drain influence over the channel potential becomes significant relative to the gate control.

From Eq. 1-1, it is clear that if  $X_J$  and  $X_{DEP}$  can be reduced aggressively, it is possible to scale the MOSFET down to very small  $L_G$ . This is precisely what is done in the case of ultra-thin body (UTB) silicon-on-insulator (SOI) devices, where  $X_J$  and  $X_{DEP}$  are physically limited to the thickness of an ultra-thin silicon film. Eq. 1-1 only qualitatively describes the scaling behavior of UTB, and better models are introduced later. Thus, the scalability of MOS devices can be improved by using an ultra thin silicon body such that all points in the silicon channel are close enough to the gate and well controlled by it, thereby eliminating sub-surface leakage currents. The conventional fully depleted SOI MOSFET (with a thick body) is known to have worse short-channel effects than bulk MOSFETs and partially depleted SOI MOSFETs [11]. To achieve good short channel control,  $T_{Si}$  must be smaller than the depletion width or junction depth of a comparable bulk device with high channel doping. The leakage path in a UTB device is along the buried-oxide interface, furthest away from the gate. The thinner the silicon body is made, the larger is the leakage reduction from eliminating sub-surface leakage paths far away from the gate, and the better the device scalability. Also, UTB devices do not have the floating body effects seen in thick (partially-depleted) SOI devices (PDSOI), because there is no floating quasi-neutral region in the body.

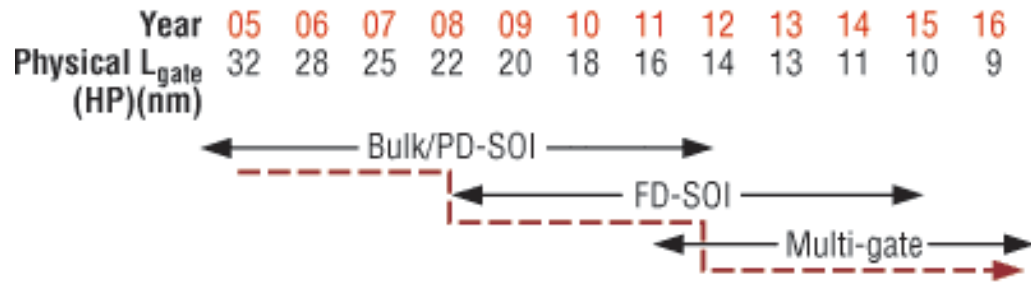


Figure 1.4: Advanced transistor designs may be necessary to meet performance requirements. Potential timetable for the adoption of advanced device structures to meet performance requirements. [6, 10]

The body thinness requirement can be relaxed by adopting the double-gate (DG) MOSFET structure shown in Figure 1.3 c, in which two gates control the channel potential. The DG-FET achieves better gate control and thereby has improved SCE for a given body thickness [12]. The body thickness can be twice that of a single-gated UTB device, in order to achieve the same degree of SCE. The DG MOSFET does not suffer from electric field penetration from the source/drain to the channel through the buried oxide and is therefore more scalable. The relaxed thinness requirement for the body is highly desirable from a manufacturability point of view, since the formation of a uniform ultra-thin film can pose major technological challenges. Simulation results show that a DG MOSFET has the best scalability, down to sub-10nm  $L_G$  devices [13]. The improved scalability of thin-body devices makes them attractive for future generations of CMOS technology and so they have been included in the International technology roadmap for semiconductors (ITRS) (see Figure 1.4) [6].



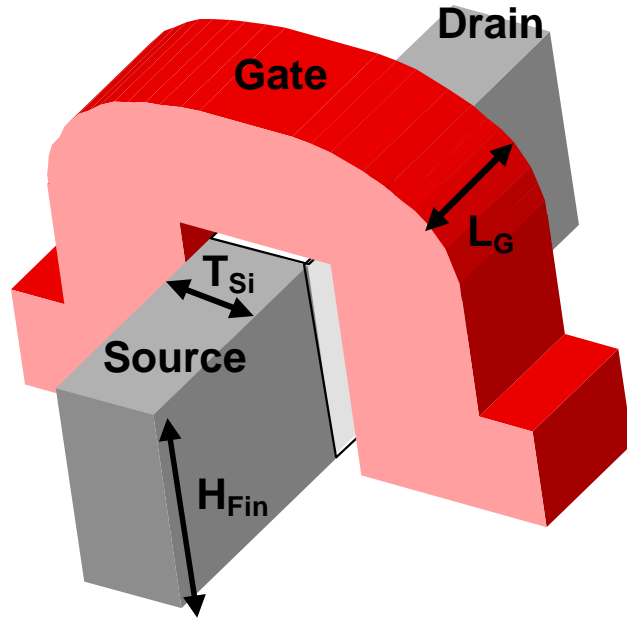


Figure 1.5: The FinFET consists of a thin Si fin, with the gate running over the fin in a self-aligned fashion. The gate controls the channel along the sidewalls of the fin and the width of the channel is defined by twice the height of the fin,  $H_{FIN}$ .

UTB devices can be implemented in a straightforward manner as planar single gate fully depleted silicon-on-insulator (FDSOI) devices [14-19]. While the planar double-gate device has been demonstrated [20], the fabrication of a planar double-gate FET with a bottom gate that is aligned to the top gate and source/drain regions imposes numerous process challenges. Among all DG structures proposed so far, the FinFET (Figure 1.5) is the most manufacturable because it eliminates the need for the bottom gate by rotating the channel by  $90^\circ$  and placing the gate electrodes on the two sidewalls of the silicon fin [21-23]. Independent gate FinFETs, in which the front and back-gate electrodes can be independently biased have been demonstrated as well [24, 25]. The front gate can be used to switch the device, whereas the back-gate can be used to set the correct  $V_{TH}$ . The back-gate is as strong as the front gate, and therefore the device has

degraded sub-threshold slope and transconductance due to a capacitive division of the channel potential between the two gates, however.

The planar FDSOI MOSFET can be extended to include a conducting electrode underneath the buried oxide (BOX) layer to form a second gate to control the channel from below [26]. This ground plane or the back-gate acts as a second gate to shield the field penetration from the drain into the channel, and improves SCE. In a way, it serves the role of the retrograde doping in a bulk MOSFET, by raising the body backside potential and by terminating drain electric fields [12]. In addition, the BOX eliminates source/drain-to-substrate depletion capacitance. In order to prevent electric field penetration through the BOX, the BOX layer should be thin. Another benefit of a thin BOX is the “back-gate effect,” similar to the “body effect” in bulk-Si devices, wherein the  $V_{TH}$  can be tuned by the back-gate voltage (Figure 1.6). However, the subthreshold slope and the transconductance are degraded due to the capacitive division of the channel potential between the front- and the back-gate potentials.

While the early FinFET devices were fabricated on SOI wafers, FinFETs on bulk-Si wafers have been demonstrated as well [27, 28]. Bulk-FinFETs have the advantages of being potentially cheaper and can be easily integrated with conventional bulk-Si CMOS technology. Bulk FinFETs combine the benefits of good leakage and short-channel control together with a cheaper manufacturing process, making them attractive for high-density memory applications.

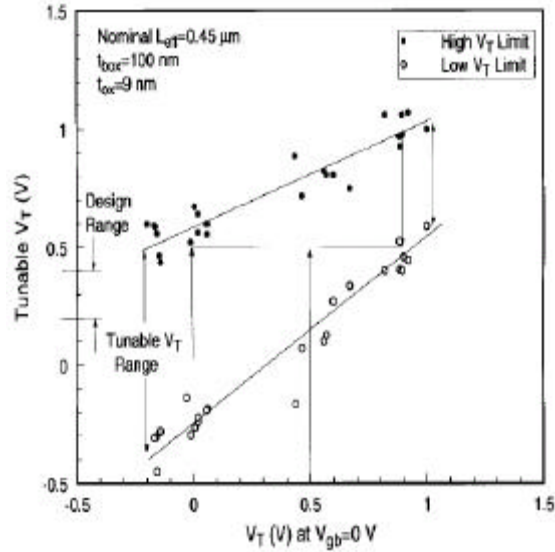


Figure 1.6: Back-gate effect in BG-FDSOI device showing  $V_{TH}$  tunability. The upper and lower limits of the tunable  $V_{TH}$  range are set by the back interface entering either inversion or accumulation.[26]

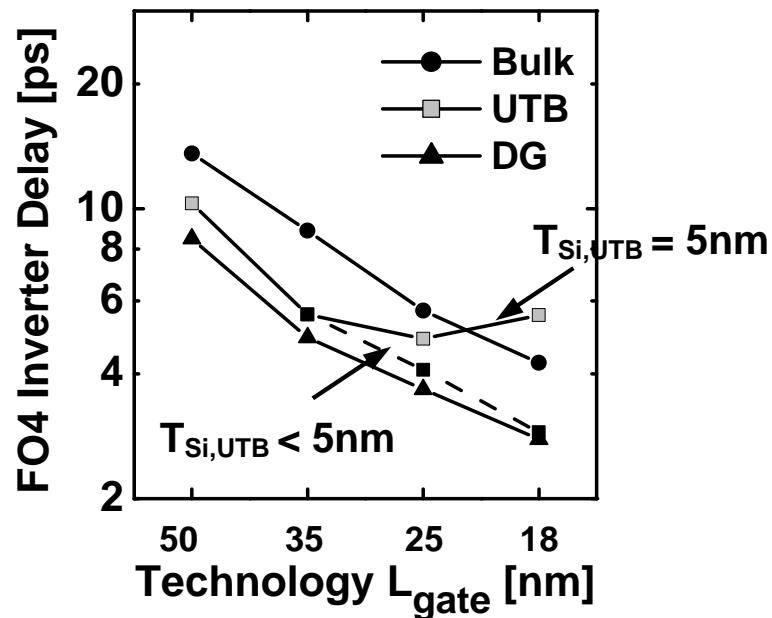


Figure 1.7: DG and UTB devices show better delay than planar bulk devices. The improved performance is due to a combination of improved subthreshold swing, higher carrier mobility, and reduced inversion capacitance and parasitic capacitances.[29]

The main benefits of thin body devices are improved transistor subthreshold swing due to greatly improved gate control, improved channel mobility due to reduced transverse electric field, reduced parasitic capacitances from the absence of depletion capacitances, leading to improved speed, and reduced power consumption. While the FinFET shows the largest performance benefits, the UTB device shows slightly degraded subthreshold swing and degraded ON-currents resulting in larger gate delays (Figure 1.7). [30]. The BG-FDSOI device, with its large back-gate effect and nonideal subthreshold swing, is expected to be slower than FinFET. However, it has the benefit of adaptive  $V_{TH}$  control, which is a promising way to limit the effect of variations.

Strained Si technology has been very successful in boosting the performance of both NMOS and PMOS devices, through enhancement in carrier mobilities. Popular approaches consist of local channel stressing through uniaxial stress induced by  $Si_{1-x}Ge_x$  source/drain regions for PMOS devices and from global stress induced by capping layers formed after gate patterning. While NMOS devices primarily benefit from tensile stress, compressive stress is beneficial in PMOS devices. The effect of biaxial and uniaxial stresses on transistor performance is now starting to be well understood [31]. UTB and FinFET devices can each benefit from a combination of local and global stresses. While it is harder to implement uniaxial stress from source/drain regions using  $Si_{1-x}Ge_x$  regions, stressed capping layers and gate electrode induced stress can be beneficial for boosting performance in FinFET devices [32, 33].

The main challenge with bringing UTB and FinFETs into manufacturing is the ability to form thin silicon channels with very good thickness uniformity. Fluctuations in the body thickness can cause spread in the  $V_{TH}$  and other device characteristics. Series

resistance is a big source of performance degradation in FDSOI devices and FinFETs, and so technologies such as raised source/drain achieved through selective epitaxy or deposition are needed to make low resistance contacts [12]. These technologies have been investigated and process solutions have been identified. [17, 23]

## **1.5 SRAM Scaling Issues**

Static random access memory (SRAM) is by far the dominant form of embedded memory found in today's integrated circuits (ICs) occupying as much as 60-70% of the total chip area and about 75%-85% of the transistor count in some IC products. The most commonly used memory cell design uses six transistors (6-T) to store a bit, so all of the issues associated with MOSFET scaling apply to scaling of SRAM. As memory will continue to consume a large fraction of the area in many future IC chips, scaling of memory density must continue to track the scaling trends of logic. [34]. Statistical dopant fluctuations, variations in oxide thickness, and line-edge roughness increase the spread in transistor threshold voltage and thus the on- and off- currents as the MOSFET is scaled down in the nanoscale regime [35]. Increased transistor leakage and parameter variations present the biggest challenges for the scaling of 6-T SRAM memory arrays.

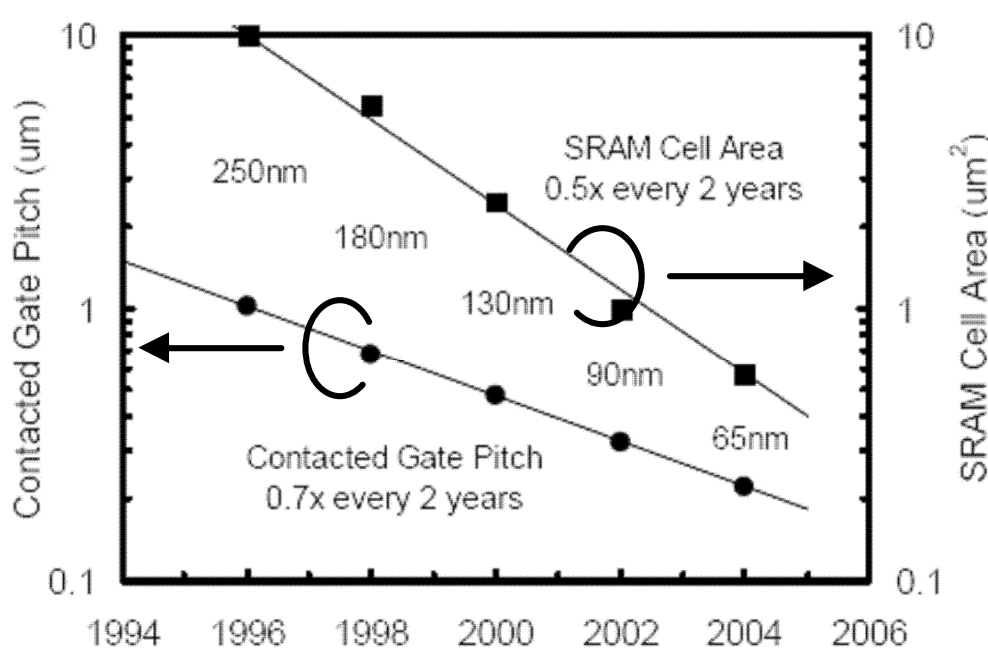


Figure 1.8: SRAM cell size has been scaling at  $\sim 0.5$  x per generation [36], but it might slow down due to lack of cell robustness caused by process induced variations. The data shows that SRAM scaling has been thus far tracking the scaling trends of logic.

The functionality and density of a memory array are its most important properties. Functionality is guaranteed for large memory arrays by providing sufficiently large design margins (to be able to be read without changing the state, to hold the state, to be writable and to function within a specified timeframe), which are determined by device sizing (channel widths and lengths), the supply voltage and, marginally, by the selection of transistor threshold voltages. Increase in process-induced variations results in a decrease in SRAM read and write margins, which prevents the stable operation of the memory cell, and is perceived as the biggest limiter to SRAM scaling. The 6-T SRAM cell size, thus far, has been scaled aggressively by  $\sim 0.5X$  every generation (Figure 1.8), however it remains to be seen if that trend will continue. Since the control of process variables does not track the scaling of minimum features, design margins will need to be

increased to achieve large functional memory arrays. Moving to more lithography friendly regular layouts with gate lines running in one direction, has helped in gate line printability [8], and could be the beginning of more layout regularization in the future. Also, it might become necessary to slow down the scaling of transistor dimensions to increase noise margins and ensure functionality of large arrays, i.e., tradeoff cell area for SRAM robustness. [34].

SRAM cells based on advanced transistor structures such as the planar UTB FETs and FinFETs have been demonstrated [37-41] to have excellent stability and leakage control. Some techniques to boost the SRAM cell stability, such as dynamic feedback [34], are best implemented using FinFET technology, because there is no associated layout area or leakage penalty. FinFET-based SRAMs are attractive for low-power, low-voltage applications.

## **1.6 Summary**

MOS technology has followed Moore's law for over four decades with the continual shrinking of transistor dimensions to increase the number of transistors on an integrated chip at an exponential rate. Transistors typically become faster and consume less power with each new process technology generation, leading to overall performance improvements. Unfortunately, due to fundamental physical limits to scaling, the era of conventional linear scaling of transistor dimensions has ended. Power dissipation and process-induced variations are big issues for continued scaling of bulk-Si MOSFETs in future generations. Improvements in transistor density, performance and power consumption together with high yield will become harder to achieve. Advanced device structures such as the UTB-FET and the FinFET offer improved performance and low

leakage. The back-gated FDSOI offers tunable performance and could be an attractive solution for counteracting process-induced variations. These new transistor structures can be seamlessly integrated into the CMOS design stream, making them attractive to extend Si CMOS scaling. With power-aware design in the presence of variations (statistical design) taking on a bigger role, extensive collaboration between circuit design, system architects and semiconductor device and process engineers will be crucial to translate the promises of these new device technologies into actual chip performance.

## **1.7 Research Objectives and Dissertation Outline**

In this dissertation, the key benefits of thin-body MOSFETs over the conventional planar bulk MOSFET are studied for future CMOS technologies. Through modeling and device simulation, scaling issues and performance of nanoscale thin-body transistor designs and their applications for improved circuit performance are evaluated.

In Chapter 2, transistor design optimization for the double-gate MOSFET is outlined in order to maximize the drive current and minimize circuit delay while taking into account parasitic resistance and capacitance effects. Based on this optimization, it is shown that a double-gate MOSFET needs to have an effective channel length larger than the physical gate length for scaling into the sub-10nm regime.

The gate delay versus energy consumption tradeoffs in double-gate versus back-gated device designs are studied in Chapter 3. Adaptive  $V_{TH}$  control in back-gated devices make them span a larger range in energy-delay space, making them attractive single technology solutions for variable throughput applications ranging from high performance to low power.



Chapter 4 quantifies the performance benefits of back-gated fully-depleted SOI devices (BG-FDSOI). The scale length for the BG-FDSOI is derived as a function of back-gate bias to account for the observed dependence of short channel effects on back-gate bias. The scale length is used to guide device design so as to make the BG-FDSOI close to FinFET in terms of performance while relaxing the body-thickness scaling requirement through the use of back-gate bias. It is shown that back-gate biasing can be used to partially reduce the impact of process variations.

Design considerations for FinFET based SRAM memory are discussed in Chapter 5. The tradeoffs in read margin, write margin, and cell area for various FinFET based designs are presented. In addition, a new FinFET-based SRAM cell with dynamic feedback is shown to provide significant improvement in SRAM noise margin, without area or leakage penalty. Also, a 4-T FinFET SRAM cell using dynamic feedback is shown to be an attractive low cost, high-density memory solution.

Chapter 6 presents the process development involved in the fabrication of FinFET-based SRAM with dynamic feedback. This involves the fabrication of double-gate FinFETs and independent-gate FinFETs simultaneously and is achieved using selective gate separation. The FinFET SRAM process has been transferred to other industrial fabrication facilities, because dynamic feedback is a promising manufacturable solution to extend SRAM scaling.

An overall summary of this dissertation is presented in Chapter 7. Key research contributions and suggestions for future research directions are highlighted.

## 1.8 References

- [1] G. E. Moore, "Cramming more components onto integrated circuits," *Electronics*, vol. 38, 1965, pp. 114 -- 117.
- [2] G. E. Moore, "No exponential is forever: but "Forever" can be delayed!," Proc. Proceedings of IEEE International Solid-State Circuits Conference. San Francisco, CA, 2003
- [3] E. J. Nowak, "Maintaining the benefits of CMOS scaling when scaling bogs down," *Ibm Journal of Research and Development*, vol. 46, 2002, pp. 169-80.
- [4] Z. H. Liu, C. Hu, J. H. Huang, T. Y. Chan, M. C. Jeng, P. K. Ko, and Y. C. Cheng, "Threshold voltage model for deep-submicrometer MOSFETs," *IEEE Transactions on Electron Devices*, vol. 40, 1993, pp. 86-95.
- [5] H. Wakabayashi, S. Yamagami, N. Ikezawa, A. Ogura, M. Narihiro, K. Arai, Y. Ochiai, K. Takeuchi, T. Yamamoto, and T. Mogami, "Sub-10-nm planar-bulk-CMOS devices using lateral junction control," Proc. IEEE International Electron Devices Meeting 2003. Washington, DC, 2003
- [6] "International Technology Roadmap for Semiconductors, 2005 ed," <http://www.itrs.net/Links/2005ITRS/Home2005.htm>.
- [7] "International Technology Roadmap for Semiconductors, 2003 ed," <http://www.itrs.net/Links/2003ITRS/Home2003.htm>.
- [8] P. Bai, C. Auth, S. Balakrishnan, M. Bost, R. Brain, V. Chikarmane, R. Heussner, M. Hussein, J. Hwang, D. Ingerly, R. James, J. Jeong, C. Kenyon, E. Lee, S. H. Lee, N. Lindert, M. Liu, Z. Ma, T. Marieb, A. Murthy, R. Nagisetty, S. Natarajan, J. Neiryneck, A. Ott, C. Parker, J. Sebastian, R. Shaheed, S. Sivakumar, J. Steigerwald,

- S. Tyagi, C. Weber, B. Woolery, A. Yeoh, K. Zhang, and M. Bohr, "A 65nm logic technology featuring 35nm gate lengths, enhanced channel strain, 8 Cu interconnect layers, low-k ILD and 0.57  $\mu\text{m}^2$  SRAM cell," Proc. 2004 International Electron Devices Meeting. San Francisco, CA, 2005
- [9] A. Asenov, "Random dopant induced threshold voltage lowering and fluctuations in sub-0.1  $\mu\text{m}$  MOSFET's: A 3-D "Atomistic" simulation study," *IEEE Transactions on Electron Devices*, vol. 45, 1998, pp. 2505-13.
- [10] J. Butterbaugh and C. M. Osburn, "Frontend processes required for continued CMOS scaling," *Solid State Technology*, 2006, pp.
- [11] L. T. Su, J. B. Jacobs, J. E. Chung, and D. A. Antoniadis, "Short-channel effects in deep-submicrometer SOI MOSFETS," Proc. Proceedings of 1993 IEEE International SOI Conference. Palm Springs, CA, 1993
- [12] H.-S. P. Wong, D. J. Frank, P. M. Solomon, C. H. J. Wann, and J. J. Welser, "Nanoscale CMOS," *Proceedings of the IEEE*, vol. 87, 1999, pp. 537-70.
- [13] L. Chang, Y. K. Choi, D. W. Ha, P. Ranade, S. Y. Xiong, J. Bokor, C. M. Hu, and T. J. King, "Extremely scaled silicon nano-CMOS devices," *Proceedings of the IEEE*, vol. 91, 2003, pp. 1860-1873.
- [14] V. Subramanian, J. Kedzierski, N. Lindert, H. Tam, Y. Su, J. McHale, K. Cao, T. J. King, J. Bokor, and C. Hu, "A bulk-Si-compatible ultrathin-body SOI technology for sub-100 nm MOSFETs," Proc. 1999 57th Annual Device Research Conference Digest. Santa Barbara, CA, 1999

- [15] Y.-K. Choi, K. Asano, N. Lindert, V. Subramanian, T.-J. King, J. Bokor, and C. Hu, "Ultrathin-body SOI MOSFET for deep-sub-tenth micron era," *IEEE Electron Device Letters*, vol. 21, 2000, pp. 254-5.
- [16] J. Kedzierski, P. Xuan, V. Subramanian, J. Bokor, T.-J. King, C. Hu, and E. Anderson, "A 20 nm gate-length ultra-thin body p-MOSFET with silicide source/drain," Proc. 5th Silicon Nanoelectronics Workshop. Honolulu, HI, 2000
- [17] Y. K. Choi, D. W. Ha, T. J. King, and C. M. Hu, "Nanoscale ultrathin body PMOSFETs with raised selective germanium source/drain," *IEEE Electron Device Letters*, vol. 22, 2001, pp. 447-448.
- [18] Z. Krivokapic, W. Maszara, K. Achutan, P. King, J. Gray, M. Sidorow, E. Zhao, J. Zhang, J. Chan, A. Marathe, and M. R. Lin, "Nickel silicide metal gate FDSOI devices with improved gate oxide leakage," Proc. IEEE International Electron Devices Meeting. San Francisco, CA, 2002
- [19] J. Kedzierski, E. Nowak, T. Kanarsky, Y. Zhang, D. Boyd, R. Carruthers, C. Cabral, R. Amos, C. Lavoie, R. Roy, J. Newbury, E. Sullivan, J. Benedict, P. Saunders, K. Wong, D. Canaperi, M. Krishnan, K. L. Lee, B. A. Rainey, D. Fried, P. Cottrell, H. S. Wong, M. Jeong, and W. Haensch, "Metal-gate FinFET and fully-depleted SOI devices using total gate silicidation," Proc. IEEE International Electron Devices Meeting. San Francisco, CA, 2002
- [20] H.-S. P. Wong, K. K. Chan, and Y. Taur, "Self-aligned (top and bottom) double-gate MOSFET with a 25 nm thick silicon channel," Proc. International Electron Devices Meeting. IEDM Technical Digest. Washington, DC, 1997

- [21] D. Hisamoto, W.-C. Lee, J. Kedzierski, H. Takeuchi, K. Asano, C. Kuo, E. Anderson, T.-J. King, J. Bokor, and C. Hu, "FinFET-a self-aligned double-gate MOSFET scalable to 20 nm," *IEEE Transactions on Electron Devices*, vol. 47, 2000, pp. 2320-5.
- [22] X. Huang, W.-C. Lee, C. Kuo, D. Hisamoto, L. Chang, J. Kedzierski, E. Anderson, H. Takeuchi, Y.-K. Choi, K. Asano, V. Subramanian, T.-J. King, J. Bokor, and C. Hu, "Sub 50-nm FinFET: PMOS," Proc. International Electron Devices Meeting 1999. Technical Digest. Washington, DC, 1999
- [23] N. Lindert, Y. K. Choi, L. Chang, E. Anderson, W. C. Lee, T. J. King, J. Bokor, and C. Hu, "Quasi-planar FinFETs with selectively grown germanium raised source/drain," Proc. 2001 IEEE International SOI Conference. Proceedings. Durango, CO, 2001
- [24] D. M. Fried, E. J. Nowak, J. Kedzierski, J. S. Duster, and K. T. Komegay, "A Fin-type independent-double-gate NFET," Proc. 61st Device Research Conference. Salt Lake City, UT, 2003
- [25] L. Mathew, Y. Du, A.-Y. Thean, M. Sadd, A. Vandooren, C. Parker, T. Stephens, R. Mora, R. Rai, M. Zavala, D. Sing, S. Kalpat, J. Hughes, R. Shimer, S. Jallepalli, G. Workman, W. Zhang, J. G. Fossum, B. E. White, B. Y. Nguyen, and J. Mogab, "CMOS Vertical Multiple Independent Gate Field Effect Transistor (MIGFET)," Proc. 2004 IEEE International SOI Conference. Charleston, SC, 2004
- [26] I. Y. Yang, C. Vieri, A. Chandrakasan, and D. A. Antoniadis, "Back gated CMOS on SOIAS for dynamic threshold voltage control," Proc. Proceedings of International Electron Devices Meeting. Washington, DC, 1995

- [27] T. Park, S. Choi, D. H. Lee, J. R. Yoo, B. C. Lee, J. Y. Kim, C. G. Lee, K. K. Chi, S. H. Hong, S. J. Hynn, Y. G. Shin, J. N. Han, I. S. Park, U. I. Chung, J. T. Moon, E. Yoon, and J. H. Lee, "Fabrication of body-tied FinFETs (Omega MOSFETs) using bulk Si wafers," Proc. 2003 Symposium on VLSI Technology. Digest of Technical Papers. Kyoto, Japan. 10-12 June 2003, 2003
- [28] K. Okano, T. Izumida, H. Kawasaki, A. Kaneko, A. Yagishita, T. Kanemura, M. Kondo, S. Ito, N. Aoki, K. Miyano, T. Ono, K. Yahashi, K. Iwade, T. Kubota, T. Matsushita, I. Mizushima, S. Inaba, K. Ishimaru, K. Suguro, K. Eguchi, Y. Tsunashima, and H. Ishiuchi, "Process Integration Technology and Device Characteristics of CMOS FinFET on Bulk Silicon Substrate with sub-10 nm Fin Width and 20 nm Gate Length," Proc. IEEE International Electron Devices Meeting, 2005. IEDM Technical Digest, Washington D.C., 2005, 721- 724.
- [29] L. Chang, "Nanoscale Thin-Body CMOS Devices," in *Dept. of Electrical Engg and Computer Sciences*: Univ. California, Berkeley, 2003.
- [30] L. Chang, Y.-K. Choi, K. J., N. Lindert, P. Xuan, J. Bokor, C. Hu, and T.-J. King, "Moore's law lives on," *IEEE Circuits & Devices Magazine*, vol. 19, 2003, pp. 35-42.
- [31] S. Thompson, G. Sun, K. Wu, J. Lim, and T. Nishida, "Key differences for process-induced uniaxial vs. substrate-induced biaxial stressed Si and Ge channel MOSFETs," Proc. 2004 International Electron Devices Meeting. San Francisco, CA, 2005

- [32] K. Shin, T. Lauderdale, and T.-J. King, "Effect of tensile capping layer on 3-D stress profiles in FinFET channels," Proc. 63rd Device Research Conference Digest, DRC '05., 2005
- [33] K. Shin, C. O. Chui, and T.-J. King, "Dual Stress Capping Layer Enhancement Study for Hybrid Orientation FinFET CMOS Technology," Proc. IEEE International Electron Devices Meeting (Washington D.C., USA), 2005
- [34] Z. Guo, S. Balasubramanian, R. Zlatanovici, T.-J. King, and B. Nikolic', "FinFET-based SRAM design," Proc. ISLPED '05. Proceedings of the 2005 International Symposium on Low Power Electronics and Design. San Diego, CA, 2005
- [35] A. Bhavnagarwala, S. Kosonocky, C. Radens, K. Stawiasz, R. Mann, and Q. Ye, "Fluctuation Limits & Scaling Opportunities for CMOS SRAM Cells," Proc. International Electron Devices Meeting, Technical Digest, Washington DC, 2005,28.2.
- [36] S.-M. Jung, H. Lim, W. Cho, H. Cho, C. Yeo, Y. Kang, D. Bae, J. Na, K. Kwak, B. Choi, S. Kim, J. Jeong, Y. Chang, J. Jang, J. Kim, K. Kim, and B.-I. Ryu, "Highly area efficient and cost effective double stacked S<sup>3</sup> (stacked single-crystal Si) peripheral CMOS SSTFT and SRAM cell technology for 512M bit density SRAM," Proc. 2004 International Electron Devices Meeting. San Francisco, CA, 2005
- [37] E. J. Nowak, T. Ludwig, I. Aller, J. Kedzierski, M. Leong, B. Rainey, M. Breitwisch, V. Gemhoefer, J. Keinert, and D. M. Fried, "Scaling beyond the 65 nm node with FinFET-DGCMOS," Proc. CICC Custom Integrated Circuits Conference. San Jose, CA, 2003

- [38] T. Park, H. J. Cho, J. D. Choe, S. Y. Han, S. M. Jung, J. H. Jeong, B. Y. Nam, O. I. Kwon, J. N. Han, H. S. Kang, M. C. Chae, G. S. Yeo, S. W. Lee, D. Y. Lee, D. Park, K. Kim, E. Yoon, and J. H. Lee, "Static noise margin of the full DG-CMOS SRAM cell using bulk FinFETs (Omega MOSFETs)," Proc. IEEE International Electron Devices Meeting 2003. Washington, DC, 2003
- [39] R. V. Joshi, R. Q. Williams, E. Nowak, K. Kim, J. Beintner, T. Ludwig, I. Aller, and C. Chuang, "FinFET SRAM for high-performance low-power applications," Proc. Proceedings of the 34th European Solid-State Device Research Conference. Leuven, Belgium. 21-23 Sept. 2004, 2004
- [40] P. Tai-Su, C. Hye Jin, C. Jeong Dong, H. Sang Yeon, P. Donggun, K. Kinam, E. Yoon, and L. Jong-Ho, "Characteristics of the full CMOS SRAM cell using body-tied TG MOSFETs (bulk FinFETs)," *IEEE Transactions on Electron Devices*, vol. 53, 2006, pp. 481-7.
- [41] B. Doris, Y. H. Kim, B. P. Linder, M. Steen, V. Narayanan, D. Boyd, J. Rubino, L. Chang, J. Sleight, A. Topol, E. Sikorski, L. Shi, L. Wong, K. Babich, Y. Zhang, P. Kirsch, J. Newbury, J. F. Walker, R. Carruthers, C. D'Emic, P. Kozlowski, R. Jammy, K. W. Guarini, and M. Leong, "High performance FDSOI CMOS technology with metal gate and high-k," Proc. 2005 Symposium on VLSI Technology. Kyoto, Japan. Japan Soc. of Appl. Phys.. IEEE Electron Devices Soc. 14-16 June 2005, 2005



# **Chapter 2 : Circuit design implications of scaling sub-25 nm double-gate MOSFETs**

## **2.1 Introduction**

Double gate MOSFETs (Figure 2.1) such as the FinFET are promising structures to be scaled into the sub-25nm regime [1-4]. DG-MOSFETs usually are designed to have a very thin Si channel that is fully-depleted in order to cut-off sub-surface leakage paths, thereby making them more scaleable. The use of lightly doped or undoped channels leads to enhanced immunity to dopant fluctuation effects, smaller drain-to-body capacitance and higher carrier mobility arising from a lower transverse electric field. With no doping in the channel, metal gates with suitable work function are required to achieve reasonable threshold voltages in fully-depleted devices. [5-8].

One of the challenges introduced by a thin silicon channel is the extremely high parasitic series resistance and contact resistance at the source and drain (S/D) regions. While parasitic resistance is a serious challenge in bulk devices [9, 10], the problem is more severe in thin-body devices, and various process technologies have been proposed to reduce it [11-13]. This chapter discusses device optimization methodology to identify the device design tradeoffs involved in order to find the balance between good-control of short channel effects (SCE) and minimizing external parasitic resistance. The tradeoffs

between the various device parameters in determining the short-channel behavior, can be studied using the framework of the scale length [2, 14]. This is important from the viewpoint of device scalability and is discussed in detail in Chapter 4.

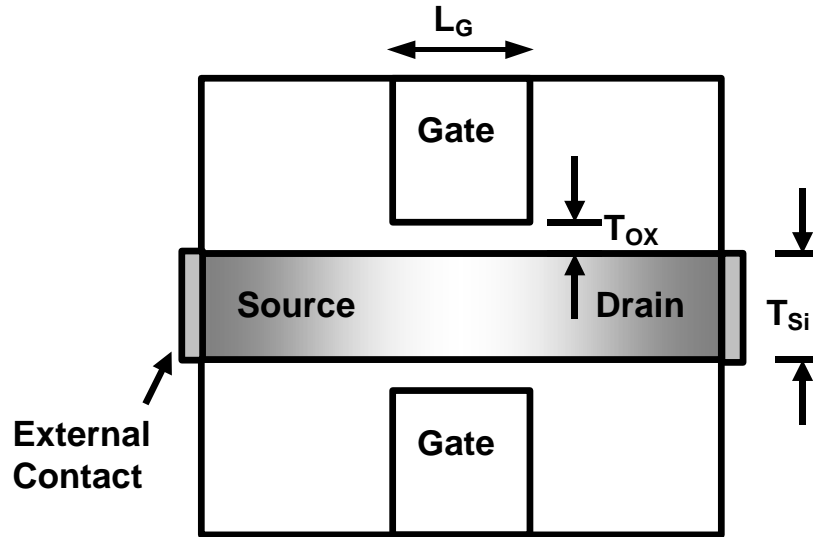


Figure 2.1: Schematic cross-section of the double-gate device structure use for simulations. Graded source-drain junctions are used. The structure includes sidewall spacers to capture the effect of parasitic capacitance. The gate work function is adjusted to meet the  $I_{OFF}$  specification.

## 2.2 Device Design Optimization

The DG-MOSFET device design optimization study has been carried out using calibrated energy transport models in the device simulator, Medici [15] and cross-checked with the quantum device simulator Nanomos 2.5 [16] for the case  $L_G = 13$  nm. The parameters used in the simulations are tabulated in Table 2-1. The silicon body thickness,  $T_{si}$ , needs to be around  $\sim 0.6 - 0.7 L_G$  for adequate control of short channel effects (SCE). The carrier energy relaxation times used in the hydrodynamic simulations to account for transient velocity overshoot effects are adapted from [17].

Parameter	45 nm node	32 nm node
$L_G$ (nm)	25	13
$T_{OX}$ (Å)	11	8
$T_{Si}$ (nm)	7	5
$V_{DD}$ (V)	0.7	0.5
Gate height (nm)	37.5	19.5
S-D gradient (nm/dec)	2.8	1.4
$t_{relaxation}$ (ps)	1.6	1.3
$I_{OFF}$ ( $\mu A/um$ )	0.3	1

Table 2-1: Summary of device parameters used in the simulations. The numbers used here are essentially taken from the ITRS roadmap 2001 (with more conservative numbers for  $T_{OX}$  and  $I_{OFF}$ ). [18].

Commonly, device optimization has been carried out with the aim to maximize the saturation drive current,  $I_{D,SAT}$ , subject to an upper limit on the leakage current [5]. Using this approach, a 25nm gate length device has been optimized by changing the source-drain separation in order to get the maximum drain current,  $I_{D,SAT}$  (Figure 2.2). The source-drain separation is related to the effective channel length of the device,  $L_{EFF}$ , and can be changed by adjusting the offset spacer thickness[19, 20].

The optimal source-drain (S-D) spacing is determined by a tradeoff between short-channel effects (SCE) and the series resistance of the channel. When S-D separation decreases,  $L_{EFF}$  is reduced and the leakage current increases due to increased worsened short channel effects. The S-D spacing is changed together with the metal gate

work function,  $\Phi_M$ , to meet the constant  $I_{OFF}$  specification. Therefore in a DIBL dominated regime (small  $L_{EFF}$ ), a higher  $\Phi_M$  is needed to compensate for the leakage increase due to degraded SCE. On the other hand, as the  $L_{EFF}$  increases with a larger S-D separation, the improvement in short channel effects due to reduced source/drain coupling is offset by a large increase in parasitic extension resistance and poor gate coupling between the channel and extensions, thereby degrading  $I_{D,SAT}$ . Thus, the right balance between the SCE and series resistance sets the optimal  $L_{EFF}$ .

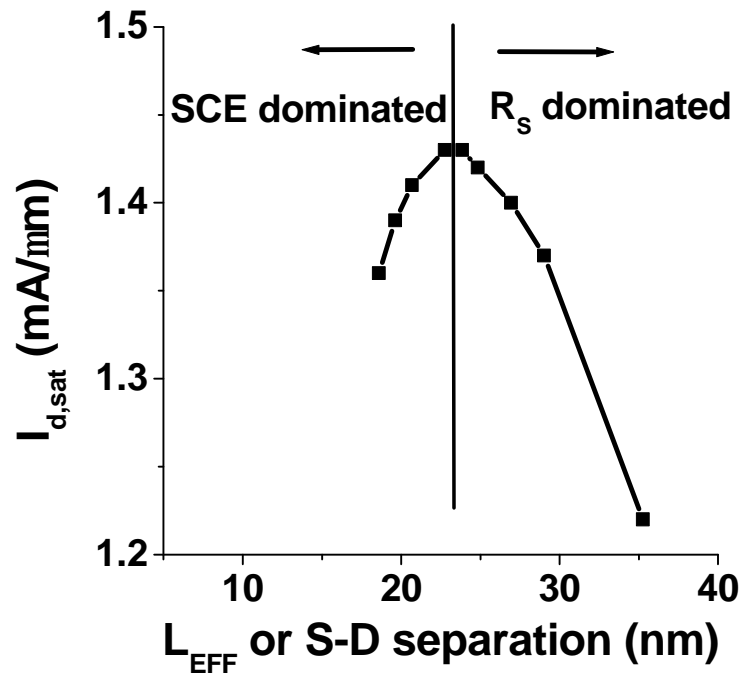


Figure 2.2: Dependence of the  $I_{D,SAT}$  on the source to drain separation for  $L_G=25$  nm. The optimal  $I_{D,SAT}$  is set by the tradeoff between SCE and series resistance.  $L_{EFF}$  is defined at the position where the doping falls off to  $2 \times 10^{19} \text{ cm}^{-3}$ .

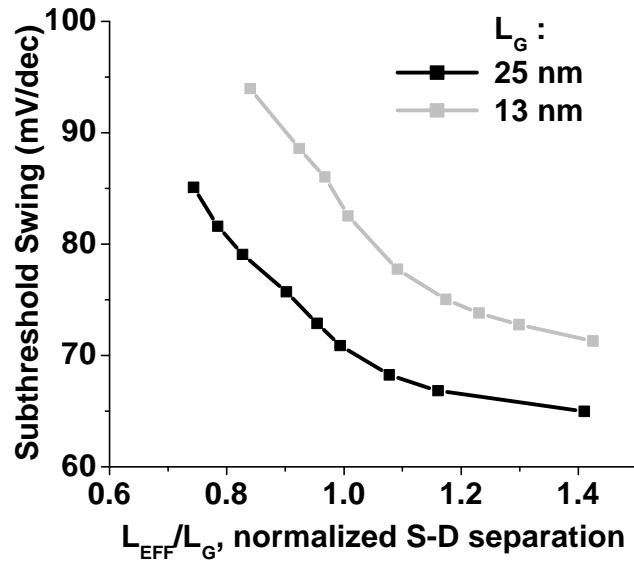


Figure 2.3: Subthreshold swing variation with the S-D separation normalized w.r.t.  $L_G$ . The swing for shorter  $L_G$  degrades due to increased source/drain coupling to the channel resulting in worsened DIBL and sub-threshold swing.

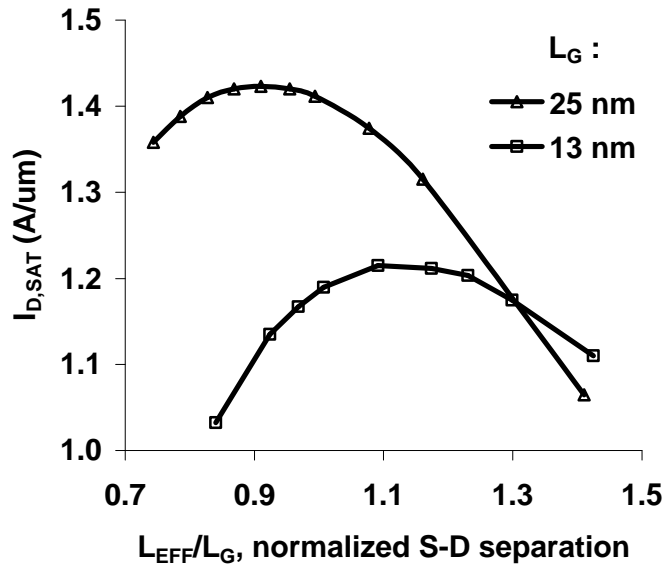


Figure 2.4: The optimal  $L_{EFF}$  needed is larger than  $L_G$  for very small  $L_G$ . With degraded SCE, the optimal underlap between gate and source/drain regions needed is greater.

Also, when the gate length is scaled from 25 nm to 13 nm, the short-channel effects are degraded (Figure 2.3) if the  $T_{OX}$  and  $T_{Si}$  cannot be scaled proportionately to  $L_G$  due to gate leakage limitations. Therefore, the optimal S-D separation or  $L_{EFF}$  for maximizing  $I_{D,SAT}$  in a scaled device with degraded SCE is expected to be larger. This is verified in Figure 2.4. Thus, having an effective channel length that is larger than the physical gate length ( $L_{EFF} > L_G$ ) is probably necessary to continue scaling devices. The trends hold true for PMOS devices as well.

In the above simulations the source/drain doping gradients were kept fixed as shown in Table 2-1. In order to understand the effect of source/drain doping gradients on device optimization, FinFETs with four different doping gradients were optimized to have same  $I_{OFF}$  and  $DIBL = 100$  mV/V, resulting in devices with the same  $V_{TH}$  and SCE. A device with a very graded profile would need thick gate sidewall spacers in practice to reduce the S/D encroachment into the channel. The optimal doping profiles from simulation are shown in Figure 2.5 and are all seen to intersect at a doping level of  $2-3 \times 10^{19} \text{ cm}^{-3}$ , which is the level at which  $L_{EFF}$  is defined [20]. Alternatively, if the  $V_{TH}$  and SCE effects are the same in these devices, they ought to have the same  $L_{EFF}$ . Therefore, the doping level of  $2-3 \times 10^{19} \text{ cm}^{-3}$  is an appropriate point from which to define  $L_{EFF}$ , consistent with [20].

This implies that different source-drain dopant activation technologies can be used in conjunction with the appropriate spacer thickness to achieve the same  $L_{EFF}$ . Steep S/D junctions need thin spacers, while graded junctions need a correspondingly thicker spacers.

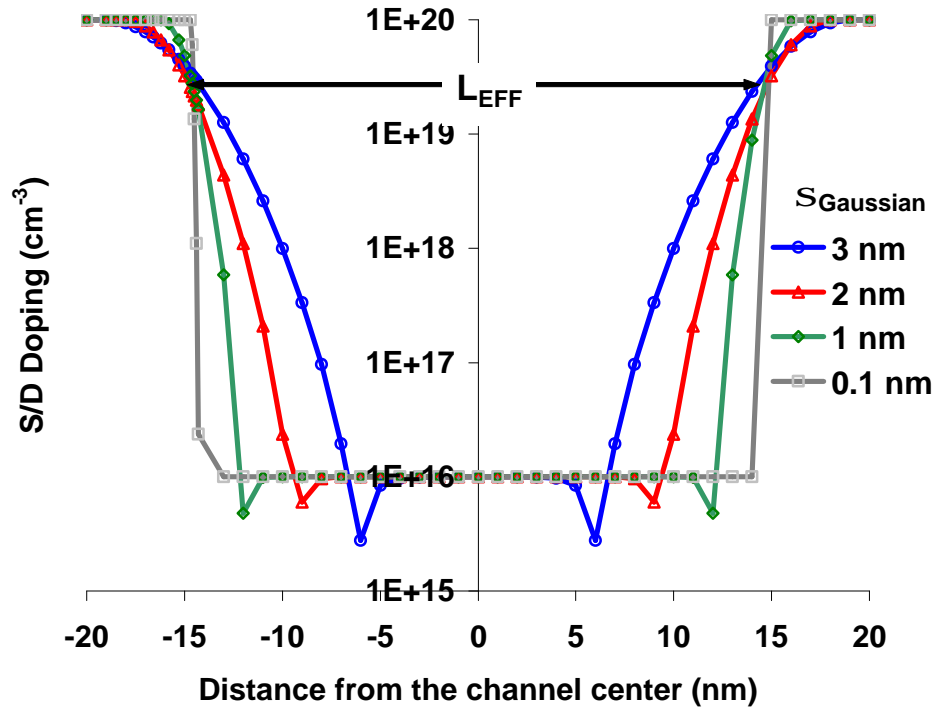


Figure 2.5: Equivalent source-drain doping profiles identified from Medici simulations [15] of four different FinFET devices, all with the same  $I_{OFF}$  and  $DIBL=100$  mV/V. These equivalent doping profiles all intersect at a doping level of  $2-3 \times 10^{19}$   $\text{cm}^{-3}$ , implying that they all have the same  $L_{EFF}$ . Step junctions need thin gate sidewall spacers, while graded junctions need a correspondingly thicker spacers to achieve the same  $L_{EFF}$ .

### 2.3 Effect of Parasitic Capacitances

This optimization for maximum  $I_{D,SAT}$ , however, does not take into consideration the role of parasitic capacitances and their impact on circuit performance. The total gate capacitance is the sum of the gate oxide capacitance, the gate to S/D overlap capacitance and the sidewall fringing capacitance [21].

In order to separate the effect of the overlap capacitance from the sidewall fringing effects, the capacitance simulations were run with a line gate, where the gate height,  $T_G$ , is set to zero. Therefore,  $C_{MIN}$ , ( $C_G @ V_{GS}=0$ ), is related directly to the overlap capacitance arising from the gate-to-source-drain overlap region. As the source and drain separation increases, the overlap capacitance between the gate and the source-drain regions decreases linearly (Figure 2.6). The  $C_{MAX}$ , ( $C_G @ V_{GS}=V_{DD}$ ), the gate capacitance in strong inversion, is slightly smaller than  $C_{OX}$  ( $= \epsilon_{OX}/T_{OX}$ , equivalent oxide capacitance), due to the increase in the electrical oxide thickness from quantum mechanical effects and is independent of source/drain overlap.

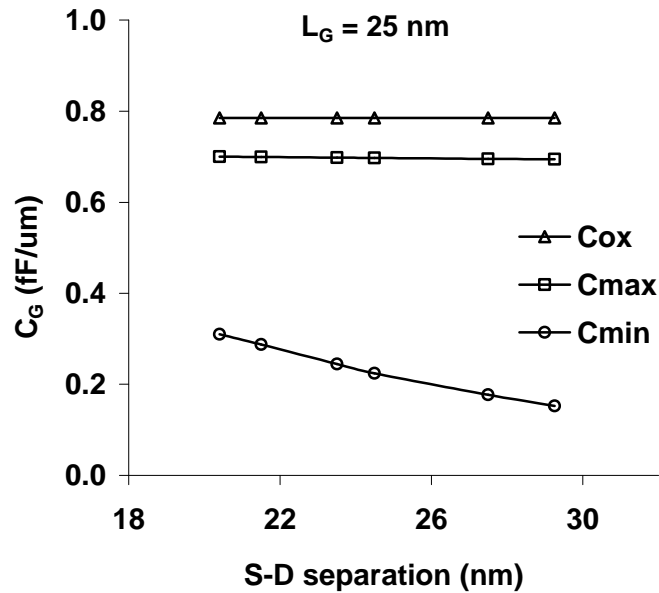


Figure 2.6: Variation of gate capacitance ( $C_G$ ) with the S-D separation (assuming a line gate,  $T_G = 0\text{nm}$ ).  $C_{MAX}$  is slightly smaller than  $C_{OX}$  because the quantum mechanical charge centroid is shifted away from the oxide interface.  $C_{MIN}$  ( $C_G @ V_{GS}=0$ ), decreases almost linearly with the S-D separation due to reduced gate-to-source/drain overlap area.



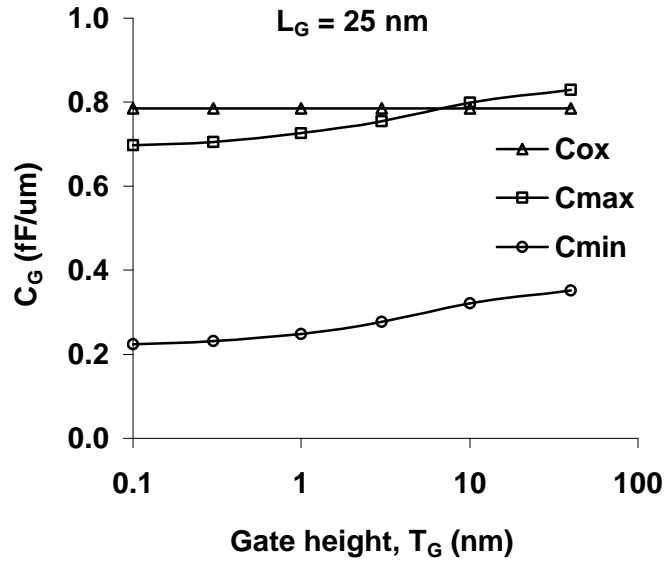


Figure 2.7: Variation of total gate capacitance ( $C_G$ ) with the gate height ( $T_G$ ).  $C_{MIN}$  and  $C_{MAX}$  increase with gate height due to increased fringing fields and saturate at large  $T_G$ .

The other component of the gate capacitance, the parasitic sidewall capacitance through the gate sidewall spacer, is not affected by the source-drain overlap. This component increases as the height of the gate is increased and saturates at large values of the gate height (Figure 2.7). While a smaller gate height is good to achieve a smaller capacitance, the height of the gate electrode is often determined by the need to keep the sheet resistance of the gate within bounds, and to ensure that the channel is protected from the S/D implants.

## 2.4 Circuit Simulations

To investigate the effect of parasitic capacitance on circuit performance, mixed-mode simulations of inverter FO-4 buffer chain were carried out in Medici [15]. The parasitic source/drain capacitance for a thin body transistor is very small, so it is expected that the optimal fan-out using the method of logical effort for minimal delay would be

closer to 3 [22]. However, a smaller effective fan-out per stage increases the number of driving stages and the total layout area, and the sensitivity of delay to fan-out near the optimal fan-out is small, so the fan-out factor of 4 is still used in this study.

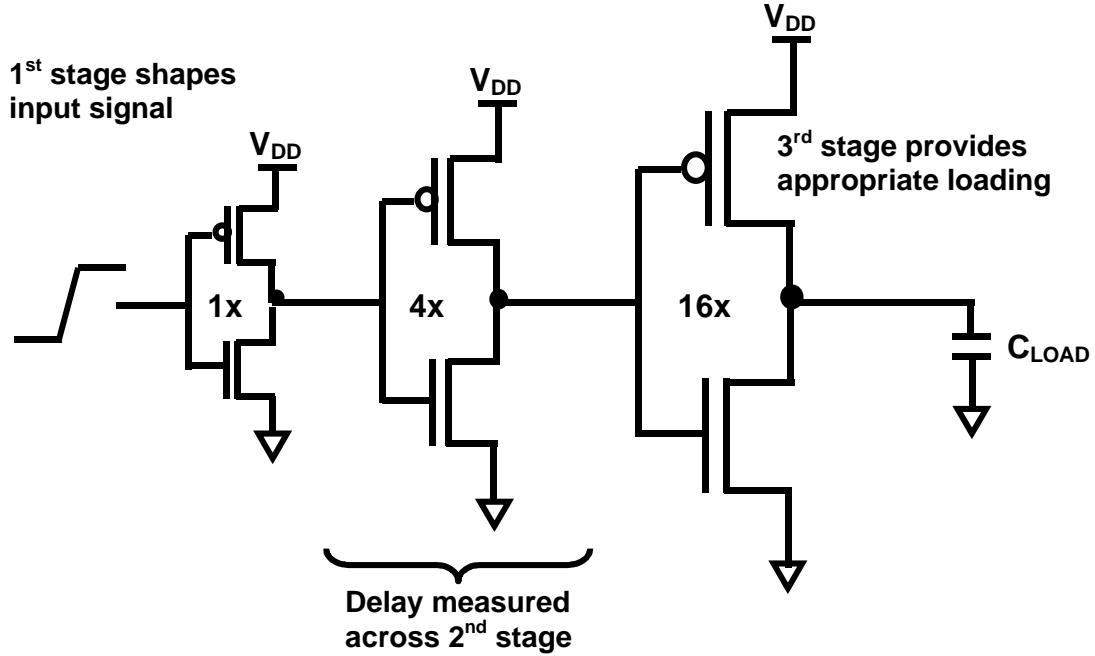


Figure 2.8: Schematic of FO-4 inverter mixed-mode simulation setup to measure the stage delay. The chain consists of 3 stages, the first stage corrects the input slope, the propagation delay is measured across the second stage and the last stage has a capacitive load equal to 4x of its input capacitance to present the appropriate Miller capacitance

The dependence of the FO-4 inverter delay on the source-drain spacing was investigated. The optimal spacing was found to be larger than that expected from maximizing drive current (Figure 2.9). This is because as the gate-to-S/D overlap region becomes smaller, its parasitic contribution to the total gate capacitance decreases. Therefore, in increasing the S/D spacing beyond the optimal value for maximum  $I_{D,SAT}$ , (from Figure 2.2) the capacitance reduction is more significant than the reduction in  $I_{D,SAT}$ , which results in an overall reduced delay. However, when the source-drain spacing

becomes even larger, i.e., as the gate to S/D underlap increases, the series resistance starts to dominate and the delay goes back up. The optimal spacing corresponding to minimal delay can result in dynamic power savings as well, because the parasitic part of the total switching capacitance is lowered significantly.

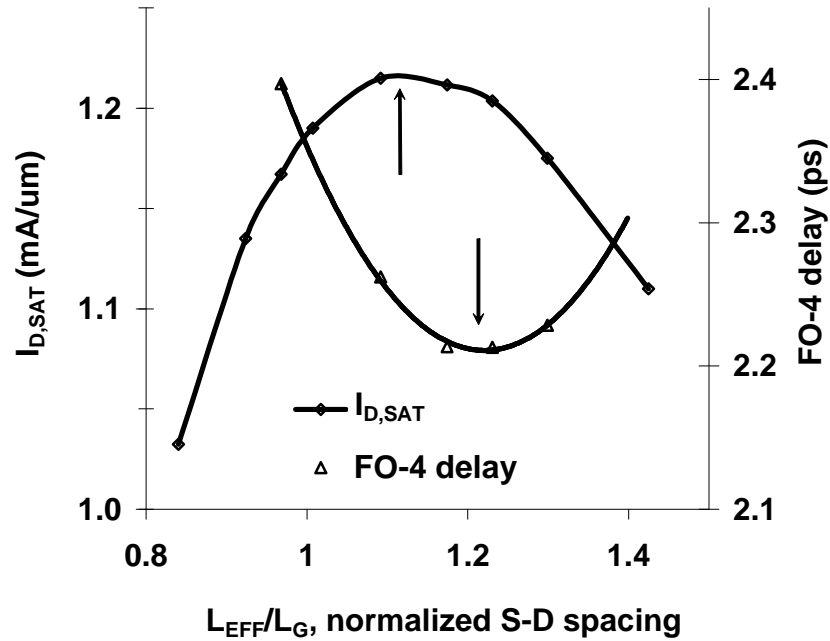


Figure 2.9: Dependence of the  $I_{D,SAT}$  and FO-4 delay on the normalized source to drain separation for  $L_G = 13$  nm. The optimal separation from the delay perspective is clearly larger than that for maximum  $I_{D,SAT}$ , i.e.,  $L_{EFF} > L_G$

## 2.5 Device Optimization under constant DIBL constraint

Device optimization thus far has been carried out under constant  $I_{OFF}$ , with  $L_{EFF}$  as the only design variable. As  $L_{EFF}$  is made longer, the DIBL gets better monotonically. In reality, constant  $V_{TH}$  (sets leakage) and constant DIBL are both constraints that need to be satisfied in maximizing performance. This aspect is addressed in greater detail in Chapter 4 on back-gated FDSOI design. In this section, a 100mV/V DIBL constraint is

additionally imposed, and the design optimization is briefly addressed below. Here  $T_{Si}$  is the additional physical parameter that is varied together with  $L_{EFF}$  to optimize device performance under DIBL constraints.

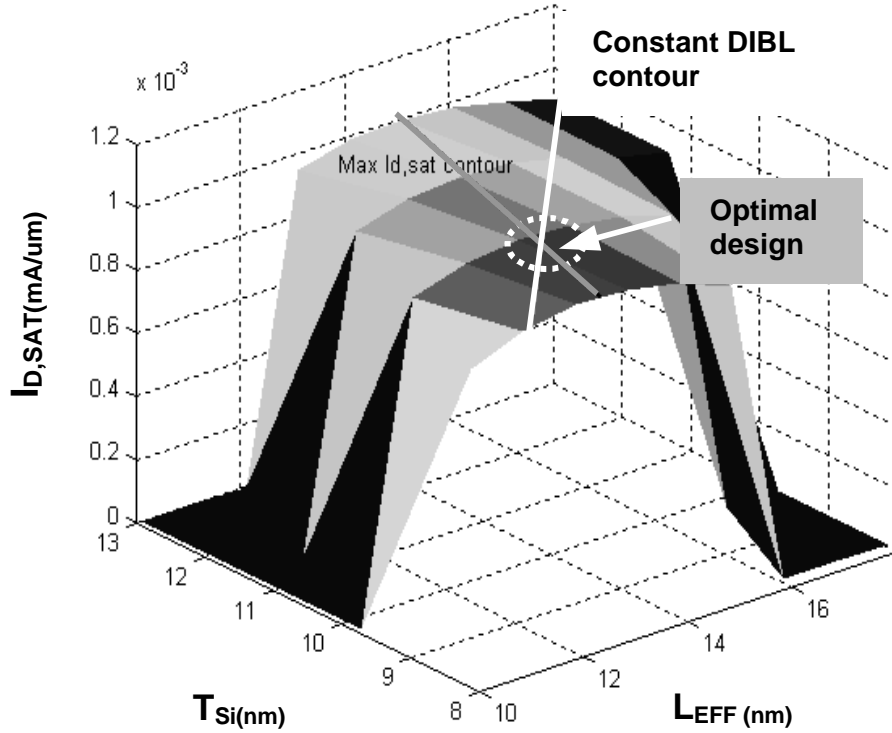


Figure 2.10: Dependence of  $I_{D,SAT}$  on  $T_{Si}$  and  $L_{EFF}$  for DG-MOSFET with  $L_G = 13$  nm,  $EOT = 6$  Å,  $\rho_C = 10^{-8}$  Ω cm<sup>2</sup>. As  $T_{Si}$  increases, SCE are degraded, and  $L_{EFF}$  needs to be longer in order to meet the constant DIBL constraint, as shown by the constant DIBL contour. The optimal  $I_{D,SAT}$  shows a weak dependence on  $T_{Si}$ , decreasing with thinner  $T_{Si}$  due to higher series resistance.

For each  $T_{Si}$ , the  $L_{EFF}$  optimization is carried out as described in Section 2.2 in order to identify the optimal  $I_{D,SAT}$  and is shown by maximum  $I_{D,SAT}$  contour in Figure 2.10. When  $T_{Si}$  increases, SCE are degraded, and  $L_{EFF}$  needs to be longer in order to meet the constant DIBL constraint, as shown by the constant DIBL contour in Figure 2.10. The intersection point between the maximum  $I_{D,SAT}$  contour and the constant DIBL contour

corresponds to the optimal device under DIBL constraints from the viewpoint of maximizing ON-current. A similar study can be carried out to identify the optimal delay point under SCE constraints.

## 2.6 Conclusions

When optimizing DG-MOSFET for maximum drive current,  $I_{D,SAT}$ , under constant leakage constraints, it is seen that the effective channel length,  $L_{EFF}$ , is an important design parameter. The optimal S-D separation is determined from the tradeoffs between short-channel effects and parasitic series resistance. Nanoscale devices may have to be designed with gate underlapped source/drain regions to meet the SCE requirements and optimize their performance. Also, the optimal underlap for maximizing drive current,  $I_{D,SAT}$ , is seen to be larger for smaller gate length devices. It is clear that optimizing devices with circuit performance considerations is important. The impact of parasitic capacitances on the performance of DG-MOSFETs has been investigated. The optimal  $L_{EFF}$  for minimizing circuit delay has been found to be larger than that needed to maximize transistor drive current, due to smaller parasitic overlap capacitance.

## 2.7 References

- [1] H. S. P. Wong, Y. Taur, and D. J. Frank, "Discrete random dopant distribution effects in nanometer-scale MOSFETs," *Microelectronics Reliability*, vol. 38, pp. 1447-1456, 1998.
- [2] D. J. Frank, Y. Taur, and H. S. Wong, "Generalized scale length for two-dimensional effects in MOSFETs," *IEEE Electron Device Letters*, vol. 19, pp. 385-7, 1998.

- [3] L. L. Chang, Y. K. Choi, J. Kedzierski, N. Lindert, P. Q. Xuan, J. Bokor, C. M. Hu, and T. J. King, "Moore's law lives on - Ultra-thin body SOI and FinFET CMOS transistors look to continue Moore's law for many years to come," *Ieee Circuits & Devices*, vol. 19, pp. 35-42, 2003.
- [4] Y.-K. Choi, N. Lindert, P. Xuan, S. Tang, D. Ha, E. Anderson, T.-J. King, J. Bokor, and C. Hu, "Sub-20 nm CMOS FinFET technologies," presented at International Electron Devices Meeting. Technical Digest. Washington, DC, 2001.
- [5] L. Chang, S. Tang, K. Tsu-Jae, J. Bokor, and H. Chenming, "Gate length scaling and threshold voltage control of double-gate MOSFETs," presented at International Electron Devices Meeting. Technical Digest. IEDM. San Francisco, CA, 2000.
- [6] P. Ranade, R. Lin, Q. Lu, Y. C. Yeo, H. Takeuchi, T. J. King, and C. Hu, "Molybdenum gate electrode technology for deep sub-micron CMOS generations," presented at Gate Stack and Silicide Issues in Silicon Processing II. Symposium. San Francisco, CA, 2002.
- [7] I. Polishchuk, P. Ranade, T. J. King, and C. Hu, "Dual work function CMOS gate technology based on metal interdiffusion," presented at Gate Stack and Silicide Issues in Silicon Processing II. Symposium. San Francisco, CA, 2002.
- [8] D. W. Ha, P. Ranade, Y. K. Choi, J. S. Lee, T. J. King, and C. M. Hu, "Molybdenum gate work function engineering for ultra-thin-body silicon-on-insulator (UTB SOI) MOSFETs," *Japanese Journal of Applied Physics Part 1- Regular Papers Short Notes & Review Papers*, vol. 42, pp. 1979-1982, 2003.
- [9] S. Thompson, P. Packan, T. Ghani, M. Stettler, M. Alavi, I. Post, S. Tyagi, S. Ahmed, S. Yang, and M. Bohr, "Source/drain extension scaling for 0.1 um and

- below channel length MOSFETs," presented at 1998 Symposium on VLSI Technology Digest of Technical Papers. Honolulu, HI, 1998.
- [10] J. Yuan, P. M. Zeitzoff, and J. C. S. Woo, "Source/drain parasitic resistance role and electrical coupling effect in sub 50 nm MOSFET design," presented at 32nd European Solid State Device Research Conference. Firenze, Italy. 24-26 Sept. 2002, 2002.
- [11] Y. K. Choi, D. W. Ha, T. J. King, and C. M. Hu, "Nanoscale ultrathin body PMOSFETs with raised selective germanium source/drain," *Ieee Electron Device Letters*, vol. 22, pp. 447-448, 2001.
- [12] Y. Chunshan, V. W. C. Chan, and P. C. H. Chan, "Low S/D resistance FDSOI MOSFETs using polysilicon and CMP," presented at Proceedings 2001 IEEE Hong Kong Electron Devices Meeting. Hong Kong, China. IEEE Electron Devices Soc.. Dept. Electron. & Inf. Eng. Hong Kong Polytech. Univ. 30 June 2001, 2001.
- [13] Z. Krivokapic, W. Maszara, F. Arasnia, E. Paton, Y. Kim, L. Washington, E. Zhao, J. Chan, J. Zhang, A. Marathe, and M. R. Lin, "High performance 25 nm FDSOI devices with extremely thin silicon channel," presented at 2003 Symposium on VLSI Technology. Digest of Technical Papers. Kyoto, Japan. 10-12 June 2003, 2003.
- [14] K. Suzuki, T. Tanaka, Y. Tosaka, H. Horie, and Y. Arimoto, "Scaling theory for double-gate SOI MOSFET's," *IEEE Transactions on Electron Devices*, vol. 40, pp. 2326-9, 1993.
- [15] "Medici v. 2002.4," Synopsys Inc.
- [16] "Nanomos, v 2.5," <http://nanohub.purdue.edu>.

- [17] M. Y. Chang, D. W. Dyke, C. C. C. Leung, and P. A. Childs, "High-energy electron-electron interactions in silicon and their effect on hot carrier energy distributions," *Journal of Applied Physics*, vol. 82, pp. 2974-9, 1997.
- [18] "International Technology Roadmap for Semiconductors," 2001.
- [19] Y. Taur and T. H. Ning, *Fundamentals of Modern VLSI Devices*: Cambridge University Press, 1998.
- [20] Y. Taur, Y.-J. Mii, R. Logan, and H.-S. Wong, "On "effective channel length" in 0.1-um MOSFETs," *IEEE Electron Device Letters*, vol. 16, pp. 136-8, 1995.
- [21] J. M. Rabaey, A. Chandrakasan, and B. Nikolic', *Digital Integrated Circuits*, 2 ed: Prentice Hall, 2002.
- [22] I. Sutherland, R. F. Sproull, and D. Harris, *Logical Effort: Designing Fast CMOS Circuits*: Morgan Kaufmann Publishers, 1999.



# Chapter 3 : Energy-delay optimization of multi-gate FETs in the sub-25nm era

## 3.1 Introduction

There are primarily two types of power dissipation in a CMOS digital integrated circuit: dynamic and static. The dynamic power arises from the useful work done in switching between logic states during digital computation. Dynamic power is proportional to  $CV_{DD}^2f$ , where  $C$  is the capacitive load being switched,  $V_{DD}$  is the supply voltage, and  $f$  is the clock frequency. The dynamic power dissipation is directly related to the rate of computation, so it can be adjusted to meet power budgets by adjusting the frequency of operation. Supply voltage scaling can also be used to adjust the dynamic power dissipation [1].

Static power, on the other hand, is associated with the holding of logic states, i.e., when the circuit is idle. This power is due to leakage mechanisms such as sub-threshold leakage or gate leakage within the transistors in the circuit, and is wasteful because it does not contribute to computation [1]. Leakage is unavoidable in modern CMOS technologies, and actually increases with scaling and is perceived as a major roadblock to scaling [2]. Today's microprocessors have thus entered power-limited scaling where

performance alone is not critical; rather performance under a power budget is the metric of relevance [3].

Power dissipation becomes a primary design constraint with further CMOS scaling, requiring circuit designs to be optimized considering both energy and delay. The effectiveness of heat removal system from hot spots poses limits on the power density, and impacts system cost and maximum attainable performance. Power constraints are even more stringent in mobile processor designs in which long battery life is desirable. The goal of a processor design, therefore, is to achieve the maximum operating frequency while meeting the power density constraint.

For high-performance chips, the high subthreshold leakage current must be within bounds to keep chip static power dissipation within acceptable limits. One common approach is multi- $V_{TH}$  technology, where low  $V_{TH}$  high-performance MOSFETs, are used only in critical paths to meet delay requirements and higher  $V_{TH}$  and larger EOT devices with lower leakage currents are used everywhere else to minimize the overall power dissipation without sacrificing performance. To achieve optimal energy vs. delay (E-D) performance [4], multiple transistor designs are needed to cater to various application areas. Other circuit/architectural techniques used to curtail static power dissipation include the use of sleep transistors to cut off access to power/ground rails or other techniques to power down circuit blocks [5].

Another potential technique used in bulk-Si MOSFET technology to tune the  $V_{TH}$  of NMOS and PMOS transistors separately is adaptive body biasing (ABB). The  $V_{TH}$  of a transistor can be controlled to a limited extent by using ABB, by applying a finite body-to-source voltage. By modulating the  $V_{TH}$ , the overall leakage and frequency for a die can

be controlled to some extent. Reverse body biasing (RBB) has been employed to reduce the standby leakage power dissipation, and the application of forward body bias (FBB) in active mode increases the frequency of operation, but it increases the leakage power as well. FBB has the desirable result of reducing the depletion thickness of the channel, thereby improving the short-channel effects (SCE) of a bulk-Si MOSFET, and improves the overall sensitivity to parametric variations. For the same reason, RBB increases the sensitivity to process variations due to worsened SCE. In extremely scaled transistors, the body effect is degraded due to worse short channel effects, and so adaptive body biasing to reduce leakage is not effective [6, 7]. Implementing ABB in bulk-Si technology requires a triple-well technology, which may not always be available.

For a multi-gate FET, adaptive threshold control, implemented through back-gate biasing, can be used in conjunction with dynamic voltage scaling (DVS) to minimize power dissipation in circuits and has been used in this study to achieve energy-delay optimality [8-11]. The goal of this combined  $V_{DD}$  and  $V_{TH}$  scaling scheme is to achieve the optimal combination of frequency and power, i.e., identify the minimum energy required to operate at a certain target frequency.

With parallelism, achieved through the use multiple cores, becoming more important, the emphasis on transistor performance is reducing and that on lower leakage transistors with minimal variations is increasing. In scaled technologies, achieving the target  $V_{TH}$  through process control alone is getting harder and the degree of process variations is getting larger. Dynamically tunable  $V_{TH}$  technologies provide a post-manufacturing electrical knob to fine tune a chip back to within the specifications and

thereby fill this gap between the target and achievable  $V_{TH}$  and are expected to become more important in the future.

Conventional UTB or FDSOI MOSFETs are built on thick BOX and therefore exhibit little or no effect on  $V_{TH}$  from the application of back-gate bias. However, when the BOX thickness is scaled down, the back-gate coupling to the channel increases and the  $V_{TH}$  change with back-gate bias can be used to modulate MOSFET performance. This chapter presents the design of energy-delay optimized back-gated thin-body SOI MOSFETs, (BG-FETs), and uses back-gate biasing to control the leakage power dissipation. It is demonstrated here that BG-FETs exhibit power savings over double-gate MOSFETs that increase with scaling into the sub-10 nm gate length regime. [12]

### 3.2 Adaptive $V_{TH}$ in FDSOI MOSFETs

In this section, we quantify the circuit level benefits of enhancement mode (ENH) thin-body double gate (DG) and back-gated (BG) MOSFETs.

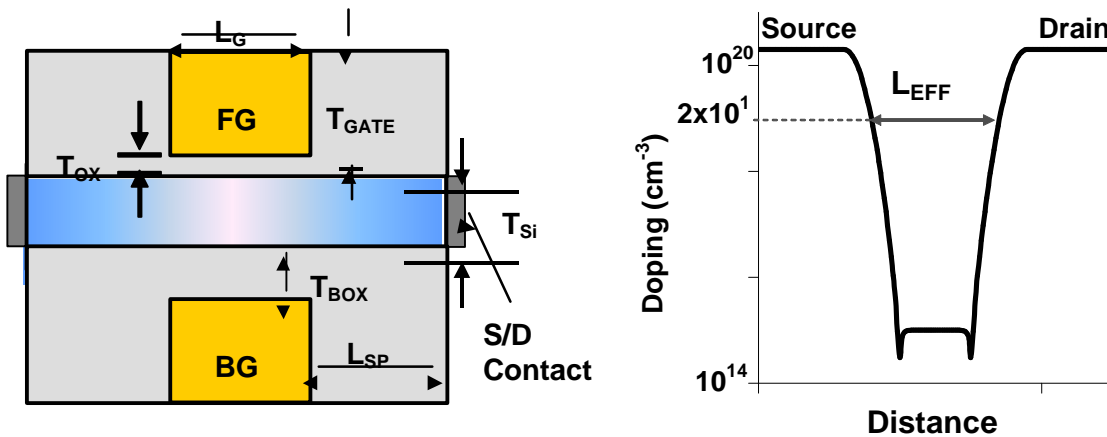


Figure 3.1 - Cross-sectional schematic of BG FETs studied. The effective channel length,  $L_{EFF}$ , for the BG-FET is defined as the separation between the points where doping falls off to  $2 \times 10^{19} \text{ cm}^{-3}$ .

Device parameters	32 nm node			22nm node
	BG ENH	DG-FET		BG-ENH
		HP <sup>a</sup>	LP <sup>b</sup>	
L <sub>G</sub> (nm)	13			9
L <sub>SP</sub> (nm)	13			9
T <sub>OX</sub> (Å) (EOT)	6			5
T <sub>BOX</sub> (Å)	63	11.5	11.5	47
T <sub>Si</sub> (nm)	5	8.2	8.2	3
T <sub>GATE</sub> (nm)	19.5	19.5	19.5	13.5
N <sub>BODY</sub> (cm <sup>-3</sup> )	2 x 10 <sup>16</sup>	2 x 10 <sup>16</sup>		2 x 10 <sup>16</sup>
Φ <sub>G</sub> (eV)	4.4	4.45	4.6	4.33
V <sub>DD</sub> (V)	0.6	0.6	0.6	0.5
S-D σ <sub>Gaussian</sub> (nm)	2.0	2.0	2.0	1.4
ρ <sub>C</sub> , (Ω-cm <sup>2</sup> )	5x10 <sup>-9</sup>	5x10 <sup>-9</sup>		5x10 <sup>-9</sup>
L <sub>EFF</sub> (nm)	20.2	15.6	15.6	12
I <sub>off, active</sub> (μA/μm)	1	1	0.01	3
I <sub>ON</sub> (μA/um)	575	665	398	629
I <sub>SLEEP</sub> (nA/μm) <sup>c</sup>	10	1000	10	66

Table 3-1: Summary of the MOSFET design parameters used. - HP<sup>a</sup> refers to high performance and LP<sup>b</sup> refers to low power. The L<sub>EFF</sub> for the MOSFET is defined as distance between points where the doping concentration falls to 2x10<sup>19</sup> cm<sup>-3</sup>. <sup>c</sup> The sleep state standby leakage current, I<sub>SLEEP</sub>, is evaluated at V<sub>BG</sub> = -V<sub>DD</sub>.

DG-FET and BG-FET device simulations were carried out in the Taurus-Device simulator using drift-diffusion transport and the 1-D Schrödinger equation [13]. (See Figure 3.1 and Table 3-1).

### 3.3 Transistor Design Optimization

The DG-FETs and BG-FETs were each optimized to achieve maximum  $I_{ON}$  at constant active-state leakage,  $I_{OFF} = 10^{-6}$  A/ $\mu\text{m}$ , and DIBL of 100 mV/V. This was achieved by co-optimizing  $T_{Si}$ ,  $T_{BOX}$ , S-D separation to change  $L_{EFF}$ , and using gate workfunction tuning to achieve the target  $I_{OFF}$ , at constant  $T_{OX}$  using the design-of-experiments (DOE) methodology, similar to that described in Chapter 2 [14]. Two versions of the DG-FET are also included in the study: a low  $V_{TH}$ , high-performance (HP) device and a higher  $V_{TH}$ , low-power (LP) device. (See Table 3-1.) The only difference between these two devices is the  $V_{TH}$ , with the LP device having a 100x lower leakage as compared to the HP device, achieved through a gate workfunction shift. These two versions of the DG-FETs would be needed for a multi- $V_{TH}$  technology to control the overall power dissipation as discussed earlier. Note that  $L_{EFF}$  must be larger than the physical gate length  $L_G$  to achieve good short channel effects in sub-15nm devices [15] (Table 3-1).

BG-FETs, have a thicker  $T_{BOX}$ , and therefore need to have a thinner body than DG-FETs to have the same degree of short channel effect control. In this section, the front- and back-gate workfunctions are assumed to be equal, resulting in a negligible transverse electric field in the channel. This pushes the active state leakage path to position of the weakest gate control, i.e., the back oxide/channel interface. However, in the sleep state, a reverse bias can applied to the back-gate to reduce the leakage of these devices. The scalability of the BG-FET can be improved if reverse back-gate biasing can be used even

in the active mode (together with a front-gate with a lower workfunction to compensate for the accompanying  $V_{TH}$  shift) to setup a high electric field in the channel and is described in chapter 4.

A thinner  $T_{BOX}$  provides higher  $V_{TH}$  sensitivity to  $V_{BG}$ . However, an ultra-thin  $T_{BOX}$  also has increased quantum-mechanical direct tunneling between the back-gate and the channel near the drain edge, thereby increasing the BG-leakage current in the sleep mode. Another disadvantage is worsened sub-threshold slope and device transconductance,  $g_m$ , due to the capacitive division of the channel potential between the front gate and the back-gate causing degraded transistor performance. In addition, at large reverse back-gate bias values, the back channel is biased into accumulation and the  $V_{TH}$  sensitivity to back-biasing becomes quite weak. At that point, the maximum reverse bias is limited by the back-gate induced band-band tunneling (BTBT) between the back-channel accumulation layer and the reverse-biased drain. The  $T_{BOX}$  was chosen in this work in such a way that the back-side BTBT leakage limit is still not reached at maximum back bias (limited to  $-V_{DD}$  for the n-channel MOSFET) and the direct tunneling leakage through the back-oxide is small (50-100× lower) compared to  $I_{OFF}$ .

The back-gate effect to modulate  $V_{TH}$  in back-gated FDSOI devices can be retained with scaling if the  $T_{BOX}$  can be scaled as well (Figure 3.2). The  $T_{BOX}$  needs to be about ~5x –10x of the  $T_{OX}$  to have a good tradeoff of  $V_{TH}$  tunability without having to apply a very large  $V_{BG}$  and to limit degradation of device turn-on characteristics.

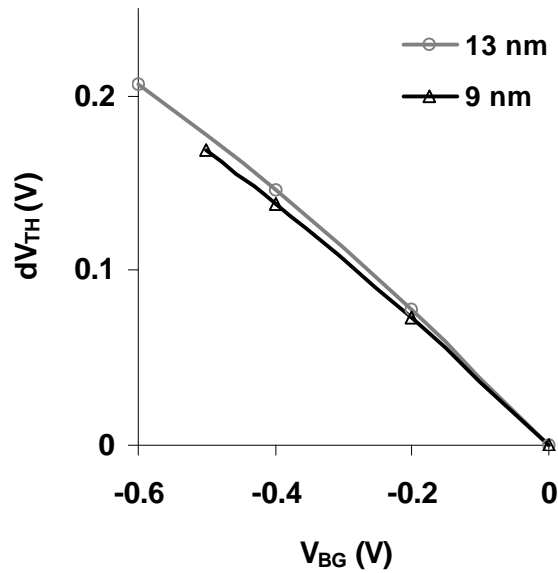


Figure 3.2 - The BG-FET devices show good sensitivity to  $V_{BG}$  that is retained with scaling, if the  $T_{BOX}$  is scaled as well. (ref. Table 3-1)

### 3.4 Comparison of DG-FETs and BG-FETs

BG-FETs and DG-FETs are compared to study the short channel behavior, ON-state performance and the immunity to process-induced variations. Figure 3.2 shows that the BG-FET design can be optimized to have a large back-gate effect, and therefore can be put into deep sleep mode, making it attractive for low power applications. Simulations of the BG-FETs were carried out with  $L_G = 9\text{nm}$  and  $13\text{nm}$ , and the effectiveness of the back-gate control on  $V_{TH}$  is still retained at short  $L_G$ . The BG-FETs are optimized in order to achieve a sleep state current of  $10^{-8}$  A/ $\mu\text{m}$  at  $V_{BG} = -V_{DD}$ . Increasing the back-gate effect to reduce the sleep state current comes at the expense of  $I_{ON}$ . From Figure 3.3, it can be seen that the BG-FETs devices have  $I_{ON}$  intermediate to those for the HP and LP DG-FETs. In order to limit saturation current degradation arising from the back-gate effect, a thicker  $T_{BOX}$  is desirable.



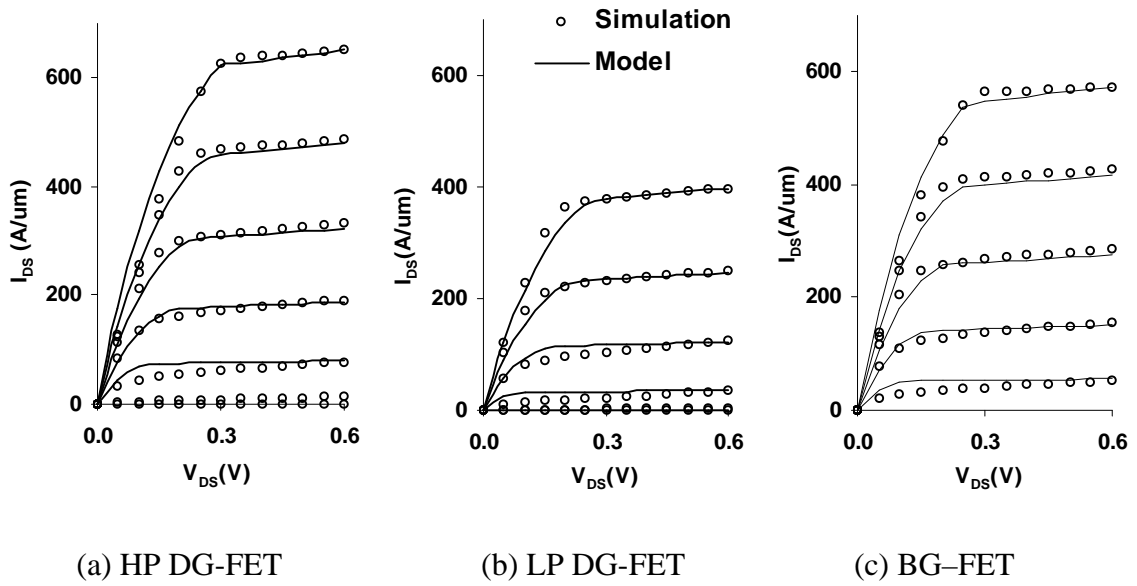


Figure 3.3 - Drain characteristics of the FETs used in the study. (a-c) The simulation data from Taurus [13] (points) was fitted to an empirical model (Eq 3-1), shown by solid lines.

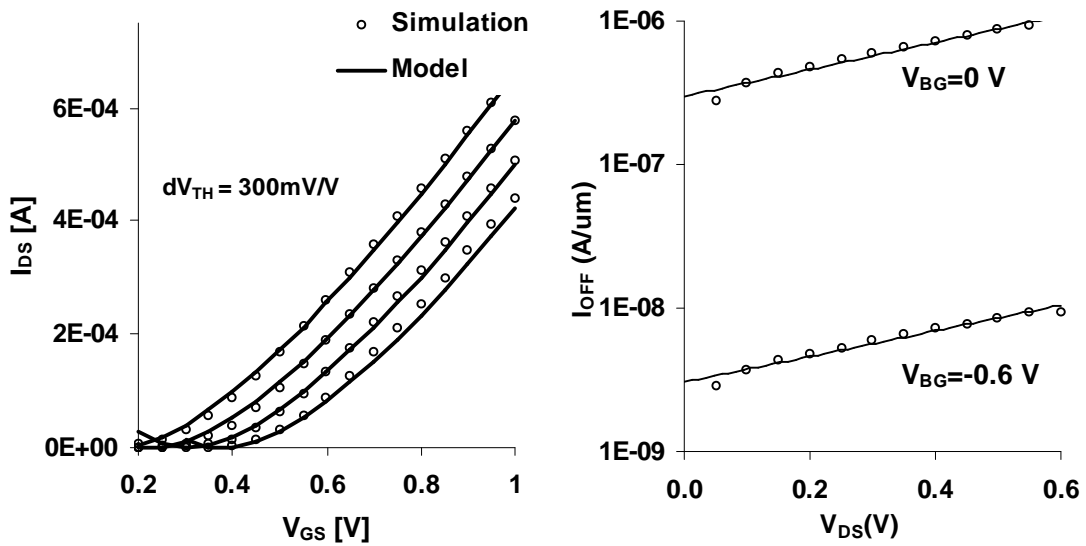


Figure 3.4 (a) Change in the  $I_{DS}$  with back-gate biasing is captured through (b)  $I_{OFF}$  vs.  $V_{DS}$  @  $V_{BG}$ . The leakage of the BG devices matches that of the HP DG-FET at zero back bias, and at  $V_{BG} = -V_{DD}$  match that of the LP DG-FET.

$$\begin{aligned}
 I_{DLIN} &= \frac{2KV_{DS}(V_{GS} - V_{TH} - 0.5V_{DS})}{V_{DS} + E_C L} \left(1 - \frac{V_{DS}}{V_A}\right) \\
 I_{DSAT} &= \frac{K(V_{GS} - V_{TH})^2}{V_{GS} - V_{TH} + E_C L} \left(1 - \frac{V_{DS}}{V_A}\right) \\
 V_{DSAT} &= \frac{E_c L(V_{GS} - V_{TH})}{E_c L + V_{GS} - V_{TH}}
 \end{aligned}
 \tag{Eq. 3-1}$$

A semi-empirical device model (Eq. 3-1) [16] based on a subset of BSIM3 model equations can fit the simulated drain current characteristics,  $I_{DS}$ - $V_{DS}$  data of HP, LP DG-FETs and BG-FETs (Figure 3.3). It also captures the  $V_{TH}$  shift from back-gate biasing and captures its effect on ON-state and OFF-state currents (Figure 3.4). Also, mobility enhancement parameters and the effect of parameter variations can be modeled to create Spectre AHDL models for DC simulation to estimate gate delay and power dissipation.

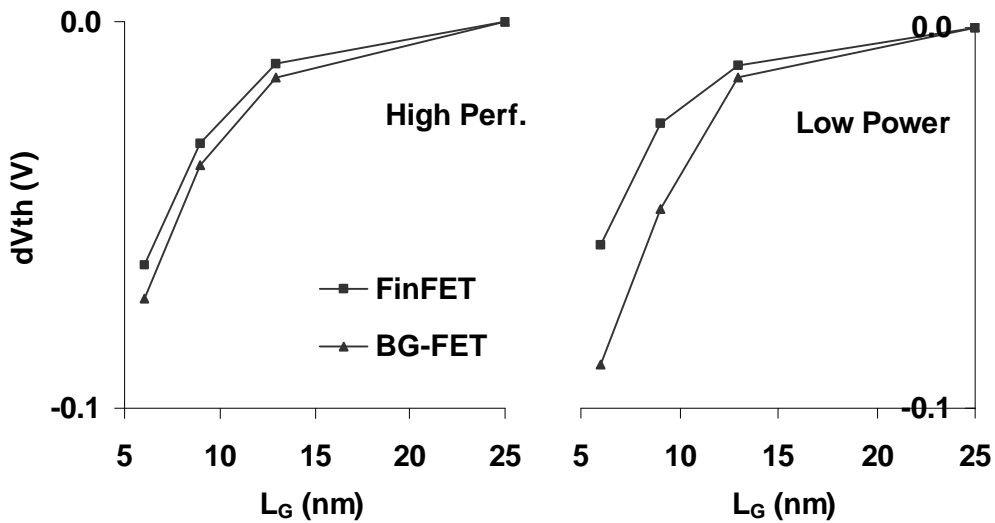


Figure 3.5 - The BG-FET devices show similar  $V_{TH}$ -rolloff behavior to the DG-FET devices. The low power and high-performance devices show similar  $V_{TH}$ -roll off.

In comparing short-channel effects,  $V_{TH}$  roll-off (

Figure 3.5) and the sensitivity of  $V_{TH}$  to  $T_{Si}$  variations (Figure 3.6) for the BG-FET and the FinFET devices are similar. The DG-FET shows slightly better roll-off and lower  $T_{Si}$  sensitivity, because it has the thickest Si body.

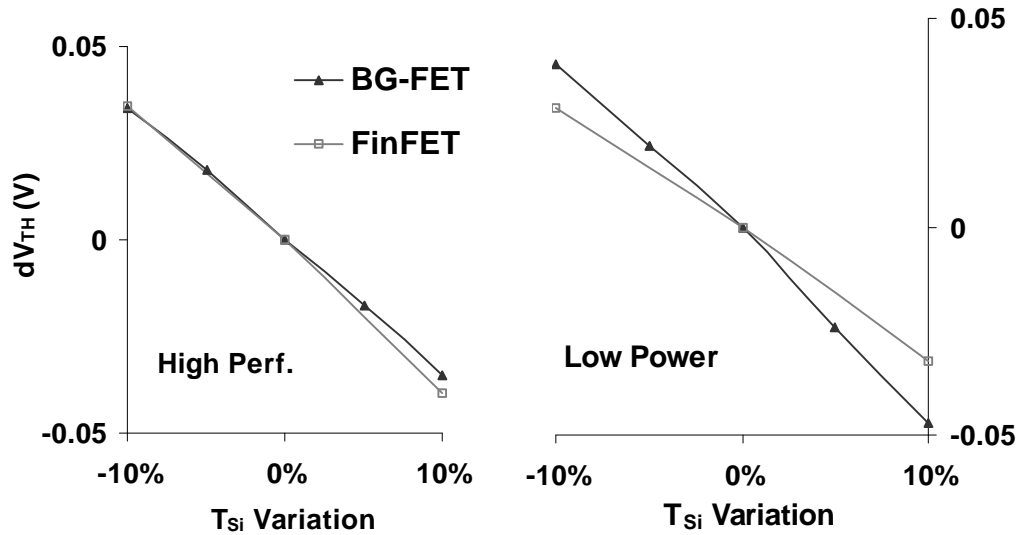


Figure 3.6 - The BG-FET and the DG-FET devices show similar sensitivity to variations in  $T_{Si}$  for both HP and LP designs.

The BG-FET has slightly larger inversion gate capacitance as compared to the DG-FET (Figure 3.7) due to its increased carrier confinement due to the applied back-gate bias resulting in a quantum-mechanical charge centroid location that is closer to the gate oxide interface. The BG-FET needs to have a slightly longer  $L_{EFF}$  as compared to the DG-FET to achieve the same SCE, resulting in a reduced overlap capacitance.

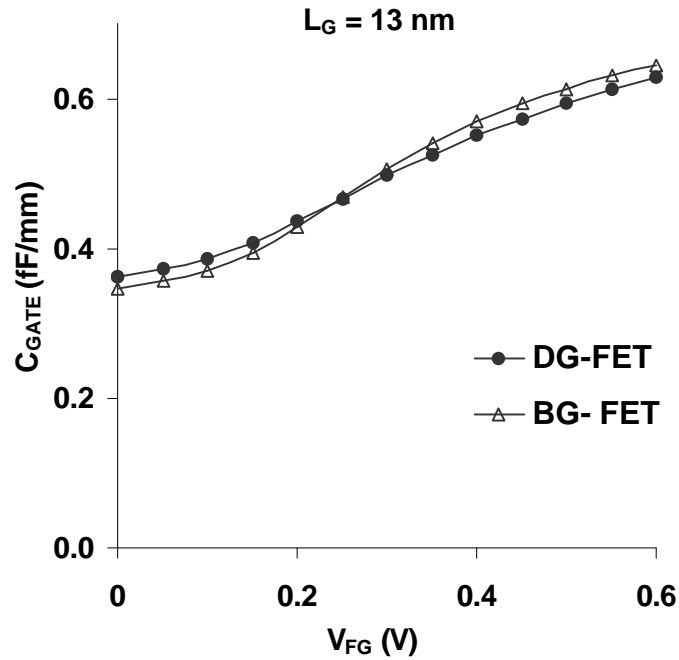


Figure 3.7 - The gate capacitance is similar for BG-FET and DG-FET devices, thus, the intrinsic delay,  $t_{p0}$ , scales with  $I_{ON}$ .

### 3.5 Circuit design benefits of BG-FETs

Adaptive supply- and threshold-voltage scaling can be used to minimize energy dissipation as delay requirements of a circuit change. Deeply scaled bulk-Si MOSFETs have limited  $V_{TH}$  tuning range due to reduced body effect and reduced  $V_{DD}/V_{TH}$  ratios [6, 7]. The  $V_{TH}$  of DG-FET devices cannot be dynamically changed. The  $V_{TH}$  tunability of deeply scaled BG devices makes them attractive for achieving minimal energy over a wide range of target frequencies.

Adaptive body biasing can be used to set the optimum  $V_{TH}$  for each die so as to compensate for variations in chip performance or power dissipation [6, 7]. The  $V_{TH}$  of the NMOS/PMOS devices in each die is therefore controlled not only by gate workfunction and channel length engineering but also by the application of the appropriate forward or

reverse back-gate bias. Dies that are too slow and fail to meet the performance target need to be forward biased, thereby increasing the die operating frequency and the overall die leakage, whereas those that leak excessively have to be reverse biased, reducing the operating frequency as well. The goal of the ABB is to find the optimum PMOS/NMOS  $V_{TH}$  combination that maximizes the die frequency while meeting the leakage constraint.

Dynamic voltage scaling (DVS) [17] can be used to reduce the dynamic power dissipation because of the quadratic dependence of switching power on  $V_{DD}$ . As  $V_{DD}$  is scaled, the device currents are degraded due to a reduced gate overdrive,  $V_{GS}-V_{TH}$ , leading to slower switching speeds. This is the only power saving technique that can be applied to DG-FETs such as the FinFET, which have no external  $V_{TH}$  control capability. This interdependence between dynamic power and switching speeds can be broken by using a combination of DVS and ABB.  $V_{DD}$  can be scaled to save switching power and the  $V_{TH}$  can be lowered correspondingly to maintain enough gate overdrive to retain the switching speed. However, reducing the  $V_{TH}$  increase the leakage current of the transistors significantly. Therefore, there exists a clear tradeoff between the static power dissipation (from lowering  $V_{TH}$ ) and the active power (from lowering  $V_{DD}$ ) for a given application, leading to the existence of an optimal  $V_{DD}$  and  $V_{TH}$  combination that requires the lowest energy to perform a given task [4, 18].

Figure 3.8 demonstrates an example system, where adaptive  $V_{DD}$  and  $V_{TH}$  control of BG-FETs achieves wider energy scalability spanning the range of both HP/LP DG-FETs. While the highest performance achievable by BG-FETs is lower than that of HP DG-FETs, the minimum energy approaches that of the LP DG-FETs when the

computational throughput is reduced significantly. Thus the BG-FET spans a wide range of E-D space and is the energy optimal device for intermediate frequencies. [12]

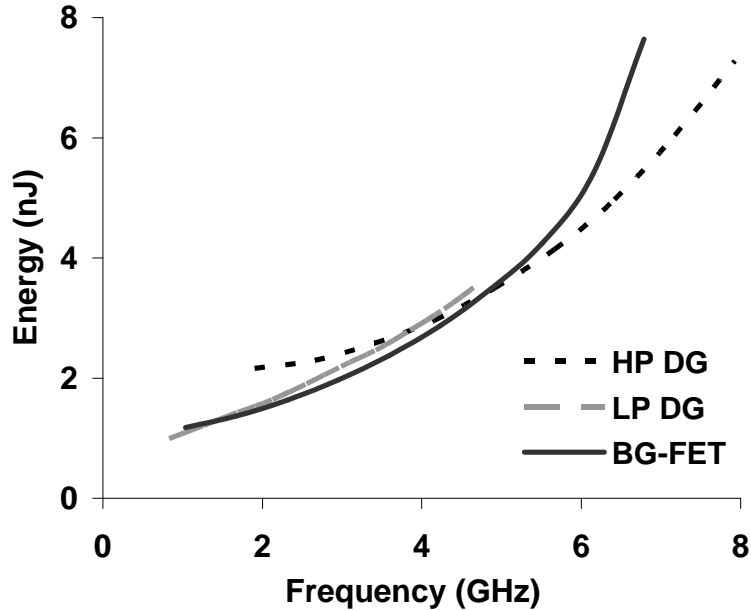


Figure 3.8 - Dynamic voltage scaling of DG-FETs and BG FETs at  $L_G = 13\text{nm}$ . With back-gate bias adjusted as voltage is scaled, the BG-FETs are able to achieve higher performance than the low-power DG-FET and lower energy than the HP DG-FET.

Active leakage control [19] implemented with BG devices allows a circuit to benefit from the low sleep-state leakage while still having performance that is determined by the active-state  $I_{ON}$ . The energy penalty for placing a BG device in the sleep state is the switched capacitance of the back gate, and it can be done in a single cycle. For a bulk-Si MOSFET, switching a large well capacitance incurs a significant layout, energy and delay penalty. Since the benefits of the BG-FET device (Figure 3.2) going into a deeper sleep is retained with scaling into the sub-10nm regime, it is well suited for leakage control in future systems. In our simulations the maximum applied negative back bias was limited to  $-V_{DD}$ ; in practical systems it can be made more negative.

Circuit Parameters	Value
Logic depth	375 CV/l
Gate area	2.4 mm <sup>2</sup>
Activity	10%
% Core sleep	30%

Table 3-2: Example system @  $L_G = 13\text{nm}$

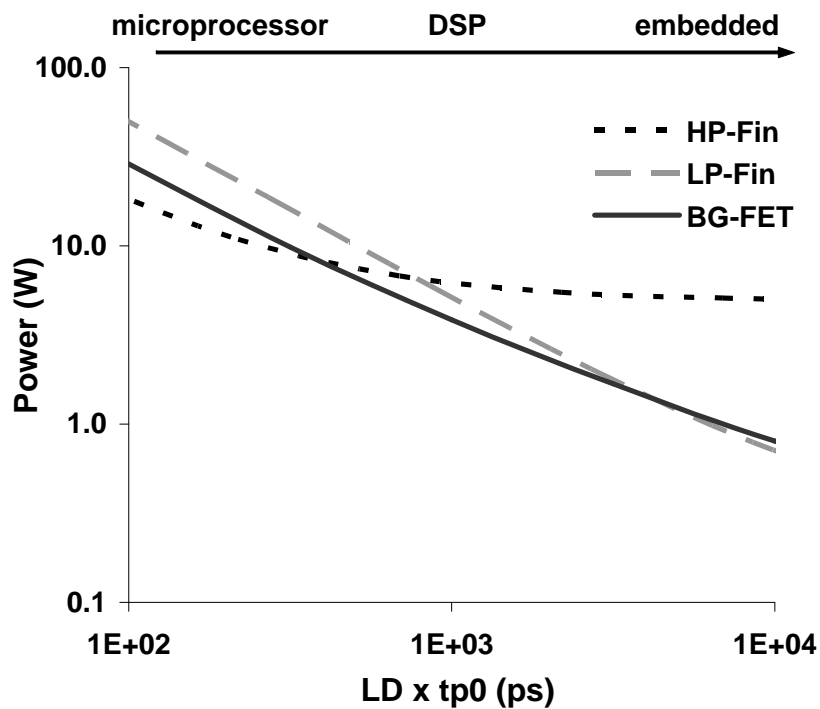


Figure 3.9: Minimum power envelope with changing logic depth in the example system (Table 3-2). The envelope represents the minimum power achievable through a combination of voltage scaling and back-gate biasing to adjust  $V_{TH}$ .

Figure 3.9 illustrates E-D trade-offs with varying logic depths in an example system implemented with both DG-FETs and BG-FETs. BG-FET implementations make use of adaptive threshold control and active leakage control in addition to  $V_{DD}$  adjustment

to achieve a wider range of optimality. The minimum power envelope for the BG-FETs lies in between that of the HP and LP FinFETs. Both Figure 3.8 and Figure 3.9 illustrate the capability of the BG-FETs to achieve delays similar to a HP DG-FET, and attain the low power of LP DG-FETs at low operating frequencies.

A multi- $V_{TH}$  DG-FET technology with more than three  $V_{TH}$  values can potentially outperform BG-FETs, but the benefit of BG-FET technology is in providing a single technology solution to meet different target applications with different throughput requirements.

### **3.6 Conclusions**

Power dissipation of scaled high performance ICs will be controlled by utilizing more than one type of transistor together with device, design and architectural techniques. This chapter presents the design of energy-delay optimized BG-FETs, and discusses the effectiveness of back-gate biasing to control the leakage current. It is demonstrated that BG-FETs exhibit power savings benefits over double-gate MOSFETs that increase with scaling into the sub-10 nm regime. Energy vs. delay (E-D) optimization shows that BG-FETs can span a wide range in E-D space, making it possible to have a single-device solution to meet high performance and low power needs through adaptive supply and threshold voltage biasing.



### 3.7 References

- [1] J. M. Rabaey, A. Chandrakasan, and B. Nikolic, *Digital Integrated Circuits*, 2 ed: Prentice Hall, 2002.
- [2] "International Technology Roadmap for Semiconductors, 2005 ed," <http://www.itrs.net/Links/2005ITRS/Home2005.htm>.
- [3] B. Nikolic, L. Chang, and T.-J. King, "Performance of Deeply-Scaled, Power-Constrained Circuits," Proc. International Conference on Solid State Devices and Materials, Tokyo, 2003,154-155.
- [4] R. W. Brodersen, M. A. Horowitz, D. Markovic, B. Nikolic, and V. Stojanovic, "Methods for true power minimization," Proc. 2002 IEEE/ACM International Conference on Computer Aided Design (ICCAD). San Jose, CA, 2002
- [5] J. T. Kao and A. P. Chandrakasan, "Dual-threshold voltage techniques for low-power digital circuits," *IEEE Journal of Solid-State Circuits*, vol. 35, 2000, pp. 1009-18.
- [6] A. Keshavarzi, S. Ma, S. Narendra, B. Bloechel, K. Mistry, T. Ghani, S. Borkar, and V. De, "Effectiveness of reverse body bias for leakage control in scaled dual  $V_t$  CMOS ICs," Proc. ISLPED'01: Proceedings of the 2001 International Symposium on Low Power Electronics and Design. Huntington Beach, CA, 2001
- [7] J. W. Tschanz, J. T. Kao, S. G. Narendra, R. Nair, D. A. Antoniadis, A. P. Chandrakasan, and V. De, "Adaptive body bias for reducing impacts of die-to-die and within-die parameter variations on microprocessor frequency and leakage," Proc. 2002 IEEE International Solid-State Circuits Conference. Digest of Technical Papers. San Francisco, CA, 2002

- [8] D. Liu and C. Svensson, "Trading speed for low power by choice of supply and threshold voltages," *IEEE Journal of Solid-State Circuits*, vol. 28, 1993, pp. 10-17.
- [9] T. Kuroda, K. Suzuki, S. Mita, T. Fujita, F. Yamane, F. Sano, A. Chiba, Y. Watanabe, K. Matsuda, T. Maeda, T. Sakurai, and T. Furuyama, "Variable supply-voltage scheme for low-power high-speed CMOS digital design," Proc. 1997 Custom Integrated Circuits Conference. Santa Clara, CA, 1998
- [10] K. Nose and T. Sakurai, "Optimization of  $V_{DD}$  and  $V_{TH}$  for low-power and high-speed applications," Proc. Proceedings of ASP-DAC2000: Asia and South Pacific Design Automation Conference 2000. Yokohama, Japan. IEEE Circuits & Syst. Soc.. ACM SIGDA. IEICE of Japan. IPSJ (Inf. Process. Soc. Japan). 25-28 Jan. 2000, 2000
- [11] T. Chen and S. Naffziger, "Comparison of adaptive body bias (ABB) and adaptive supply voltage (ASV) for improving delay and leakage under the presence of process variation," *IEEE Transactions on Very Large Scale Integration (VLSI) Systems*, vol. 11, 2003, pp. 888-99.
- [12] S. Balasubramanian, J. L. Garrett, V. Vidya, B. Nikolic, and T. J. King, "Energy-delay optimization of thin-body MOSFETs for the sub-15 nm regime," Proc. 2004 IEEE International SOI Conference. Charleston, SC, 2004
- [13] "Taurus-Device, v. 2002.4," Synopsys Inc., 2002.
- [14] D. J. Frank, Y. Taur, and H.-S. P. Wong, "Generalized scale length for two-dimensional effects in MOSFETs," *IEEE Electron Device Letters*, vol. 19, 1998, pp. 385-7.

- [15] S. Balasubramanian, L. Chang, B. Nikolic, and T.-J. King, "Circuit-performance implications for double-gate MOSFET scaling below 25 nm," Proc. Silicon Nanoelectronics Workshop, Kyoto, Japan, 2003
- [16] J. L. Garrett, "Compact models for exploring energy-delay tradeoffs in deeply-scaled CMOS digital design," Dept. of Electrical Engineering and Computer Sciences - M.S. Report, University of California, Berkeley 2004.
- [17] T. D. Burd and R. W. Brodersen, "Energy efficient CMOS microprocessor design," Proc. Proceedings of the Twenty-Eighth Annual Hawaii International Conference on System Sciences. Wailea, HI, 1995
- [18] V. Stojanovic, D. Markovic, B. Nikolic, M. A. Horowitz, and R. W. Brodersen, "Energy-delay tradeoffs in combinational logic using gate sizing and supply voltage optimization," Proc. ESSCIRC 2002. Proceedings of the 28th European Solid-State Circuit Conference. Firenze, Italy. 24-26 Sept. 2002, 2002
- [19] J. W. Tschanz, S. G. Narendra, Y. Ye, B. A. Bloechel, S. Borkar, and V. De, "Dynamic sleep transistor and body bias for active leakage power control of microprocessors," *IEEE Journal of Solid-State Circuits*, vol. 38, 2003, pp. 1838-45.

# Chapter 4 : Design of back-gated FDSOI devices

## 4.1 Introduction

Thin-body (fully depleted) SOI MOSFETs are promising to continue CMOS technology scaling in the sub 45-nm regime, because they provide better control of short-channel effects (SCE) as compared with the classic bulk-Si MOSFET. For good electrostatic integrity, i.e., the lateral dimensions of the device need to be much longer than the vertical dimensions of the device. The degree of SCE control is often characterized by the scale length,  $\lambda$ , which is a measure of the effective thickness of the MOSFET channel in the direction transverse to current flow.

A new scale-length formula to capture two-dimensional (2-D) electrostatic effects in independently gated FDSOI MOSFETs has been derived in this chapter. The scale length accounts for the effective location of the conduction path of sub-threshold leakage and thereby captures the back-gate bias dependence of short channel effects and sub-threshold swing. In order to account for quantum-mechanical effects in thin Si channels, a quantum-corrected, bias-dependent effective conduction path model is proposed. The scale length model can then be used to model the SCE in back-gated FDSOI devices (BG-FDSOI) devices and guide device design to improve their performance. It is shown that reverse back-gate biasing reduces the scale length by pushing the leakage path closer to the front channel surface, thereby improving control of short-channel effects. We

therefore propose the use of reverse back-gate biasing for active-mode operation to relax the body thinness requirement for FDSOI MOSFETs, to make it comparable to that for the FinFET, i.e.,  $T_{Si} \sim (2/3) L_G$ . The performance of such a BG-FDSOI MOSFET with a relaxed body thickness requirement can therefore approach that of a FinFET of the same body thickness, with comparable SCE. Also, BG biasing can be used to compensate for  $V_{TH}$  shifts due to process-induced variations.

## 4.2 Background - Scale length of Thin-Body MOSFETs

The potential inside the channel depletion region of a bulk-Si MOSFET is controlled by the four terminals of the device: gate, body contact, source and drain. The control of the channel from the source/drain regions is undesirable and should be minimized. Two-dimensional effects can be characterized by the control of the channel potential by the source/drain regions relative to the gate and substrate or back-gate contact. When the horizontal dimension, i.e., the channel length, is at least twice as long as the vertical dimension, (a combination of  $T_{OX}$  and the depletion width),  $X_{DEP}$ , the device behaves like a long-channel MOSFET, with its threshold voltage insensitive to channel length and drain bias. For channel lengths shorter than that, the 2D effect becomes significant, and the minimum surface potential ( $F_S$ ), which determines the threshold voltage, is increasingly controlled by the drain than by the gate. For good control of SCE effects, the scale length,  $I$ , which describes how thin the MOSFET is in the vertical dimension, needs to be small, i.e.,  $L_{EFF}$  or  $L_G \gg I$ . A large scale length,  $I$ , indicates strong SCEs that degrade device behavior.

A general 2-D scale length formula has been derived by Frank *et.al.* [1] for thin-body devices, but the solution form is implicit and hard to use except for the lowest order

term. An approximate, but closed form scale length for double-gate (DG) thin-body MOSFETs was proposed by Suzuki *et al.* [2], assuming that leakage current flows along the center of the body. Chiang [3] generalized the scale length formula in [4] to account for leakage current flowing along an effective conduction path located at a distance  $d_{EFF}$  from the center of the body, or the most probable leakage path [5]. Avci [6] proposed a scale length formula from [2] for a back-gated (BG) MOSFET, in which the front and back gates are independently biased, assuming that leakage flows along the front channel surface. In this chapter, we generalize the scale length formula for a lightly doped BG MOSFET to be a function of  $d_{EFF}$ , which depends on the back-gate bias and back oxide thickness.

### 4.3 Derivation of Quantum-Corrected Effective Conduction Path

The scale length is extracted by formulating the 2-D Poisson's equation along the effective conduction path,  $d_{EFF}$ , which is the weighted 'centre of gravity' of subthreshold current. When a reverse bias applied on the back-gate, the channel charge is quite small arising from the lack of significant depletion and inversion charge, leading to linear band bending in the channel or a constant transverse electric field,  $e$ . The scale length model derived here captures changes in SCE through the bias-dependence of  $d_{EFF}$ . In BG-FDSOI MOSFETs with a thin silicon body, the derivation of a quantum-corrected effective conduction path becomes important and is shown below.

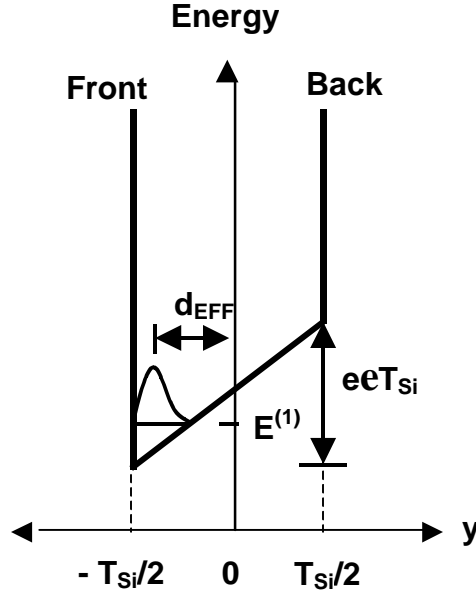


Figure 4.1: The effective conduction path,  $d_{EFF}$ , corresponds to the charge of the electron wavefunction. The vertical field across the channel sets up a trapezoidal quantum well. As the confining electric field increases, the conduction path gets closer to the interface.

For an infinite rectangular quantum well with an applied electric field,  $\epsilon$ , the exact wavefunction are based on the Airy functions. This form of the solution is hard to manipulate mathematically to derive other dependencies and the principle of variations can be used to derive a simpler, but approximate solution.

If the exact wavefunction solution to the Schrödinger equation cannot be found, then the variational method can be used start with any normalized wavefunction that satisfies the boundary conditions. For that initial guess, say  $\Psi$ , it turns out that the expectation value of the Hamiltonian,  $H$ , i.e., the Eigen energy, for the guessed wavefunction will always be greater than the actual ground state energy. Or in other words, if the approximate wavefunction is a function of a number of parameters, varying these parameters until the expectation value of  $H$  is a minimum, minimizes the error for

that form of the wavefunction. The result is an upper limit for the ground state energy of the system, which is likely to be close to actual ground state energy if the trial vector resembles the eigenvector. A variational wave function solution of the following form has been used for the case of the triangular quantum well. [7].

$$\Psi(x) = N(\mathbf{b}) \cos \frac{\mathbf{p}x}{T_{Si}} \exp \left[ -\mathbf{b} \frac{x}{T_{Si}} \right] \quad (\text{Eq. 4-1})$$

where  $\beta$  is the variational parameter, and  $N(\beta)$  is the normalization constant. The ground state energy Eigen values can then be written based on the Hamiltonian,  $H = H_0 + eey$  as,

$$E(\mathbf{b}) = E^{(1)} \left[ 1 + \frac{\mathbf{b}^2}{\mathbf{p}^2} + \mathbf{h} \left( \frac{1}{2\mathbf{b}} + \frac{\mathbf{b}}{\mathbf{b}^2 + \mathbf{p}^2} - \frac{1}{2} \coth(\mathbf{b}) \right) \right] \quad (\text{Eq. 4-2})$$

where  $E^{(1)} = \frac{\hbar^2}{8m^* T_{Si}^2}$ , the ground state energy for the rectangular quantum well, and the

dimensionless energy,  $\mathbf{h} = \frac{e e T_{Si}}{E^{(1)}}$ . The optimal value of  $\beta$  is obtained by minimizing  $E(\beta)$  w.r.t  $\beta$ , i.e., by setting  $dE/d\beta = 0$ ,

$$\frac{dE}{d\mathbf{b}} = E^{(1)} \left[ \frac{2\mathbf{b}}{\mathbf{p}^2} + \frac{\mathbf{h}}{2} \left( \csc h^2(\mathbf{b}) - \frac{3\mathbf{b}^4 + \mathbf{p}^4}{\mathbf{b}^2(\mathbf{b}^2 + \mathbf{p}^2)^2} \right) \right] = 0 \quad (\text{Eq. 4-3})$$

The analytical solution to this equation is hard to find, and the system was solved

numerically [7]. But the limits of this function are known, as  $\eta \rightarrow 0$ ,  $\mathbf{b} = \left( \frac{\mathbf{p}^2}{6} - 1 \right) \mathbf{h}$ , and

as  $\eta \rightarrow \infty$ ,  $\mathbf{b} = (6\mathbf{p}^2 \mathbf{h})^{1/3}$ . It is to be noted that the optimal value of  $\beta$  depends uniquely only on  $\eta$ , resulting in an universal relation.



$$h = \frac{b}{\left(\frac{p^2}{6} - 1\right)} + \frac{b^3}{6p^2} \quad (\text{Eq. 4-4})$$

The real solution to the cubic equation (Eq. 4-4) can be solved analytically and is verified to match the numerical solution to (Eq 4-3). Knowing  $\beta$ , we can derive  $d_{EFF}$  as the expectation value of the position operator,  $|y\rangle$

$$d_{EFF} = \frac{\int_{-T_{Si}/2}^{T_{Si}/2} \psi^*(y) y \psi(y) dy}{\int_{-T_{Si}/2}^{T_{Si}/2} \psi^*(y) \psi(y) dy} = T_{Si} \left( \frac{1}{2b} + \frac{b}{b^2 + p^2} - \frac{1}{2} \coth(b) \right) \quad (\text{Eq. 4-5})$$

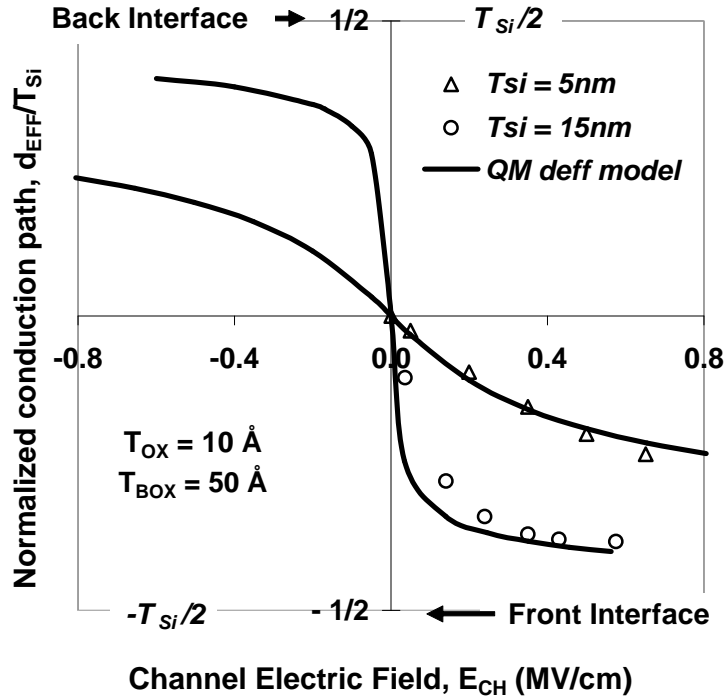


Figure 4.2: The effective conduction path,  $d_{EFF}$ , changes with the vertical channel electric field. As the confining field increases, the conduction path gets closer to the interface, thereby improving gate control and reducing SCEs. A thicker back-oxide degrades  $\beta_{BG}$ , but this can be negated by pushing the carriers closer to the interface with a larger vertical field.

The effective conduction path,  $d_{EFF}$ , is the expectation value of the charge centroid of the electron wavefunction as measured from the center of the body. Figure 4.2 shows the change in the  $d_{EFF}$  as a function of the applied electric field,  $e$ , and as expected, QM effects prevent the  $d_{EFF}$  from reaching all the way to the interfaces. The sensitivity of  $d_{EFF}$  to channel electric field becomes smaller with  $T_{Si}$  scaling, indicating that a thinner silicon body behave more like a rectangular well and the effectiveness of a vertical electric field in pushing the carriers to the surface is diminished. Thus, QM effects are expected to reduce the benefits of back-gate biasing in extremely scaled devices.

#### 4.4 Scale Length Derivation for BG-FDSOI devices

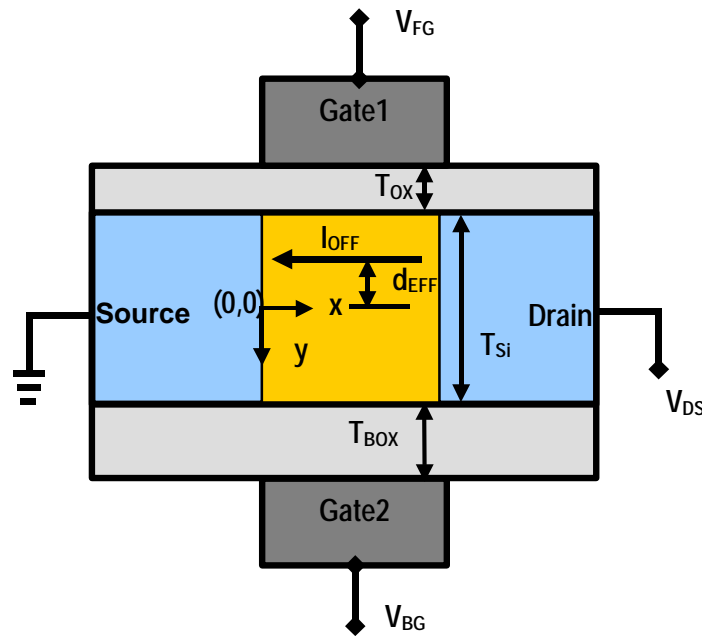


Figure 4.3 Schematic cross-sectional view of a back-gated (BG) FDSOI MOSFET. The front and back gates can be independently biased and may have different work function values. Note that the y-axis is along the vertical direction with its origin located at the center of the silicon body.

This scale length model attempts to quantify the short-channel behavior of a fully depleted transistor with back-gate biasing. The origin of the coordinate system used is set at the source end along the center of the Si body (Figure 4.3). The label  $d_{EFF}$  refers to the effective conduction path, measured from the center of the body. Also, the source potential is used as the reference point, i.e.,  $V_S=0$ . The following assumptions and approximations are made to set up the problem:

1. Since only the short-channel effects are solved here, the MOSFET is biased in the subthreshold region, and the full depletion approximation is used inside the fully depleted body.
2. Ideal abrupt source/drain junctions are assumed, so that the boundaries between the source/drain and channel do not move with bias.
3. In a FDSOI device, the body is so thin that vertical doping engineering becomes impractical. Therefore, undoped channel is assumed.
4. Also, metallic gates with appropriate workfunctions are assumed in order to set the correct  $V_{TH}$  and to ignore gate depletion effects that change the EOT
5. The electrical field in the gate dielectric and thin BOX is assumed to be strictly vertical. The 2D effect of the gate dielectric and back-oxide will be modeled using a quasi-2D approximation similar to they way it is modeled in [8].

The 2-D Poisson's equation for the potential  $F(x, y)$  in a BG FDSOI MOSFET is

$$\frac{\partial^2 \mathbf{F}(x, y)}{\partial x^2} + \frac{\partial^2 \mathbf{F}(x, y)}{\partial y^2} = \frac{qN_A}{\mathbf{e}_{Si}} \quad (\text{Eq. 4-6})$$

For constant channel doping, the solution to the potential profile can be given by a parabolic profile

$$F(x, y) = C_1(x) + C_2(x)y + C_3(x)y^2 \quad (\text{Eq. 4-7})$$

The electric field continuity at the front and back surface can be written in terms of their respective potentials  $F_f(x) = F(x, -T_{Si}/2)$  and  $F_b(x) = F(x, T_{Si}/2)$  as follows,

$$\left. \frac{\partial F(x, y)}{\partial y} \right|_{T_{Si}/2} = -\frac{\mathbf{e}_{OX}}{\mathbf{e}_{Si}} \frac{\mathbf{F}_b(x) - V_{gb,eff}}{T_{BOX}}, \text{ where } V_{gb,eff} = V_{gb} - V_{fb} \quad (\text{Eq. 4-8})$$

$$\left. \frac{\partial F(x, y)}{\partial y} \right|_{-T_{Si}/2} = \frac{\mathbf{e}_{OX}}{\mathbf{e}_{Si}} \frac{\mathbf{F}_f(x) - V_{gf,eff}}{T_{OX}}, \text{ where } V_{gf,eff} = V_{gf} - V_{fb} \quad (\text{Eq. 4-9})$$

Using Eq. 4-8 and 4-9 to express the solution coefficients in Eq. 4-7 in terms of  $F_f(x)$  and  $F_b(x)$ ,

$$C_2(x) = \frac{\mathbf{F}_b(x) - \mathbf{F}_f(x)}{T_{Si}} = \frac{\mathbf{e}_{OX} (T_{OX} (V_{gb} - \mathbf{F}_b(x)) - T_{BOX} (V_{gf} - \mathbf{F}_f(x)))}{2\mathbf{e}_{Si} T_{OX} T_{BOX}} \quad (\text{Eq. 4-10})$$

$$C_3(x) = \frac{\mathbf{e}_{OX} (T_{OX} (V_{gb} - \mathbf{F}_b(x)) + T_{BOX} (V_{gf} - \mathbf{F}_f(x)))}{2\mathbf{e}_{Si} T_{Si} T_{OX} T_{BOX}} \quad (\text{Eq. 4-11})$$

$$C_1(x) = \frac{\mathbf{F}_b(x) + \mathbf{F}_f(x)}{2} - C_3(x) \left( \frac{T_{Si}}{2} \right)^2 \quad (\text{Eq. 4-12})$$

The back surface potential,  $F_b(x)$  can be rewritten in terms of the front surface potential  $F_f(x)$  as follows

$$\mathbf{F}_b(x) = \frac{\frac{T_{Si}}{2} \mathbf{e}_{OX} (V_{gb} T_{OX} - V_{gf} T_{BOX}) + \left( T_{OX} \mathbf{e}_{Si} + \frac{T_{Si}}{2} \mathbf{e}_{OX} \right) T_{BOX} \mathbf{F}_f(x)}{T_{OX} \left( \frac{T_{Si}}{2} \mathbf{e}_{OX} + T_{BOX} \mathbf{e}_{Si} \right)} \quad (\text{Eq. 4-13})$$

Based on eqs. (4-10) – (4-13), the coefficients  $C_1(x)$ ,  $C_2(x)$ , and  $C_3(x)$  can be expressed in terms of  $F_f(x)$  alone. With the coefficients known, the potential along the effective

conduction path  $F_{deff}(x) = F(x, d_{EFF})$ , can then be written in terms of  $F_f(x)$ . This can then be inverted to express  $F_f(x)$  in terms of  $F_{deff}(x)$  as follows,

$$\mathbf{F}_f(x) = \frac{\left\{ \mathbf{e}_{ox}^2 T_{Si} \left( \left( \frac{T_{Si}}{2} \right)^2 - d_{eff}^2 \right) + \mathbf{e}_{ox} \mathbf{e}_{Si} T_{BOX} \left( \frac{3T_{Si}}{2} - d_{eff} \right) \left( \frac{T_{Si}}{2} + d_{eff} \right) \right\} V_{gf} - \left( \frac{T_{Si}}{2} + d_{eff} \right)^2 \mathbf{e}_{ox} \mathbf{e}_{Si} T_{OX} V_{gb} + \mathbf{e}_{Si} T_{OX} T_{Si} (\mathbf{e}_{ox} T_{Si} + 2\mathbf{e}_{Si} T_{BOX}) \mathbf{F}_{deff}(x)}{2T_{Si} T_{OX} T_{BOX} \mathbf{e}_{Si}^2 + \mathbf{e}_{ox}^2 T_{Si} \left( \left( \frac{T_{Si}}{2} \right)^2 - d_{eff}^2 \right) + \mathbf{e}_{ox} \mathbf{e}_{Si} \left\{ \left( \frac{3T_{Si}}{2} - d_{eff} \right) \left( \frac{T_{Si}}{2} + d_{eff} \right) T_{BOX} + \left( \frac{3T_{Si}}{2} + d_{eff} \right) \left( \frac{T_{Si}}{2} - d_{eff} \right) T_{OX} \right\}}$$
 (Eq. 4-14)

Equation (4-7) can now be written in terms of  $F_{deff}(x)$ . Using Eqs. (4-10)-(4-14) and differentiating  $F(x, y)$ , we get

$$\frac{\partial^2 \mathbf{F}(x, y)}{\partial x^2} = \frac{\partial^2 \mathbf{F}_{deff}(x)}{\partial x^2}$$
 (Eq. 4-15)

$$\frac{\partial^2 \mathbf{F}(x, y)}{\partial y^2} = \frac{2\mathbf{e}_{OX} \left[ \left( V_{gf} - \mathbf{F}_{deff} \right) \left( \mathbf{e}_{ox} \left( \frac{T_{Si}}{2} - d_{eff} \right) + \mathbf{e}_{Si} T_{BOX} \right) + \left( V_{gb} - \mathbf{F}_{deff} \right) \left( \mathbf{e}_{ox} \left( \frac{T_{Si}}{2} + d_{eff} \right) + \mathbf{e}_{Si} T_{OX} \right) \right]}{2T_{Si} T_{OX} T_{BOX} \mathbf{e}_{Si}^2 + \mathbf{e}_{ox}^2 T_{Si} \left\{ \left( \frac{T_{Si}}{2} \right)^2 - d_{eff}^2 \right\} + \mathbf{e}_{Si} \mathbf{e}_{ox} \left\{ \left( \frac{3T_{Si}}{2} - d_{eff} \right) \left( \frac{T_{Si}}{2} + d_{eff} \right) T_{BOX} + \left( \frac{3T_{Si}}{2} + d_{eff} \right) \left( \frac{T_{Si}}{2} - d_{eff} \right) T_{OX} \right\}}$$
 (Eq. 4-16)

The Poisson's equation (Eq 4-6) can now be rewritten in the following form:

$$\frac{\partial^2 \mathbf{F}_{deff}(x, y)}{\partial x^2} + \frac{(V_{gb} - \mathbf{F}_{deff})}{\mathbf{I}_b^2} + \frac{(V_{gf} - \mathbf{F}_{deff})}{\mathbf{I}_f^2} = \frac{qN_A}{\mathbf{e}_{Si}}$$
 (Eq. 4-17)

$$\text{with, } \frac{1}{\mathbf{I}_f^2} + \frac{1}{\mathbf{I}_b^2} = \frac{1}{\mathbf{I}_{bg}^2}$$
 (Eq. 4-18)

where  $\mathbf{I}_f$  and  $\mathbf{I}_b$  refer to the scale lengths characterizing front and back gate control

respectively.  $\lambda_{BG}$  is the overall scale length of independent-gate FDSOI device which depends on  $d_{EFF}$  and is given by,

$$I_{BG} = \frac{2T_{Si}T_{OX}T_{BOX}e_{Si}^2 + e_{ox}^2T_{Si}\left\{\left(\frac{T_{Si}}{2}\right)^2 - d_{eff}^2\right\} + e_{Si}e_{ox}\left\{\left(\frac{3T_{Si}}{2} - d_{eff}\right)\left(\frac{T_{Si}}{2} + d_{eff}\right)T_{BOX} + \left(\frac{3T_{Si}}{2} + d_{eff}\right)\left(\frac{T_{Si}}{2} - d_{eff}\right)T_{OX}\right\}}{2e_{ox}(T_{Si}e_{ox} + (T_{OX} + T_{BOX})e_{Si})} \quad (\text{Eq. 4-19})$$

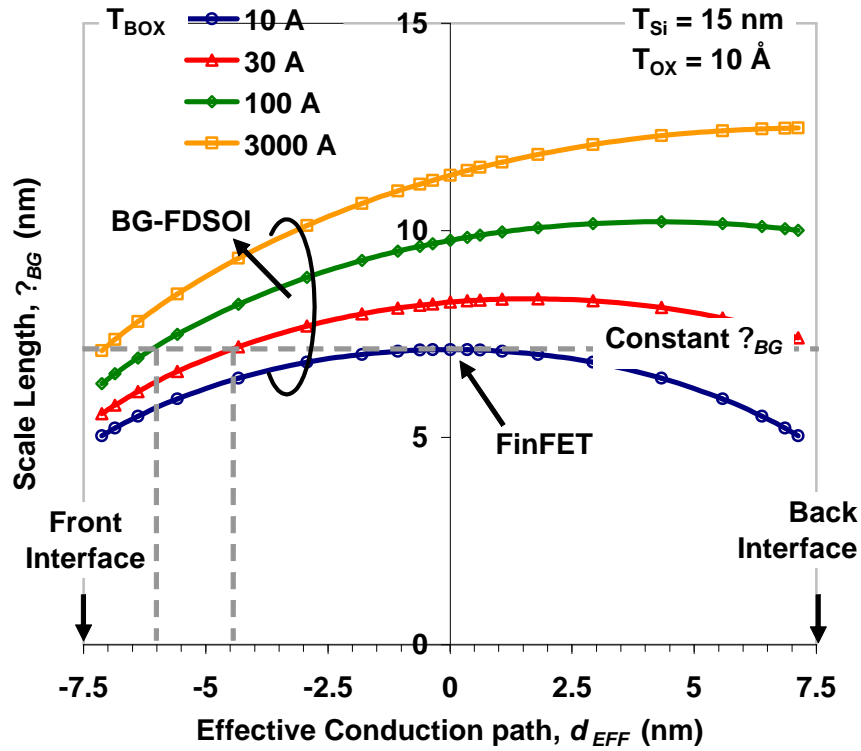


Figure 4.4: Dependence of scale length  $\lambda_{BG}$  on  $d_{EFF}$ . As the effective location of the leakage path moves closer to the front interface (i.e., as  $d_{EFF}$  approaches  $-T_{Si}/2$ ),  $\lambda_{BG}$  decreases and hence the scalability of the FDSOI MOSFET improves. A thicker  $T_{BOX}$  degrades  $\lambda_{BG}$ , but this can be compensated by pushing the leakage path closer to the front interface by applying a larger channel electric field  $E_{CH}$  (Figure 4.2).

Eq. 4-19 expresses the scale length of the BG-FDSOI device,  $L_{BG}$ , as a function of the various device parameters  $T_{OX}$ ,  $T_{Si}$ ,  $T_{BOX}$  and the applied back-gate bias through  $d_{EFF}$ . From Eq. 4-19 it is evident that improvements in the scale length,  $L_{BG}$ , can be achieved by pushing the carriers closer to either the front or the back-gate dielectric interface. However, in order to achieve good transistor drive current characteristics, it is necessary to have  $T_{BOX} > T_{OX}$  so that the coupling from the front gate to the channel is good. For the same reason, a greater improvement in  $L_{BG}$  is achieved by pushing the carriers to the front gate dielectric rather than the back-gate dielectric interface as seen in Figure 4.4.

#### 4.5 Implications of Scale length on BG-FDSOI Device Design

Eq 4-19 can be depicted in the form of a constant-scale-length surface as shown in Figure 4.5. It can be seen that  $T_{OX}$ ,  $T_{BOX}$ , and  $T_{Si}$  can be traded off against each other in achieving a target scale length. It is clear that in order to scale BG-FDSOI from  $L_G = 25\text{nm}$  down to  $13\text{nm}$ , the  $T_{OX}$ ,  $T_{BOX}$ , and  $T_{Si}$  have to be made correspondingly smaller as well. The application of a reverse back-gate bias pushes out the contour to thicker values of  $T_{OX}$ ,  $T_{BOX}$ , and  $T_{Si}$ , thereby increasing the scalability of the FDSOI MOSFET. This improvement in scale length explains the experimental observations that SCE control is improved with reverse-back-gate biasing [9]. Reverse back-gate biasing can therefore be employed as a way to control SCE through its effects on  $d_{EFF}$  in addition to adjusting  $V_{TH}$ , and can potentially be used to relax the body thinness requirement for FDSOI MOSFETs, making them more manufacturable.

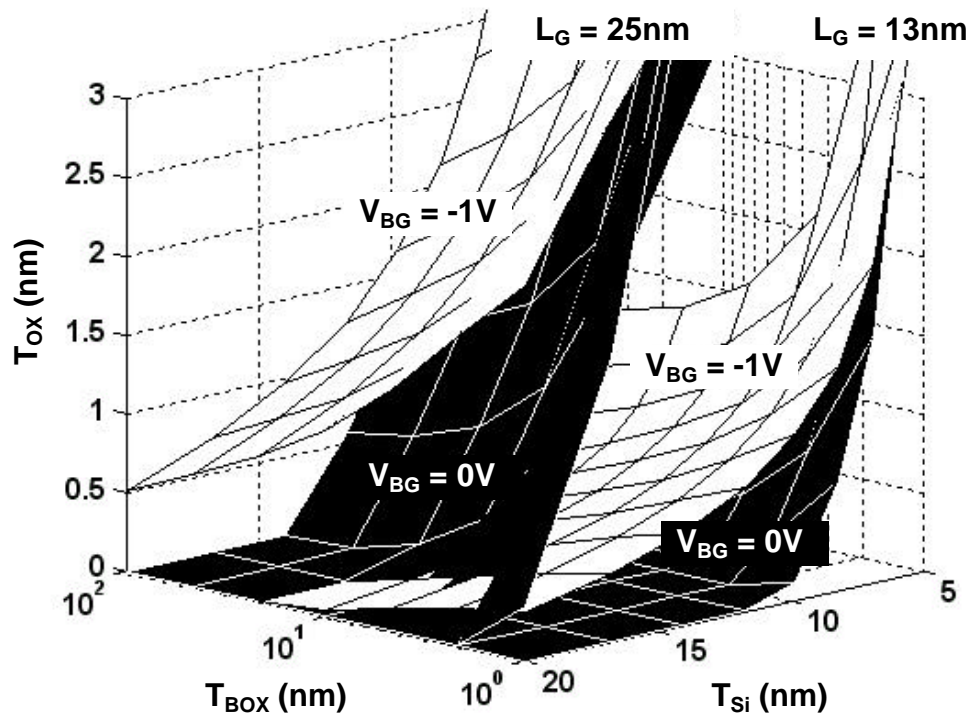


Figure 4.5: 3-D plot of constant scale length contours versus  $T_{OX}$ ,  $T_{Si}$ , and  $T_{BOX}$  for back-gated FDSOI MOSFET's for two different back-gate voltages at the 65nm and 32nm technology nodes. Clearly as the gate length is scaled, smaller  $T_{OX}$ ,  $T_{Si}$ , and  $T_{BOX}$  are needed, but these can be relaxed by applying a reverse back-gate bias, which improves the scalability of the device by pushing out the constant scale length surface.



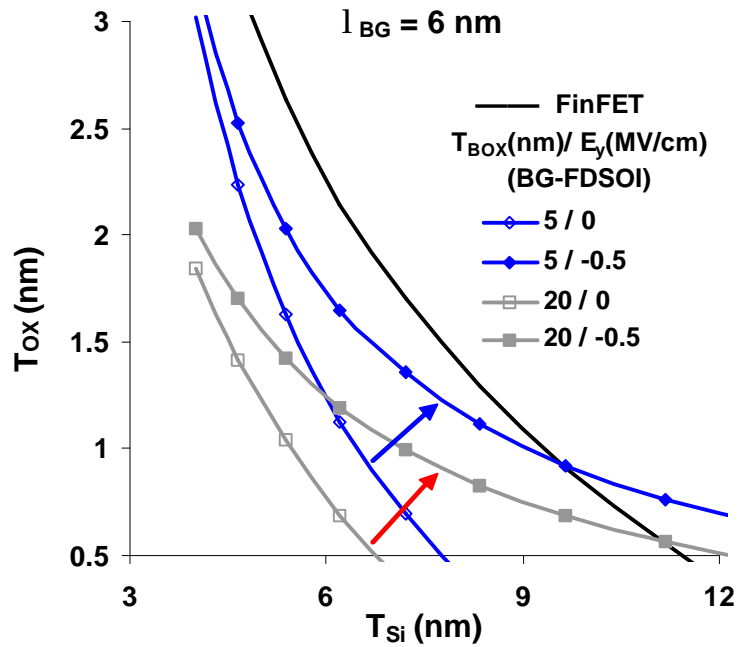


Figure 4.6: 2-D plot of constant scale length curves showing the tradeoff between  $T_{OX}$  and  $T_{Si}$  for a DG MOSFET ( $T_{BOX} = T_{OX}$ ) and for a back-gated FDSOI MOSFET, for two different  $T_{BOX}$  thicknesses. When a reverse back-gate bias is applied ( $E_y = 0.5 \text{ MV/cm}$ ),  $T_{OX}$ ,  $T_{Si}$  and  $T_{BOX}$  requirements can be relaxed as is evident in the pushed out constant- $I_{BG}$  curve (filled symbols – applied bias) to larger values of  $T_{OX}$  and  $T_{Si}$ . A thicker buried oxide (5nm - > 20 nm) degrades  $\beta_{BG}$ , but this can be compensated by applying a larger channel field  $E_{CH}$

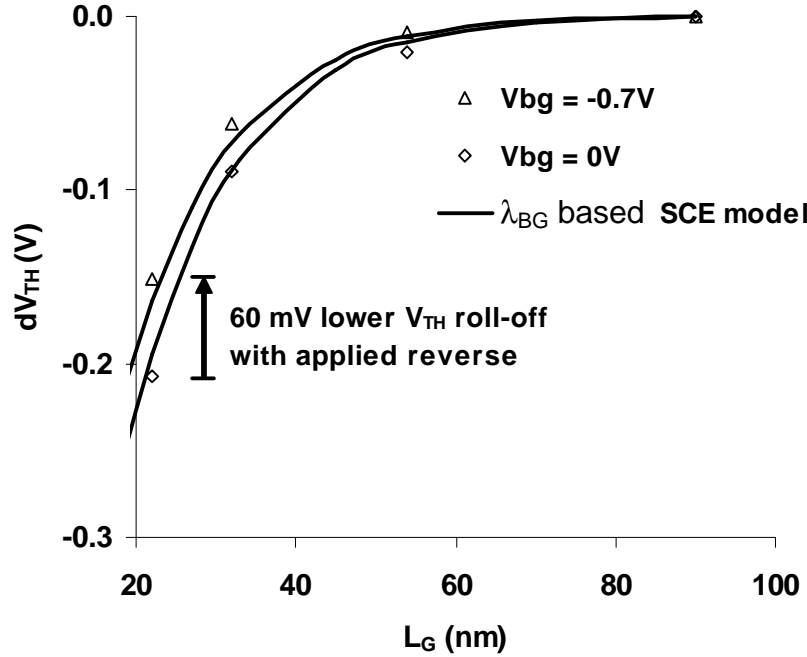


Figure 4.7:  $V_{TH}$  roll-off plot comparing Taurus-Device simulations and SCE model based on the scale length (Eq. 4-19). The plot shows the benefit of reverse back-gate biasing to improve SCE. For specified values of  $T_{OX}$ ,  $T_{BOX}$ ,  $T_{Si}$ , and leakage ( $I_{OFF} = 200$  nA/um, achieved by gate workfunction adjustment), reverse back gate biasing with  $V_{BG} = -0.7V$  improves  $V_{TH}$  roll-off by pushing the leakage path closer to the front interface, as captured by the  $d_{EFF}$  formulation.

Threshold-voltage roll-off and drain-induced barrier lowering can be deduced from the scale length using the same formulation used by Liu *et al.* [8, 10]. It should be noted that, although a thin BOX helps to improve SCE in FDSOI devices by effectively shielding the drain electric field, it can degrade MOSFET sub-threshold swing and hence ON-state current, making the scale length just one of multiple criteria to consider in device design.

## 4.6 Relaxed Body-Thickness Scaling in BG-FDSOI MOSFETs

Short-channel effects (SCE) are well suppressed in a FDSOI MOSFET with undoped channel/body when the body thickness  $T_{Si}$  is less than or equal to one-third of the gate length  $L_G$ . However, as  $L_G$  is scaled to below 20nm in sub-45nm CMOS technologies,  $T_{Si}$  must be scaled to below 5nm, so that parasitic series resistance ( $R_{series}$ ) and threshold voltage ( $V_{TH}$ ) sensitivity to  $T_{Si}$  variation become serious issues. In contrast, the double-gate (DG) MOSFET structure (*e.g.* the FinFET) avoids these issues because the body thinness requirement is less stringent:  $T_{Si} \sim (2/3) L_G$ . However, DG transistor structures such as the vertical FinFET are more challenging to manufacture than the planar FDSOI MOSFET structure.

Back-gate (BG) biasing has been shown to be effective for adjusting  $V_{TH}$  in FDSOI MOSFETs with thin buried oxide (BOX) [11]. Reverse BG biasing suppresses SCE [9, 11-15] in contrast to reverse body biasing of bulk-Si MOSFETs which worsens SCE. This is because the application of a reverse back-gate bias  $V_{BG}$  increases the vertical electric field in the channel  $E_{CH}$ , pushing the off-state leakage path closer to the front channel surface. (Note that the magnitude of  $V_{BG}$  required to achieve the desired  $E_{CH}$  will increase with increasing buried oxide thickness  $T_{BOX}$ .) We therefore propose the use of reverse back-gate biasing for *active-mode* operation to relax the body thinness requirement for FDSOI MOSFETs, to make it comparable to that for the FinFET, *i.e.*,  $T_{Si} \sim (2/3) L_G$ . The performance of such a BG-FDSOI MOSFET with a relaxed body thickness requirement can therefore approach that of a FinFET of the same body thickness, with comparable SCE.

## 4.7 BG-FDSOI MOSFET Design Considerations

Device simulations were carried out using Taurus-Device [16] with drift-diffusion models, the 1-dimensional Schrödinger Equation to account for quantum confinement, and surface mobility models to account for electric-field dependent degradation in mobility. In order to realistically include the effects of parasitic series resistance and capacitance, transistor structures with silicided raised-source/drain regions were simulated (Figure 4.8).

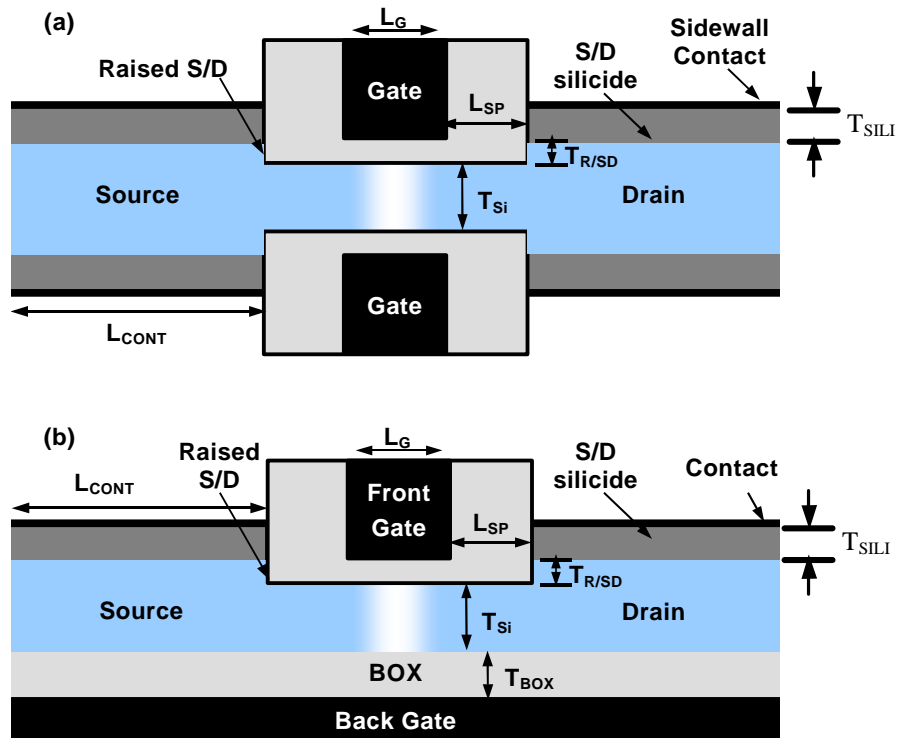


Figure 4.8: Cross-sectional schematic of a) double-gate MOSFET structure b) BG-FDSOI MOSFET structure used for device simulations. The device parameters used are  $L_G = 13\text{nm}$ ,  $T_{Si} = 8\text{nm}$ ,  $T_{OX} = 8\text{\AA}$ ,  $L_{CONT} = 40\text{nm}$ ,  $T_{R/S/D} = 5\text{nm}$ ,  $T_{SILI} = 10\text{nm}$  [17]. For the BG-FDSOI MOSFET, the back gate is  $p^+$  poly-Si for an n-channel device and  $n^+$  poly-Si for a p-channel device.

The aim of this simulation study was to take advantage of the improvement in scalability with reverse BG biasing to design a BG-FDSOI device with the same off-state leakage current, SCE, gate oxide thickness  $T_{OX}$ , and  $T_{Si}$  as that of a DG-MOSFET and to compare their performance, delay, and immunity to variations.

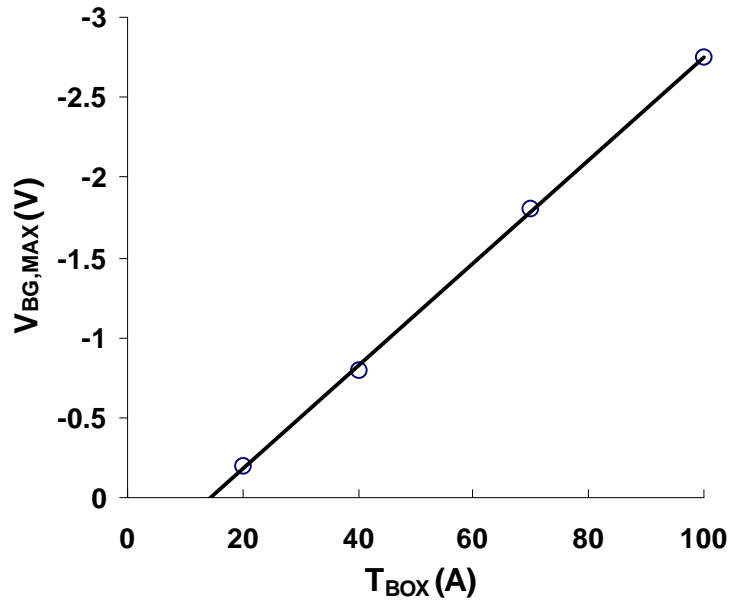


Figure 4.9 : Maximum applicable reverse back-gate bias before the onset of BGIDL, i.e., band-to-band tunneling between the accumulation layer and the reverse-biased drain in BG-FDSOI NMOSFETs.

As  $|V_{BG}|$  is increased, the back channel surface is biased into accumulation, and band-to-band tunneling (BTBT) occurs at the back channel surface between the accumulation layer and drain. This phenomenon can be considered as back-gate induced drain leakage (BGIDL), and it places an upper limit on  $|V_{BG}|$ . This limit increases with  $T_{BOX}$ , since larger  $|V_{BG}|$  is needed to achieve the same degree of energy-band bending in the channel to induce BGIDL for thicker  $T_{BOX}$  (Figure 4.9). It should be noted that BTBT

occurs at a smaller value of  $|E_{CH}|$  in PMOS devices than in NMOS devices, therefore the maximum  $|V_{BG}|$  that can be applied in PMOS BG-FDSOI devices is smaller [18].

For device design optimization,  $|V_{BG}|$  was chosen to be the maximum allowable for  $T_{BOX}$ . (From BGIDL considerations,  $|E_{CH}|$  should not exceed 0.5 MV/cm.) Since  $|V_{BG}|$  is limited, it is difficult for the BG-FDSOI MOSFET to achieve the same degree of SCE control as a FinFET with the same  $T_{Si}$ . Therefore, the BG-FDSOI MOSFET must have a slightly larger electrical channel length  $L_{EFF}$ ; this can be achieved in practice by increasing the offset spacer thickness ( $L_{SP}$ ). The work function of the front (switching) gate electrode and  $L_{EFF}$  were each adjusted so that the BG-FDSOI and FinFET designs meet the leakage current ( $I_{OFF}$ ) specification (300 nA/ $\mu$ m) and the SCE control requirements. In order to achieve the desired  $V_{TH}$  and maximize the effectiveness of BG biasing, it is best to use gates with asymmetric work-function ( $\Phi_M$ ), *e.g.* low- $\Phi_M$  front gate and high- $\Phi_M$  back gate, for an n-channel BG-FDSOI MOSFET.

Using this approach, n-channel and p-channel BG-FDSOI MOSFET designs for  $L_G = 13\text{nm}$ ,  $T_{Si} = 8\text{nm}$ , and  $T_{OX} = 8\text{\AA}$  (same as for FinFET devices) were optimized by adjusting  $T_{BOX}$  and  $L_{EFF}$  to achieve maximum on-state drain current,  $I_{D,SAT}$ , while meeting SCE and  $I_{OFF}$  specifications. The design optimization involves a tradeoff between SCE, parasitic series resistance, and the degree of back-gate coupling. Figure 4.10 shows that the BG-FDSOI MOSFET can achieve an on-state current (per micron effective channel width) that is  $\sim 6\%$  smaller than the FinFET, for a given off-state current (100nA/ $\mu$ m), while its gate capacitance is  $\sim 5\%$  larger than that of the FinFET. The gate capacitance is increased because the built-in electric field pushes the inversion charge centroid closer to the interface, thereby reducing the capacitance equivalent thickness. The on-current is

degraded in comparison to the FinFET due to the increased carrier scattering from the increased transverse electric field.

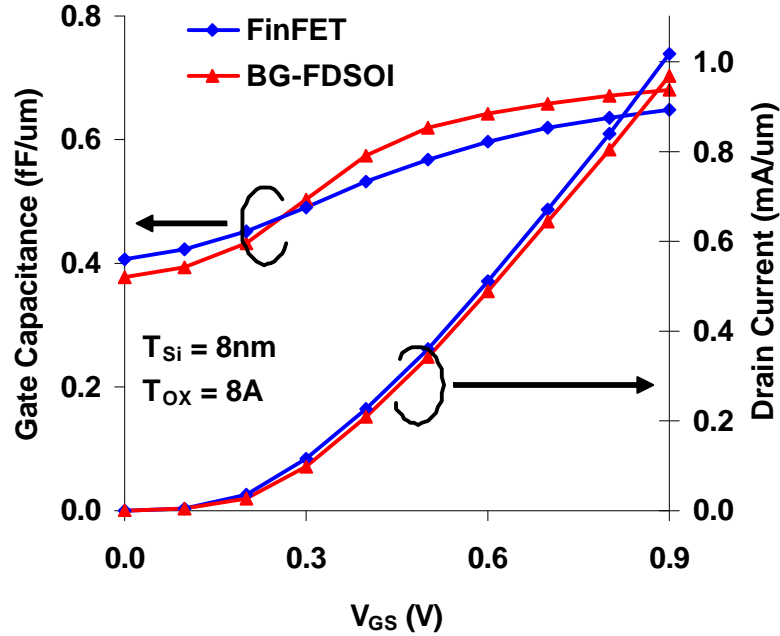


Figure 4.10: Simulated drain current characteristics and gate capacitance of BG-FDSOI vs. double-gate MOSFET (FinFET), for  $L_G = 13nm$ ,  $T_{OX} = 8\text{\AA}$ ,  $T_{Si} = 8nm$ .  $T_{BOX} = 4nm$  for the FDSOI device. The BG-FDOI device has marginally higher gate capacitance and ~6% lower on-state current (for a fixed  $I_{OFF} = 300nA/\mu m$ ).

Figure 4.11 shows that the optimal  $T_{BOX}$  for maximizing  $I_{D,SAT}$  is  $25\text{\AA}$  for a  $13nm$   $L_G$  BG-FDSOI MOSFET. As the  $T_{BOX}$  thickness is increased, SCE are worsened, so  $L_{EFF}$  needs to be longer, at a cost to  $I_{D,SAT}$ . When  $T_{BOX}$  is very thin, SCE are well controlled, but the strong back-gate coupling degrades  $I_{D,SAT}$  due to the capacitive division of the channel potential between the front- and back-gate potentials.

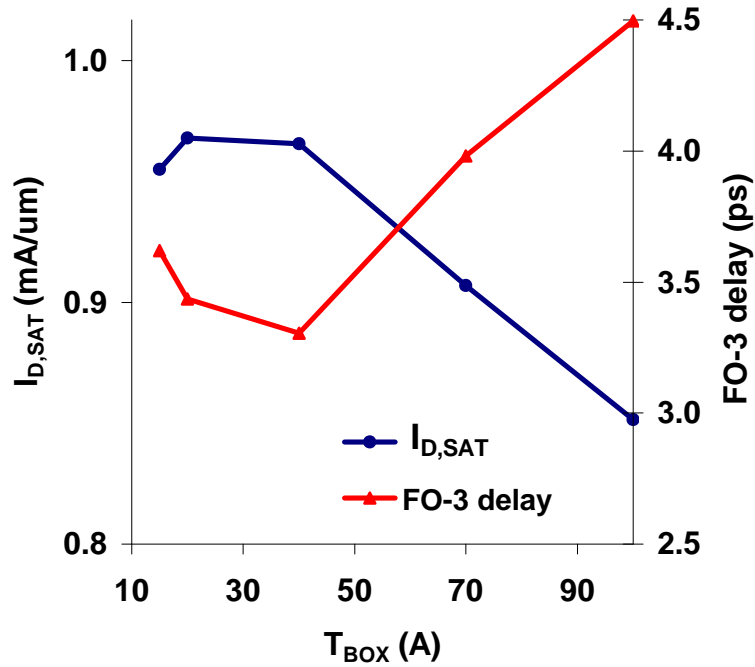


Figure 4.11: Dependence of  $I_{D,SAT}$  and FO-3 delay on  $T_{BOX}$  for  $L_G = 13$  nm. The optimal  $T_{BOX}$  for minimal delay is clearly larger than that for maximum  $I_{D,SAT}$ .

#### 4.8 Effect of Parasitic Capacitances

A disadvantage of thin  $T_{BOX}$  is significant BG and source/drain parasitic capacitances. To assess the impact of this parasitic capacitance on circuit performance, mixed-mode simulations of an inverter FO-3 buffer chain were carried out. It is seen from Figure 4.11 that the optimal  $T_{BOX}$  for minimizing stage delay is  $\sim 40\text{\AA}$ , which is larger than that for maximizing  $I_{D,SAT}$  ( $T_{BOX} \sim 25\text{\AA}$ ). In comparison against the optimized DG-MOSFET, the optimal BG-FDSOI MOSFET design ( $T_{BOX} = 4\text{nm}$ ) has  $\sim 6\%$  lower  $I_{D,SAT}$  and  $\sim 25\%$  higher stage delay. However, the BG-FDSOI structure with relatively thick  $T_{Si}$  should be easier to manufacture (similarly to a bulk-Si MOSFET), making it a worthy candidate to continue scaling CMOS to sub-45nm nodes.



## 4.9 Back-gate Biasing to Limit the Impact of Process Induced Variations

Increasing inter-die and intra-die parameter variation in the nanometer regime can result in a large variability in performance and power. Due to aggravating short channel effects in nanoscale devices, variation in the channel length results in a large variation in threshold voltage (due to  $V_{TH}$ -roll off) and hence subthreshold current. The variations in most transistor parameters such as the device width, oxide thickness or flat-band voltage etc. can all be translated into the variation in threshold voltage.

Adaptive body biasing (ABB) can be used in bulk-Si CMOS integrated circuits to compensate the effects of process-induced variations on  $I_{OFF}$  and  $V_{TH}$  and thereby reduce die-to-die performance variation [19]. Similarly, BG biasing of FDSOI devices with thin  $T_{BOX}$  can be used to compensate the impact of systematic process-induced variations. To allow  $V_{BG}$  to be adjusted for this purpose, the BG-FDSOI MOSFET must be designed to operate with a smaller nominal  $V_{BG}$ . (BG-FDSOI devices optimized for performance use the largest possible reverse  $V_{BG}$ , leaving no room for adaptive BG biasing to counter process-induced variations.) For example, for an n-channel BG-FDSOI device with  $T_{BOX} = 4\text{nm}$ ,  $V_{BG} = -0.8\text{V}$  for optimal delay, but  $V_{BG} = -0.24\text{V}$  to allow for adaptive BG biasing to compensate for systematic  $V_{TH}$  shifts due to process-induced variations.

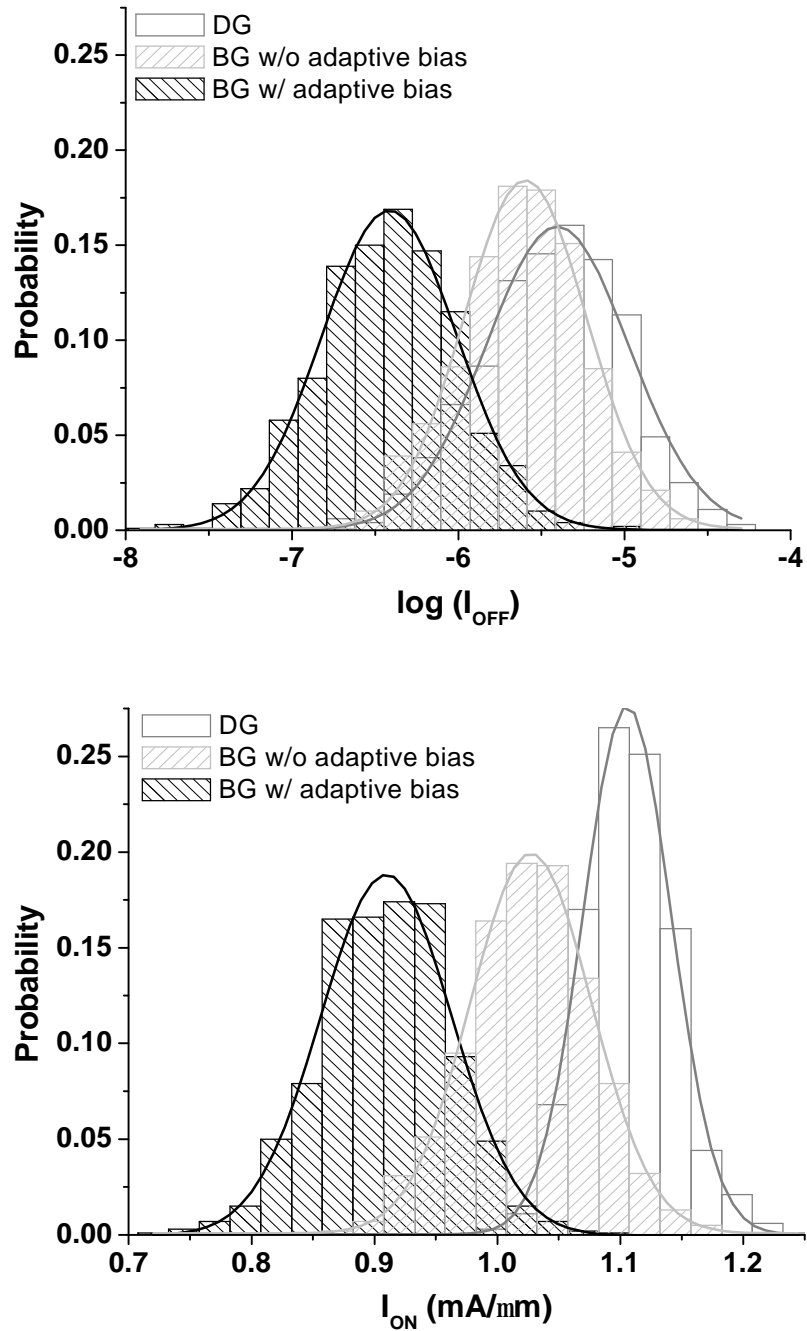


Figure 4.12: Effect of process-induced variations on  $I_{\text{OFF}}$  and  $I_{\text{ON}}$  distributions. These include i) systematic shifts in  $L_G$  (13 nm  $\rightarrow$  12 nm) and  $T_{Si}$  (8 nm  $\rightarrow$  9 nm) ii) random fluctuations in  $L_G$  and  $T_{Si}$  (both with  $3\sigma = 10\%$  of  $L_G$ ). BG-FDSOI MOSFETs have  $I_{\text{OFF}}$  spreads comparable to DG-MOSFETs, but larger  $I_{\text{D,SAT}}$  spreads.

To quantify the benefits of adaptive BG biasing, Monte Carlo simulations were run using 32-nm node device designs that have a combination of systematic shifts in  $L_G$  (13nm ? 12 nm) and  $T_{Si}$  (8 nm ? 9 nm) and random variations with  $3\sigma_{LG}$  and  $3\sigma_{TSi} = 10\%$  of  $L_G$ . From Figure 4.12, it is seen that these variations result in higher average  $I_{OFF}$  and  $I_{D,SAT}$  due to lower average  $V_{TH}$ , for both DG-MOSFETs and BG-FDSOI MOSFETs. For the BG-FDSOI MOSFETs, this can be compensated by adjusting  $V_{BG}$ . With adaptive BG biasing, the BG-FDSOI devices can achieve  $I_{OFF}$  spread comparable to that of DG-MOSFETs, *i.e.*, comparable SCE. Reverse back-gate biasing in BG-FDSOI suppresses SCE in contrast to reverse body biasing (RBB) of bulk-Si MOSFETs which worsens SCE. Thus the application of RBB to offset increased chip leakage arising from systematic die-die variations degrades the intra-die spread in  $V_{TH}$  from random process variations due to degraded SCE. However, reverse back-gate bias does not degrade the  $V_{TH}$  spread in BG-FDSOI MOSFETs as seen in Figure 4.12.

However, the  $I_{D,SAT}$  spread for BG-FDSOI devices is larger, because  $I_{D,SAT}$  is affected by changes not only in  $V_{TH}$  but also in carrier mobility (which depends on  $E_{CH}$ ). For example, with an increase in  $T_{Si}$ ,  $V_{TH}$  reduces and  $E_{CH}$  is lowered, resulting in improved mobility. These factors (lowered  $V_{TH}$  and increased mobility) improve  $I_{D,SAT}$  significantly. With a decrease in  $T_{Si}$ ,  $I_{D,SAT}$  is degraded significantly. For DG-MOSFETs, there is no built-in electric field, *i.e.*,  $E_{CH}$  is not dependent on  $T_{Si}$ , so the degree of variation in  $I_{D,SAT}$  is smaller.

## 4.10 Conclusions

A new scale length model is derived for the back-gated FDSOI MOSFET, accounting for the quantum-corrected location of the effective subthreshold leakage path.

This model captures the effects of front- and back-gate-oxide thicknesses, channel/body thickness, and back-gate bias on the scale length and can be used to describe quantitatively the SCEs in BG-FDSOI devices. The scale length of a BG-FDSOI device can be improved by applying a reverse bias on the back-gate to push the effective leakage path to the front channel surface in order to increase front-gate control. Reverse back-gate biasing can therefore be used to relax the SOI film thickness requirement of BG-FDSOI making them easier to manufacture. The back oxide thickness for optimal performance is around 40Å for 13nm  $L_G$  devices. The on-state current of an optimized BG-FDSOI MOSFET approaches that of a FinFET, with the parasitic back-gate capacitance resulting in a delay penalty of ~25%. The optimal back-gate bias to compensate for variations is smaller than that to maximize performance, and it is seen that BG-FDSOI devices can be tuned to reduce the impact of process-induced variations.

#### **4.11 References**

- [1] D. J. Frank, Y. Taur, and H.-S. P. Wong, "Generalized scale length for two-dimensional effects in MOSFETs," *IEEE Electron Device Letters*, vol. 19, pp. 385-7, 1998.
- [2] K. Suzuki, T. Tanaka, Y. Tosaka, H. Horie, and Y. Arimoto, "Scaling theory for double-gate SOI MOSFET's," *IEEE Transactions on Electron Devices*, vol. 40, pp. 2326-9, 1993.
- [3] T. K. Chiang, "A novel scaling-parameter-dependent subthreshold swing model for double-gate (DG) SOI MOSFETs: including effective conducting path effect (ECPE)," *Semiconductor Science & Technology*, vol. 19, pp. 1386-90, 2004.

- [4] K. Suzuki and T. Sugii, "Analytical models for n+-p+ double-gate SOI MOSFET's," IEEE Transactions on Electron Devices, vol. 42, pp. 1940-8, 1995.
- [5] Q. Chen, B. Agrawal, and J. D. Meindl, "A comprehensive analytical subthreshold swing (S) model for double-gate MOSFETs," IEEE Transactions on Electron Devices, vol. 49, pp. 1086-90, 2002.
- [6] U. Avci, A. Kumar, and S. Tiwari, "Theoretical and experimental analysis of back-gated SOI MOSFETs and Back-Floating NVRAMs," Journal of Semiconductor Technology and Science, vol. 4, pp. 18-26, March 2004.
- [7] G. Bastard, E. E. Mendez, L. L. Chang, and L. Esaki, "Variational calculations on a quantum well in an electric field," Physical Review B (Condensed Matter), vol. 28, pp. 3241-5, 1983.
- [8] Z. H. Liu, C. Hu, J. H. Huang, T. Y. Chan, M. C. Jeng, P. K. Ko, and Y. C. Cheng, "Threshold voltage model for deep-submicrometer MOSFETs," IEEE Transactions on Electron Devices, vol. 40, pp. 86-95, 1993.
- [9] M. Jeong, H. S.-P. Wong, Y. Taur, P. Oldiges, and D. Frank, "DC and AC performance analysis of 25 nm symmetric/asymmetric double-gate, back-gate and bulk CMOS," presented at 2000 International Conference on Simulation of Semiconductor Processes and Devices. Seattle, WA, 2000.
- [10] B. Iniguez, "Comments on "Threshold voltage model for deep-submicrometer MOSFETs"," IEEE Transactions on Electron Devices, vol. 42, pp. 1712, 1995.
- [11] R. Tsuchiya, M. Horiuchi, S. Kimura, M. Yamaoka, T. Kawahara, S. Maegawa, T. Ipposhi, Y. Ohji, and H. Matsuoka, "Silicon on thin BOX: a new paradigm of the

- CMOSFET for low-power high-performance application featuring wide-range back-bias control," IEDM Technical Digest, pp. 631-634, 2004.
- [12] H.-S. P. Wong, D. J. Frank, and P. M. Solomon, "Device design considerations for double-gate, ground-plane, and single-gated ultra-thin SOI MOSFET's at the 25 nm channel length generation," presented at International Electron Devices Meeting 1998. Technical Digest. San Francisco, CA, 1998.
- [13] T. Numata and S. Takagi, "Device design for subthreshold slope and threshold voltage control in sub-100-nm fully depleted SOI MOSFETs," IEEE Transactions on Electron Devices, vol. 51, pp. 2161 - 2167, 2004.
- [14] W. Haensch, E. J. Nowak, R. H. Dennard, P. M. Solomon, A. Bryant, O. H. Dokumaci, A. Kumar, X. Wang, J. B. Johnson, and M. V. Fischetti., "Silicon CMOS devices beyond scaling," IBM Journal of Research and Development, vol. 50, pp. 339-361, 2006.
- [15] L. Mathew, Y. Du, A.-Y. Thean, M. Sadd, A. Vandooren, C. Parker, T. Stephens, R. Mora, R. Rai, M. Zavala, D. Sing, S. Kalpat, J. Hughes, R. Shimer, S. Jallepalli, G. Workman, W. Zhang, J. G. Fossum, B. E. White, B. Y. Nguyen, and J. Mogab, "CMOS Vertical Multiple Independent Gate Field Effect Transistor (MIGFET)," presented at 2004 IEEE International SOI Conference. Charleston, SC, 2004.
- [16] "Taurus-Device, v. 2003.12," Synopsys Inc., 2003.
- [17] "International Technology Roadmap for Semiconductors, 2003 ed," <http://www.itrs.net/Links/2003ITRS/Home2003.htm>.

- [18] A. Raychowdhury, S. Mukhopadhyay, and K. Roy, "Modeling and estimation of leakage in sub-90 nm devices," Proceedings of the 17th International Conference on VLSI Design, pp. 65 - 70, 2004.
- [19] J. W. Tschanz, J. T. Kao, S. G. Narendra, R. Nair, D. A. Antoniadis, A. P. Chandrakasan, and V. De, "Adaptive body bias for reducing impacts of die-to-die and within-die parameter variations on microprocessor frequency and leakage," presented at 2002 IEEE International Solid-State Circuits Conference. Digest of Technical Papers. San Francisco, CA, 2002.

# Chapter 5 : FinFET based SRAM design

## 5.1 Introduction

Increasing process-induced variations and leakage current with  $L_G$  scaling in bulk-Si MOSFETs limit the scalability of SRAM. FinFET-based six transistor (6-T) SRAM cells have been demonstrated to be more stable, with low standby power [1-4]. This chapter discusses various design considerations such as cell stability, immunity to process variations, and cell area for continuing SRAM scaling using FinFET technology [5]. 6-T-SRAM cells for use at the 45nm technology node are designed using FinFETs with a midgap workfunction metal gate material for both NMOS and PMOS devices. Ways to improve the process immunity of SRAMs are discussed. Tradeoffs in stability and area for SRAM cells utilizing different channel surface orientations and FinFETs with multiple fins are studied. To substantially reduce the SRAM cell area four-transistor (4-T) SRAM designs have been proposed, but suffer from large power dissipation problems [6]. In this chapter, FinFET-based 4-T SRAMs cells are proposed with a mix of double-gated and independently gated FinFETs to implement dynamic feedback to achieve low power as well as area savings. It is found that FinFET-based 6-T and 4-T SRAM cell designs with dynamic feedback achieve significant improvements in the static noise margin (SNM) without incurring area penalty. Read versus write margin tradeoffs



for six-transistor (6-T) and four-transistor (4-T) SRAM cells w/dynamic feedback are presented as well.

## 5.2 Challenges in Bulk-Si SRAM Scaling

SRAM is by far the dominant form of embedded memory found in today's integrated circuits, occupying about 60-70% of the total chip area and about 75%-85% of the total transistor count in certain integrated circuits [7]. As memory will continue to consume a large fraction of many future designs, scaling of memory density must continue to track the scaling trends of logic. Challenges for MOSFET scaling in the nanoscale regime, including gate oxide leakage, control of short channel effects, contact resistance, ultra-shallow and abrupt junction technology apply to SRAM scaling as well.

While it is possible to scale the classical bulk-Si MOSFET structure to sub-45 nm nodes [8, 9], effective control of SCE requires heavy channel doping ( $>5 \times 10^{18} \text{ cm}^{-3}$ ) and heavy super-halo implants to suppress sub-surface leakage currents. As a result, carrier mobilities are severely degraded due to impurity scattering and a high transverse electric field in the ON-state. Furthermore, degraded SCE result in large leakage and a larger sub-threshold slope.  $V_{TH}$  variability caused by random dopant fluctuations is another concern for nanoscale bulk-Si MOSFETs and is perceived as a fundamental roadblock for scaling SRAM. In addition to statistical dopant fluctuations, line-edge roughness increases the spread in transistor threshold voltage ( $V_{TH}$ ) and thus the on- and off- currents, and can limit the size of the cache [10, 11].

## 5.3 6-T SRAM DESIGN TRADEOFFS



enough to compensate for the sub-threshold and gate leakage currents of all the NMOS transistors connected to the storage node  $V_L$  (Figure 1). This is becoming more of a concern due to the dramatic increase in gate leakage currents and degradation in  $I_{ON}/I_{OFF}$  ratio in recent technology nodes [12]. While hold stability was not of concern before, there has been a recent trend [13] to decrease the cell supply voltage during standby to reduce static power consumption. The minimum supply voltage or the data retention voltage in standby is dictated by the hold margin. Degraded hold margins at low voltages makes it increasingly more difficult to design robust low-power memory arrays.

Hold stability is commonly quantified by the cell static noise margin (SNM) in standby mode with the voltage on the wordline  $V_{WL}=0$  V. The SNM of an SRAM cell represents the minimum DC-voltage disturbance necessary to upset the cell state [14], and can be quantified by the length of the side of the maximum square that can fit inside the lobes of the butterfly plot formed by the transfer characteristics of the cross-coupled inverters (Figure 5.1b).

### 5.3.3 Read Margin

During a read operation, with the bitlines (BL and BLC) in their precharged state, the WL is turned on (i.e., biased at  $V_{DD}$ ), causing the storage node voltage,  $V_R$ , to rise above 0V, to a voltage determined by the resistive voltage divider formed by the access transistor (AXR) and the pull-down transistor (NR) between BL and ground (Figure 1). The ratio of the strengths of the NR and AXR devices (ratio of width/length of the two devices) determines how high  $V_R$  will rise, and is commonly referred to as the cell  $\beta$ -ratio. If  $V_R$  exceeds the trip voltage of the inverter formed by PL and NL, the cell bit will flip during the read operation, causing a read upset.

Read stability can be quantified by the cell SNM during a read access. Since AXR operates in parallel to PR and raises  $V_R$  above 0V, the gain in the inverter transfer characteristic is decreased [10], causing a reduction in the separation between the butterfly curves and thus in SNM. For this reason, the cell is considered most vulnerable to electrical disturbs during the read access. The read margin can be increased by upsizing the pull-down transistor, which results in an area penalty, and/or increasing the gate length of the access transistor, which increases the WL delay and also hurts the write margin. [15]

Process-induced variations result in a decrease in the SNM, which reduces the stability of the memory cell, and have become a major problem for scaling SRAM. While circuit design techniques can be used to compensate for variability, it has been pointed out that these will be insufficient, and that development of new technologies, including new transistor structures, will be required [16].

### **5.3.4 Write Margin**

The cell is written by applying appropriate voltages to be written to the bit lines, e.g. if a '1' is to be written, the voltage on the BL is set to  $V_{DD}$  while that on the BLC is set to 0V and then the WL is pulsed to  $V_{DD}$  to store the new bit. Careful sizing of the transistors in a SRAM cell is needed to ensure proper write operation. During a write operation, with the voltage on the WL set to  $V_{DD}$ , AXL and PL form a resistive voltage divider between the BLC biased at 0V and  $V_{DD}$  (Figure 1). If the voltage divider pulls  $V_L$  below the trip voltage of the inverter formed by PR and NR, a successful write operation occurs. The write margin can be measured as the maximum BLC voltage that is able to flip the cell state while the BL voltage is kept high. The write margin can be improved by

keeping the pull-up device minimum sized and upsizing the access transistor W/L, at the cost of cell area and the cell read margin.

### **5.3.5 Access Time**

During any read/write access, the WL voltage is raised only for a limited amount of time specified by the cell access time. If either the read or the write operation cannot be successfully carried out before the WL voltage is lowered, access failure occurs. A successful write access occurs when the voltage divider is able to pull voltage at  $V_L$  below the inverter trip voltage, after which the positive feedback in the cross-coupled inverters will cause the cell state to flip almost instantaneously. For the precharged bit-line architecture that employs voltage-sensing amplifiers, a successful read access occurs if the pre-specified voltage difference,  $\Delta V$ , between the bit-lines (required to trigger the sense amplifier) can be developed before the WL voltage is lowered [17].

Access time is dependent on wire delays and the memory array column height. To speed up access time, segmentation of the memory into smaller blocks is commonly employed. With reductions in column height, the overhead area required for sense amplifiers can become substantial, however.

### **5.3.6 Power**

Large embedded SRAM arrays consume a significant portion of the overall power of an application processor. Power consumption in an SRAM array consists of short active periods and very long idle periods. For large arrays, standby power consumption is a major issue. Therefore, leakage reduction in large memory arrays has become essential for low-power VLSI applications. Cell leakage is commonly suppressed by

either using longer channel lengths or higher transistor threshold voltages. Using longer channel lengths increases the cell area and in addition, the use of longer channel lengths tends to increase WL and BL capacitances, thus increasing access time and active power. Therefore, longer channel lengths are used sparingly (for example on the access transistors, which improves cell stability as well).[15]

Utilizing higher transistor threshold voltages also negatively impacts the access time due to the lower read current. However, it improves the read and write margins. While high threshold PMOS loads decrease the inverter trip point, high threshold NMOS pull-down devices (NPD) tend to increase it. Since the current driving ability of the NPD is larger than that of the PMOS load, increasing the threshold voltage of the NMOS transistors tends to have a stronger impact on the trip voltage [3], thus resulting in larger read and write margins. Typically, the maximum standby static power dissipation of the memory array sets the lower limit (e.g. 0.4-0.5V) for the  $V_{TH}$  in a given process. Then the operating margins are maintained by setting the supply voltage,  $V_{DD}$ , sufficiently high. There are circuit techniques to reduce memory leakage as well: using sleep transistors and body biasing [18, 19]. However, these have tradeoffs in density and can compromise cell stability.

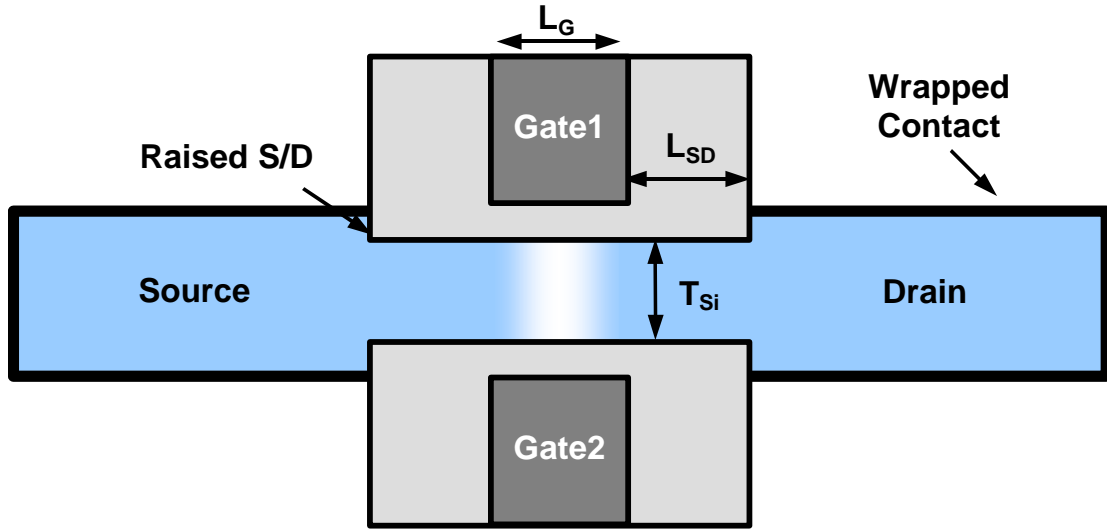
## **5.4 FinFET design for SRAMs**

The FinFET structure is promising for scaling CMOS into the sub-45nm regime, particularly for low-power applications such as memory [20, 21]. Design considerations for maximizing performance and yield of FinFET-based 6-T SRAM at the 45nm generation CMOS technology are examined here. SCE are effectively suppressed by a narrow silicon fin, which allows for gate-length scaling down to the 10-nm regime

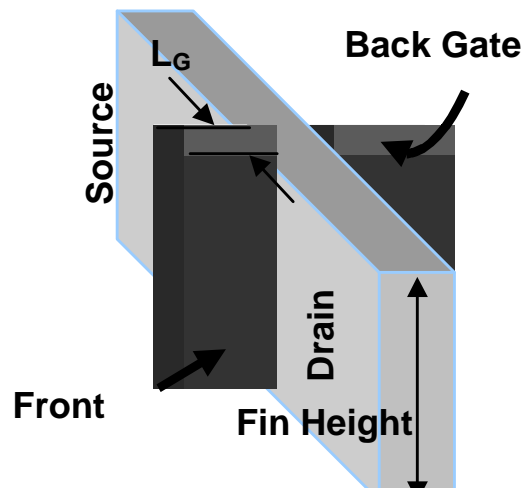
without the use of heavy channel/body doping. A lightly doped channel gives rise to lower transverse electric field in the on state and negligible impurity scattering, hence higher carrier mobilities. It also allows FinFET devices to have negligible depletion charge and capacitance, which yields a steep sub-threshold slope. In addition, FinFETs have lower parasitic device capacitance because both depletion and junction capacitances are effectively eliminated, which reduces the BL capacitive load. Finally, the elimination of heavy doping in the channel minimizes  $V_{TH}$  variations due to statistical dopant fluctuation effects. Therefore, FinFET-based SRAM cells are expected to show enhanced performance over planar bulk-Si MOSFET SRAM cells.

## **5.5 Simulation of FinFET-Based SRAM Cell Designs**

The lack of a compact device model for back-gated operation of a FinFET necessitates the use of mixed-mode device/circuit simulations using Taurus [22] to generate the SRAM butterfly plot in standby and read modes. The transistor structure used in this study is shown in Figure 5.2 with key design parameters summarized in Table 5-1. Drift-diffusion models and 1-D Schrödinger equations were used to determine the device I-V characteristics.



(a)



(b)

Figure 5.2: (a) Cross-sectional schematic of double-gate MOSFET structure used for Taurus-Device simulation structure including raised source/drain regions, and wrapped contacts to capture parasitic effects (b) The gates of the FinFET can be separated for independent back-gate operation.



Parameters	FinFET	Bulk-Si
$L_G$ (nm)	22	22
$L_{SD}$ (nm)	24	24
$T_{ox}$ (Å)	11	11
$T_{Si}$ (nm)	15	-
$V_{DD}$ (V)	1.0	1.0
Channel Doping, $N_{BODY}$ ( $cm^{-3}$ )	$10^{16}$	$4 \times 10^{18}$
$H_{FIN}$ (nm)	30	-
S/D doping gradient (nm/dec)	4	4

Table 5-1: Device parameters used for Taurus simulations

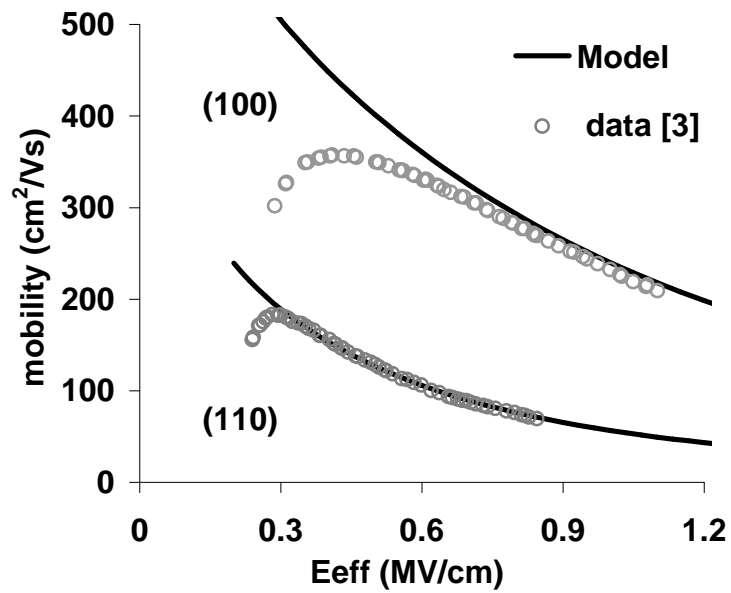


Figure 5.3: Lombardi surface mobility model (used in Taurus simulations) matched to experimental data for n-channel MOSFETs [23, 24]

To capture the effect of the fin-sidewall surface crystalline orientation on FinFET performance, the field-effect mobilities in Taurus are calibrated using experimental data for the (110) surface [23, 24], since FinFET channel surfaces fabricated on a standard (001) wafer are along (110) planes, for standard layout orientations (see Figure 5.3).

Because the high-field transient velocity overshoot effects are ignored, the drain current values may be underestimated in drift-diffusion transport based simulations. However, the qualitative trends and differences between device technologies and their impact on SRAM noise margins should still be valid because they depend on the relative strengths of two transistors and not their absolute  $I_{ON}$ . On the other hand, the error in estimating the  $I_{ON}$  together with unknown interconnect properties make access time simulations unreliable and they were therefore not performed.

It is expected that the effect of parasitic resistances and capacitances will limit circuit performance in deeply scaled CMOS technologies. Series resistance and extrinsic contact resistance are included in this work, which reduces the improvements associated with the intrinsic device structure (Figure 2.1). With the control of short-channel effects in bulk devices becoming increasingly difficult at shorter gate lengths, FinFET devices have increasing performance improvements over bulk-Si MOSFETs with technology scaling.

## **5.6 FinFET based SRAM - Technology Considerations**

### **5.6.1 Gate workfunction ( $F_G$ )**

Devices for high-performance logic need dual gate workfunction ( $F_G$ ) technology [25], which requires two different metals, one with a low workfunction ( $\sim 4.4$  eV) and one with a high workfunction ( $\sim 4.9$  eV), to set the required  $V_{TH}$  for NMOS and PMOS

devices, respectively. Various approaches have been proposed to achieve dual workfunctions [26, 27]. However, the higher- $V_{TH}$  requirement for SRAMs means that the ideal  $F_G$  values for the two metals approach mid-gap. From a layout density perspective, in order to achieve minimal spacing between the NMOS and PMOS devices, dual gate implants needed to adjust the workfunctions are infeasible due to geometric shadowing effects, as shown in Figure 5.4. The gate running over the sidewalls of the fins precludes the possibility of dual implants to set the right  $V_{TH}$ , and so a single midgap metal gate is needed from an ease of integration point of view. In addition, the n+/p+ drains need to be strapped using silicide [28]. A single metal gate with  $F_G = 4.75\text{eV}$  provides with symmetric NMOS/PMOS performance, while  $F_G = 4.6\text{eV}$  requires the use of accumulation mode (acc) PMOS

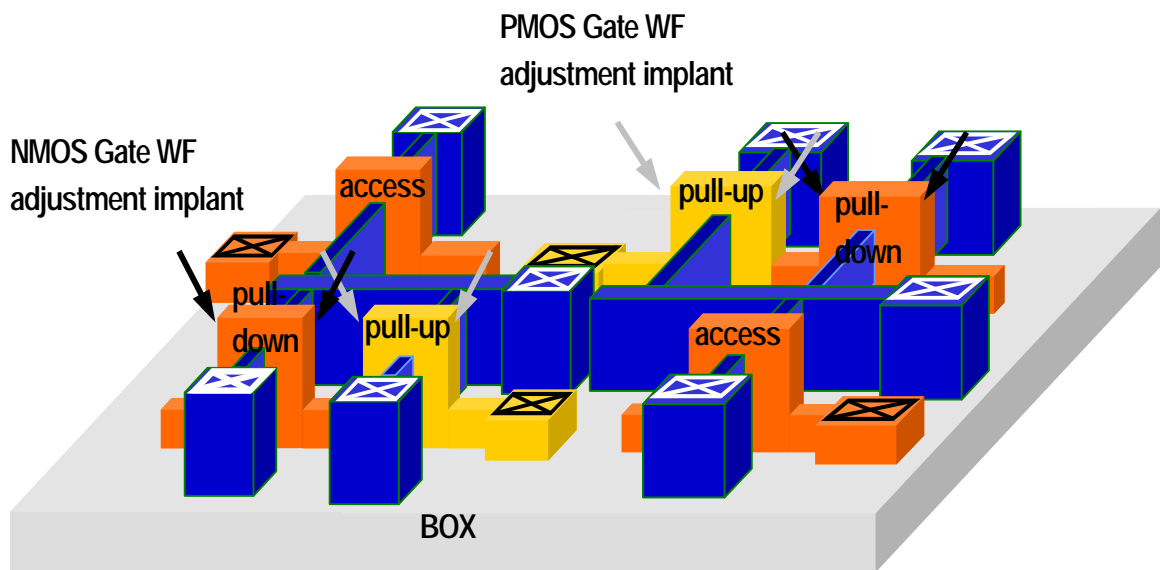


Figure 5.4: 3-D schematic of a FinFET based 6-T SRAM cell. The NMOS and the PMOS devices require separate tilted gate implants to set the correct  $V_{TH}$ , which is not possible to achieve in a dense 6-T SRAM cell due to shadowing effects.

### 5.6.2 Channel doping

Channel doping is a way to set the correct  $V_{TH}$  in FinFET devices. However, since the Si fin thickness is very small, the level of channel doping required to set the correct  $V_{TH}$  is very high. Higher channel doping results in mobility degradation from Coulombic scattering and increased transverse electric field [29] and causes increased random dopant fluctuation effects resulting in the statistical variation of the  $V_{TH}$  [11, 30]. Therefore, the channel is best left undoped, thereby eliminating the impact of dopant fluctuations on  $V_{TH}$ . If the  $F_G = 4.6\text{eV}$  is chosen, the PMOS load device must be doped and is in an accumulation mode device (acc-PMOS). The acc-PMOS has lower performance and shows greater sensitivity to variations (Figure 5.5), and therefore this design was not pursued.

### 5.6.3 Body thickness

In order to control short channel effects, the body thickness needs to be in the  $L_G/2$  to  $0.7L_G$  range [25]. Achieving this with good dimensional control can be challenging. There are novel technologies such as spacer lithography [21, 31], and more conventional approaches such as controlled photoresist ashing and sacrificial oxidation of the single crystalline Si-fin. Variation in fin width is potentially a major source of SRAM variations, if not controlled adequately.

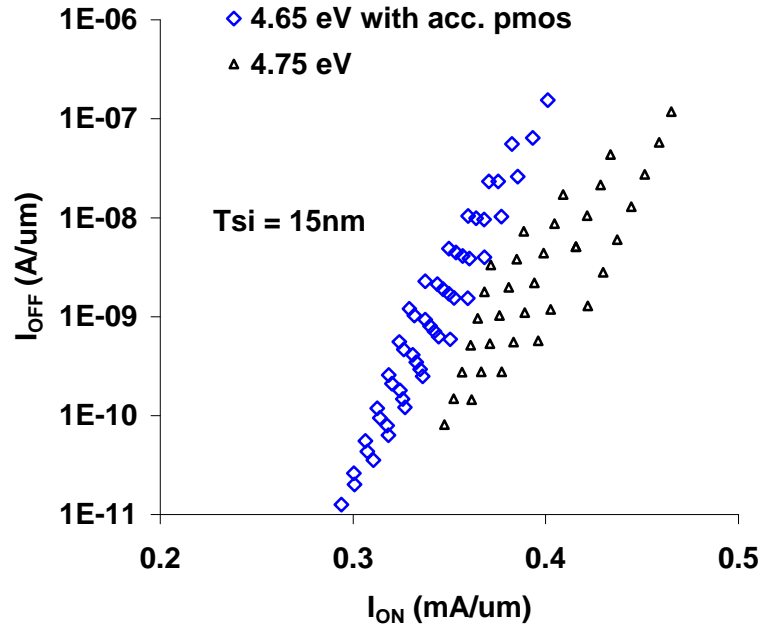


Figure 5.5: Comparison of  $I_{ON} - I_{OFF}$  spreads for enhancement-mode PMOS vs. accumulation mode PMOS devices arising from statistical variations in  $L_G$  and  $T_{Si}$  ( $3\sigma L_G = 3\sigma T_{Si} = 2.1$  nm). The  $V_{TH}$  for the acc-PMOS devices is set by doping the channel. Acc-PMOS shows greater variability and lower performance.

#### 5.6.4 Fin surface orientation

NMOS	(100)	(110)
Thick Si Body	100%	80%
Thin Si Body	100%	81%

Table 5-2: Summary of relative  $I_{D,SAT}$  for various channel orientations. Due to velocity saturation, the impact of mobility differences on  $I_{D,SAT}$  is limited [32].

The FinFET sidewall surfaces fabricated on standard orientation (001) wafers lies along (110) planes, and along (100) planes if the layouts are rotated by 45°. For a (110) surface, hole mobility is enhanced while electron mobility is degraded as compared to a (100) surface [29]. Due to velocity saturation effects in nanoscale devices, only a small fraction of the mobility change results in a change in  $I_{D,SAT}$  (Table 5-2).

### **5.6.5 Sensitivity of FinFET performance to process-induced variations**

Control of critical dimensions does not track their scaling, thus the ratio of the standard deviation ( $\sigma$ ), over the average ( $\mu$ ) increases. Designing large arrays requires design for 5 or more standard deviations ( $> 5\sigma$ ). With increasing variations, it becomes difficult to guarantee near-minimum-sized cell stability for large arrays for embedded, low-power applications. Increasing transistor sizes, on the other hand, is counter to the fundamental reason for scaling in the first place – to increase storage density.

The process-induced variation in FinFET performance arises from statistical variations in  $L_G$  and  $T_{Si}$ . The devices with different  $T_{Si}$  are optimized individually, as discussed in Chapter 2, by changing the  $L_{EFF}$  by adjusting the gate sidewall spacer thickness and tuning  $F_G$  to meet the  $I_{OFF}$  target and  $DIBL = 100mV/V$ . A thinner  $T_{Si}$  yields better leakage and control of short channel effects (SCE) so that a lower  $F_G$  and  $L_{EFF}$  can be used, leading to larger  $I_{ON}$ . The simulations to study the impact of process variations assume that the same patterning technology is used to define the fins and the gates and therefore have the same absolute variability, with a  $3\sigma = 10\%$  of  $L_G$ . This large variation in  $T_{Si}$  results in a large spread in  $I_{ON}$ - $I_{OFF}$ .

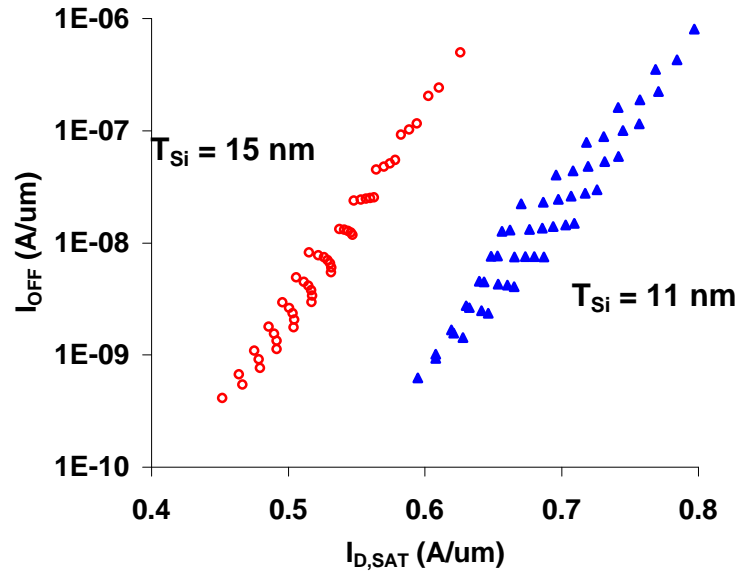


Figure 5.6: Spread in NMOS  $I_{ON}$  versus  $I_{OFF}$  with  $L_G$  and  $T_{Si}$  variations ( $3\sigma_{L_G} = 3\sigma_{T_{Si}} = 2.1\text{nm}$ ) from Taurus-Device simulations. The devices with different  $T_{Si}$  are optimized individually by changing the  $L_{EFF}$  to meet the  $I_{OFF}$  target and  $DIBL = 100\text{mV/V}$ . A thinner  $T_{Si}$  yields better  $I_{OFF}$  and SCE and so a lower  $F_G$  can be used, leading to larger  $I_{ON}$ .

If spacer lithography is used to pattern the fins, the degree of variations in  $T_{Si}$  can be reduced because the spacer thickness can be well controlled through the CVD deposition of the sidewall material [21, 31]. The spread in  $I_{ON}$ - $I_{OFF}$  is comparable for the thinner and the thicker silicon body thickness, due to a tradeoff between better control of short channel effects using thinner  $T_{Si}$  versus a larger relative variation in  $T_{Si}$  for the thinner body case (Figure 5.6).

## 5.7 FinFET SRAM Cell Designs

### 5.7.1 Conventional Double-Gated (DG) Designs

Conventional 6-T SRAMs based on FinFETs have been demonstrated recently to show good stability and low leakage [1-4]. In this section, the various tradeoffs involved in SRAM design are presented. Also, memory density, an important consideration in the choice of SRAM configurations, for the various designs are compared.

Table 5-3 lists the 45nm design rules used in the layouts, generated using a linearly scaled version of 90nm node logic design rules. If a borderless contact technology is available for FinFETs, then memory density can be significantly improved, as the layout is no longer limited by active and contact layer rules, but by metal layer rules instead.

Design Rules	Line/ Space (nm)
Active	50 / 70
Poly	50/70
Contact	60/70
Metal1	60/60
Via1	65/75
M-x	70/70
Via-x	65/75
Poly-related active	50
Poly-unrelated active	25
Poly-contact	40

Table 5-3: 45nm-node design rules used to study the layout implications of the various SRAM designs.



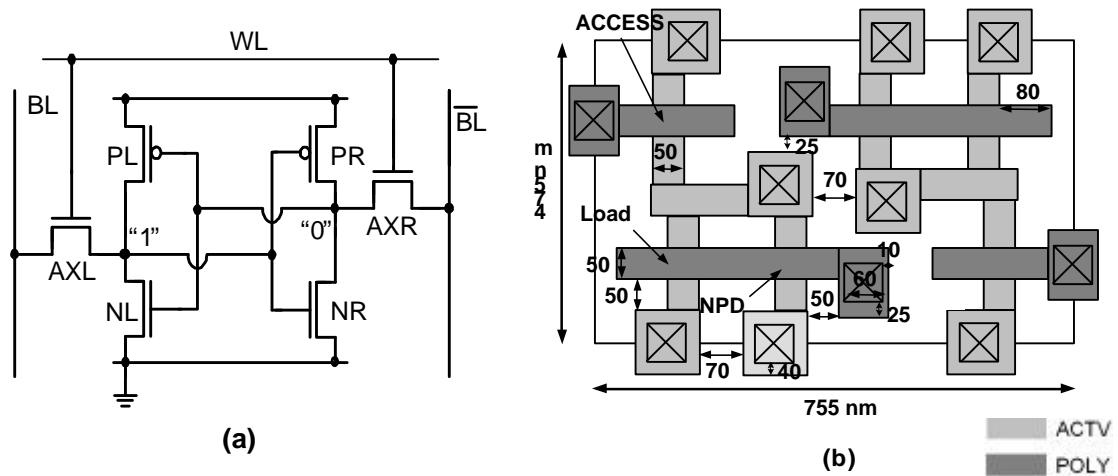


Figure 5.7. Circuit schematic (a) and layout (b) for a conventional DG 6-T SRAM cell.

The outline indicates the area of one memory cell.

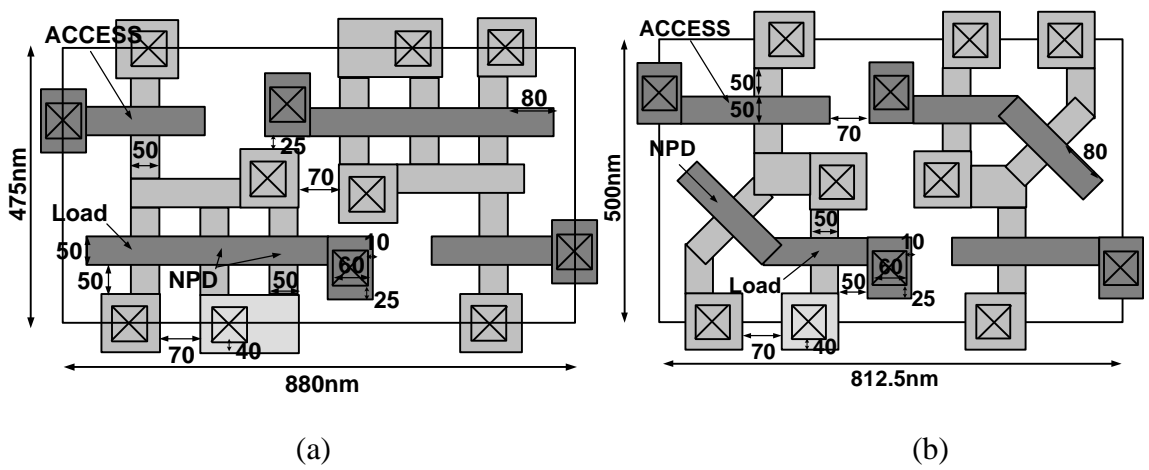


Figure 5.8. 6-T SRAM cell layout with a) 2-fin pull-down FETs b) pull-down devices with rotated fins. The cell  $\beta$ -ratio is improved by increasing the strength of the pull-down NMOS devices, which can be achieved by a) having 2 fins in the pull-down NMOS devices to double their effective channel width, or b) rotating the fin orientation by  $45^\circ$  in order to orient the pull-down NMOS channel surfaces along the (100) planes, thereby increasing electron mobility.

Also, in order to ease lithography, the designs use the long-cell layout, with all the fins running in one direction and all the poly-lines in the perpendicular direction. Source-drain flare-outs can cause variations due to corner rounding effects from lithography, but they make it easier to make conventional top contacts to the source/drain regions. In this study, flared out source/drain regions are used in the layouts.

The read margin of a 6-T SRAM cell can be improved by increasing the strength of the pull-down transistor relative to the access transistor. This is achieved by either by increasing the size-ratio between NR and AXR (ref. Figure 5.1) or enhancing carrier mobility in the pull-down devices relative to the access devices. Significant improvements in read margin can be obtained by upsizing the pull-down transistor (Figure 5.8 a) or increasing  $L_G$  of AXR. Since the effective channel widths of FinFET devices are determined by the number of fins, only discrete sizing is available [1]. Increasing the cell  $\beta$ -ratio by using two fins to the pull-down device is beneficial, and boosts the noise margin by 37% (Figure 5.8 a), but this comes with an area penalty. Increasing the access device  $L_G$  has less impact on cell area but increases the WL capacitance and also negatively impacts the read current, resulting in slower access time.

Electron mobility along (100) planes is higher than along (110) planes. In order to increase the effective cell  $\beta$ -ratio and thus improve the cell read margin, the NMOS pull-down devices (NPD) can be rotated to have channel surfaces along (100) planes. Unlike cell designs in planar bulk-Si CMOS, FinFET-based SRAM cells containing transistors with channel surface both along (110) and (100) planes can be easily fabricated by simply rotating the fin layout orientation by  $45^\circ$  for the (100) fins (Figure 5.8 b). As a tradeoff, printing rotated fins may be lithographically more challenging due

to corner rounding effects and the need for complex OPC to be applied and may in turn lead to enhanced process variations. The mobility difference between the pull-down and the access device causes an  $I_{D,SAT}$  change of about 20% (Table 5-2) and helps to boost noise margins .

Figure 5.9 a-c show the butterfly plots for 6-T bulk-Si MOSFET-based SRAM cells and the 6-T FinFET-based SRAM cells (simulated using device parameters from Table 5-1). As can be seen from these Figures, the conventional DG 6-T FinFET-based SRAM with 1-fin pull-down achieves a 22% improvement in the read SNM compared to its bulk-Si-based counterpart with  $\beta$ -ratio of 1.5. Moreover, a 15% further improvement in the read SNM, with a 13.3% area penalty, can be achieved by rotating the pull-down transistors; a 36% further improvement in the read SNM, with 16.6% area penalty, can be achieved by upsizing the pull-down transistors to 2-fins. Higher threshold pull-down devices were then used in the FinFET designs, by raising the gate work function of the NMOS and PMOS devices (both to 4.75eV), to suppress leakage and to improve read/write margin. The resulting improvements in SNM are shown in Figure 5.9 c. A higher  $V_{TH}$  bulk-Si device achieved by higher channel doping might not provide lower overall standby current due to band-to-band tunneling leakage.

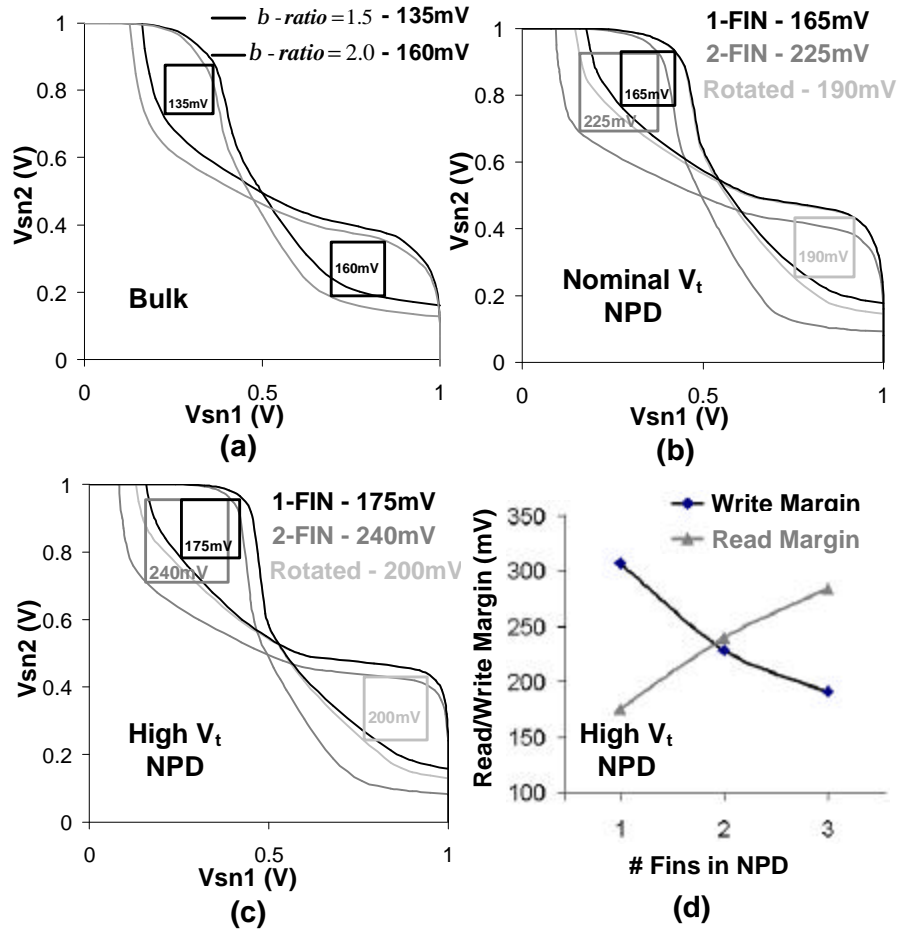


Figure 5.9: 6-T SRAM read butterfly plots (a) bulk-Si MOSFET SRAM cell with  $\beta$ -ratio = 1.5 (black), 2.0 (gray) and (b-c) FinFET-based SRAM cell with 1-fin (black), 2-fins (dark gray), and pull-down device layout rotation (light gray). (d) Impact of adding fins to the NPD on the read- and write-margins.

Whenever the pull-down devices are strengthened, either by adding fins or by rotating the channel surface plane, the cell write margin shrinks – primarily due to the reduction in the write trip voltage. The more stable the cell is during read against voltage disturbs, the harder it becomes to write into the cell. The effects of inserting extra fins on the read and write noise margins are summarized in Figure 5.9 d.

### 5.7.2 FinFET-based 6-T SRAMs w/dynamic feedback

Whereas adaptive body biasing becomes less effective with bulk-Si MOSFET scaling [33, 34], back-gate biasing of a thin-body MOSFET remains effective for dynamic control of  $V_{TH}$  with transistor scaling, and can provide improved control of short-channel effects as well [35]. A FinFET can be operated as a back-gated (BG) thin-body MOSFET if the gate electrode is etched away in the region over the top of the fin, to allow for independent biasing of the gate electrodes on either side of the fin [36, 37]. The strong back-gate biasing effect can be leveraged to optimize the performance of FinFET-based SRAMs.

By connecting each storage node to the back-gate of the access transistor, as shown in Figure 5.10, the strength of the access transistors can be selectively and dynamically decreased. For example, if the stored bit is a “0”, the back-gate of the corresponding access transistor is biased at 0V, thereby decreasing its strength. This effectively increases the  $\beta$ -ratio during the read cycle and thus improves the read margin. Although a BG access transistor has weaker current driving strength compared to a DG access transistor, the “0” storage node in the 6-T design with feedback stays closer to  $V_{SS}$  than the conventional DG design (Figure 5.10 a); thus giving the BG access transistors in the 6-T design more gate overdrive. Therefore, only a small performance hit in terms of read current is incurred by introducing the feedback. A 71% read margin improvement over the DG design is achieved (Figure 5.11a).

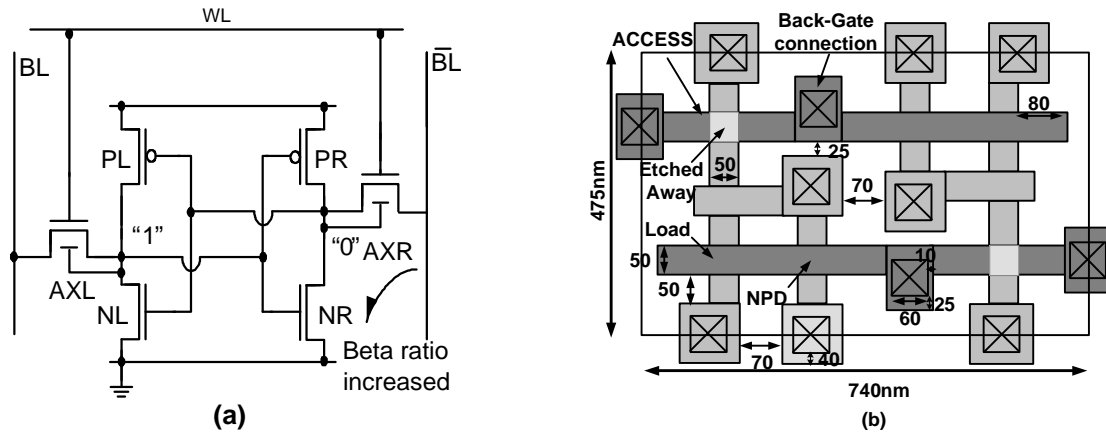


Figure 5.10. Circuit schematic (a) and layout (b) for a 6-T SRAM cell with back-gate connections to provide dynamic feedback. Note the use of BG-FinFET NMOS access devices involves gate separation as indicated in the layout by a dark layer over their gate electrode and fin.

Moreover, this simple back-gate connection can be made by extending the access poly-gate line to connect to the internal storage node, incurring no area penalty over the conventional DG 6-T SRAM cell design (Figure 5.7b vs. Figure 5.10b). Processing techniques such as selective gate separation can be used to make the access device an independently-gated FinFET to enable dynamic feedback. The cell area is actually reduced by 2% due to the disappearance of the gate extension over active (fin) design rule (Table 5-3) that the DG access device required (Figure 5.7b).

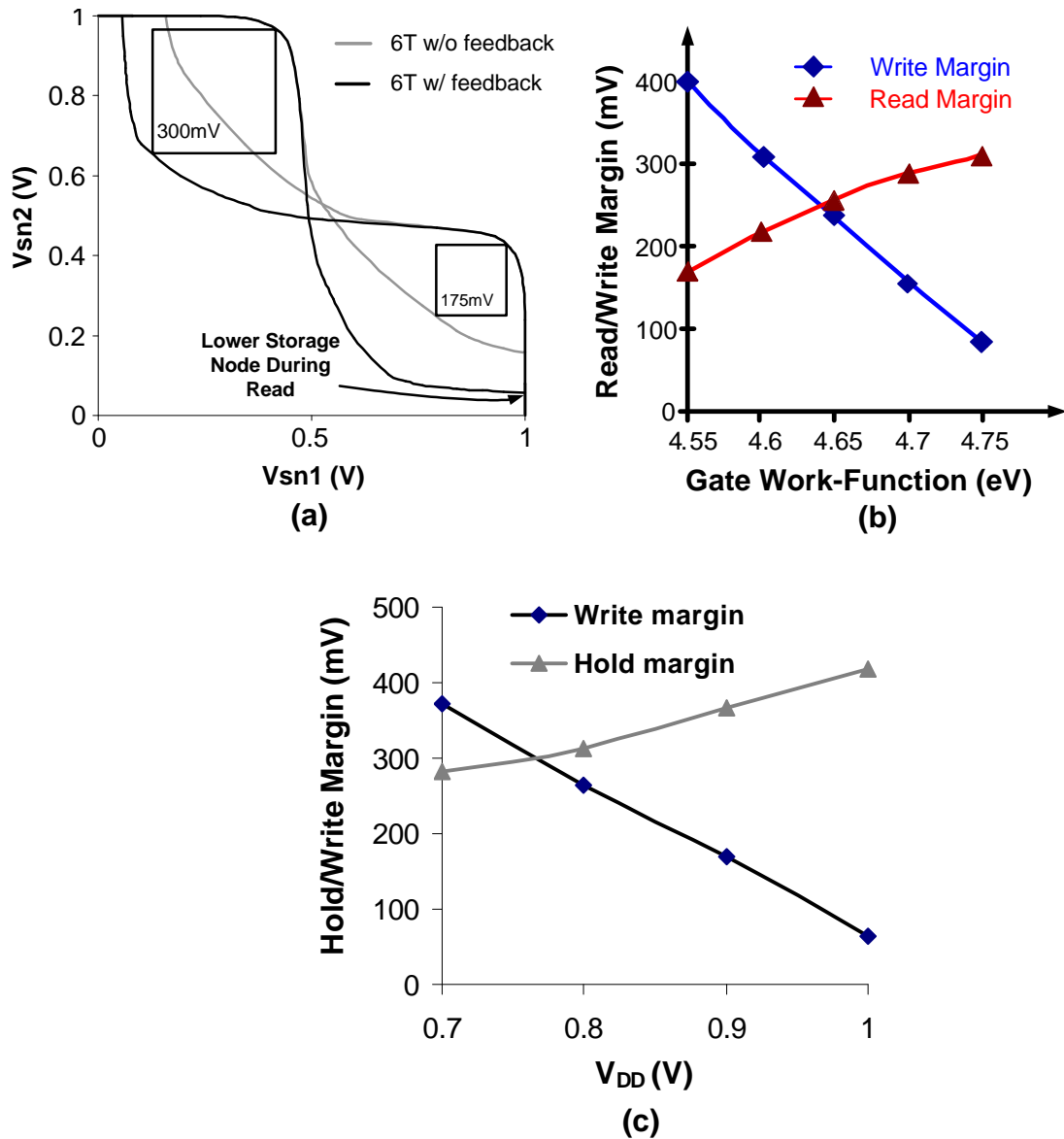


Figure 5.11. (a) Read SNM plot for a FinFET 6-T cell with feedback,  $\Phi_M = 4.75\text{eV}$  (b) Read versus write margin tradeoffs with varying gate workfunction. A gate workfunction of 4.65 eV shows balanced read and write margins c) Impact of cell supply voltage on write margin and standby SNM using  $\Phi_M = 4.75\text{eV}$ . Approximately 300mV of write margin and standby SNM can be achieved with a cell supply voltage of 0.8V.

The main drawback of the 6-T SRAM design with feedback is the reduced write margin because of the reduction in the driving current of the BG access transistor at the

'1' storage node as it is pulled low. This can be combated, without major impact on read SNM, by changing the gate workfunction to adjust the strength of the PMOS load devices (Figure 5.11b). The PMOS load devices can be made weaker by either increasing their threshold voltage or gate length. However, both techniques will only improve the write margin at the expense of the read margin. A much more significant improvement in the write margin can be attained by lowering the cell supply voltage during write [7]. This is made possible by adopting the long AR cell layout, since the cell supply can be routed vertically for each column and can be exploited to break the contention between read and write optimization. With the ability for column based biasing, cell supply voltage can be selectively lowered only for the column containing the cell under write access. This keeps the cell stability high for all other cells connected to the same WL. Thus, large read- and write-margins can be independently achieved. Essentially, the contention between read- and write-margins has been replaced by a contention between hold- and write-margins, which offers a much bigger window for optimization. Figure 5.11c summarizes the enhancement in write margin due to reduced cell supply and the corresponding impact on the hold SNM.

### **5.7.3 4-T FinFET SRAM Cell Design with Dynamic Feedback**

4-T SRAM designs were investigated because they can increase memory density over 6-T SRAM designs. 4-T SRAMs have not been used in embedded applications, because they need a complex process to form a resistive load element and have poor stability at low voltage. A novel 4-T cell design consists of two NMOS devices for pull-down and two PMOS devices as access transistors, and no load devices [6]. During standby, the bit lines and the WL are precharged to  $V_{DD}$ , and in order to retain stored '1'



bit, the PMOS access transistors, which are turned off, need to be very leaky to compensate for the leakage currents in the pull-down transistors during standby, resulting in large-power dissipation. Although compensation current is only needed for the “1” storage node, both PMOS access transistors draw currents from the bit-lines, resulting in high power dissipation.

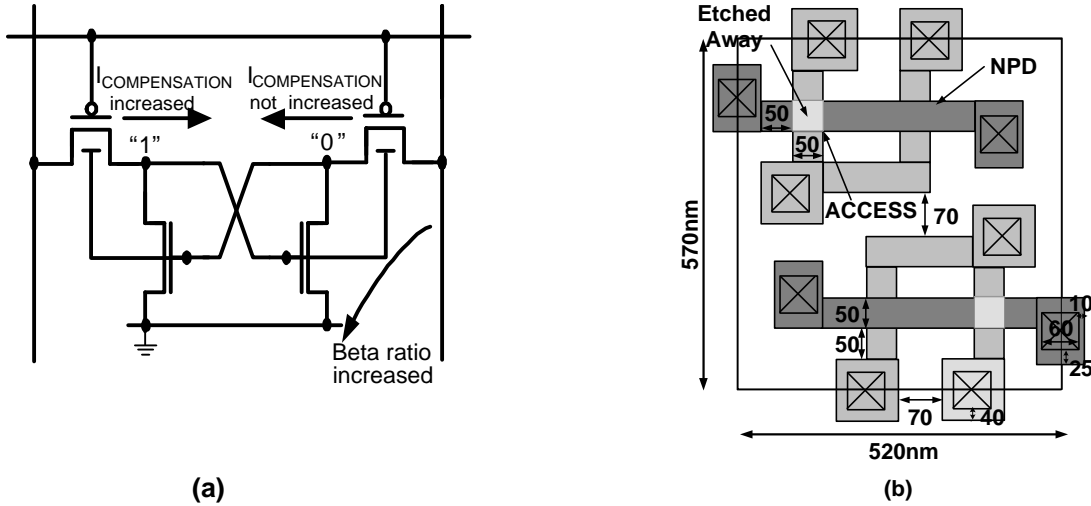


Figure 5.12: Circuit schematic (a) and layout (b) for a 4-T SRAM cell with back-gate connections to provide dynamic feedback. Note the use of BG-FinFET PMOS access devices, indicated in the layout by a dark layer over their gate electrodes and fins.

A newer 4-T SRAM cell design [38] using dynamic control of the PMOS  $V_{TH}$  offers a means for selectively adjusting the compensation leakage current [[38] and also provides higher effective  $\beta$ -ratio for the 4-T SRAM cell design. By cross-coupling the storage node to the back-gate of the access transistor on the opposite side, as shown in Figure 5.12, high compensation current can be selectively injected only into the “1” storage node though the forward biased PMOS device as seen in Figure 5.13. In addition, the  $\beta$ -ratio of the cell is increased because the access transistor connected to the “0”

storage node is made weaker with its back-gate biased by the “1” storage node. (Note that a “1” back-gate bias lowers the PMOS drive current.)

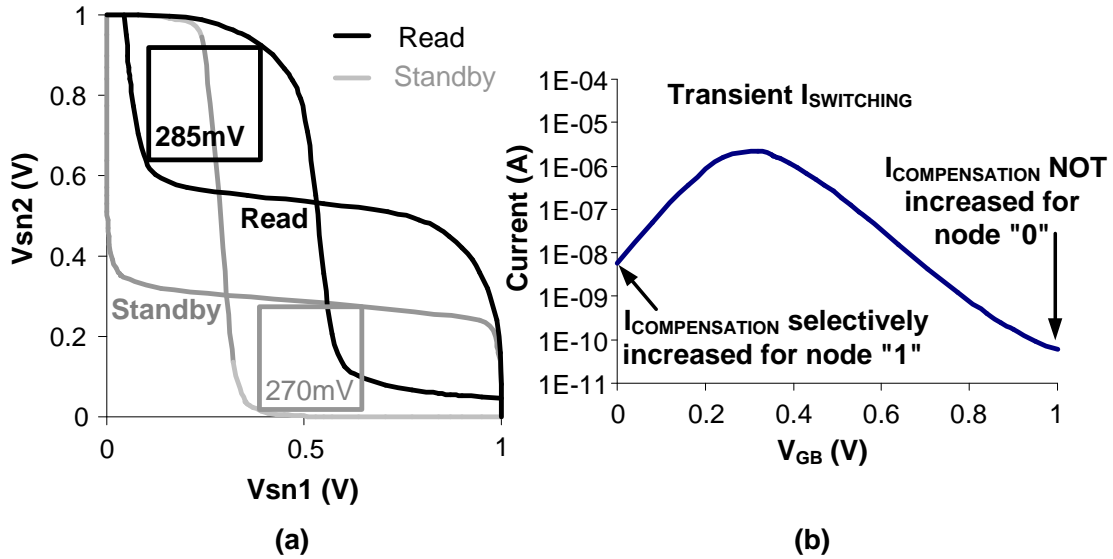


Figure 5.13: (a) SNM plots for a 4-T cell with feedback during standby and read. (b)

Using dynamic feedback,  $I_{COMPENSATION}$  is selectively increased for the “1” node.

Cell Design	$F_G$ (eV)	Cell Area ( $mm^2$ )	SNM (mV)	$I_{CELL, STANDBY}$ (nA)
6-T DG w/ 1-fin NPD	4.75	0.36	175	0.191
6-T DG w/ 2-fin NPD	4.75	0.42	240	0.26
6-T DG w/ rotated NPD	4.75	0.41	200	0.191
6-T w/ feedback	4.65	0.35	300	0.193
4-T w/ feedback	4.65	0.30	285	5.9

Table 5-4: Summary of Bulk and FinFET SRAM characteristics with  $V_{DD} = 1V$

The simulated SNM values, cell area and standby currents for the 4-T and the different 6-T FinFET-based designs are summarized in Table 5-4 and highlight the benefit of dynamic feedback for achieving large SNM without area or leakage penalty. 4-

T cells have good SNM, but tend to be leakier unless leakage suppression techniques such as sleep transistors are used [5].

#### 5.7.4 Effect of Process-Induced Variations

The control of process variables does not track the scaling of minimum features, so that design margins will eventually need to be relaxed to achieve large functional memory arrays. This is seen to be the biggest limiter to SRAM scaling. Process-induced variations in device parameters cause  $V_{TH}$  variations resulting in spread in SNM distributions. The impact of process induced variations on 6-T and 4-T FinFET-based SRAM cells were analyzed using mixed-mode Monte-Carlo simulations in the Taurus-Device simulator [22] assuming completely random and independent fluctuations in  $L_G$  and  $T_{Si}$  ( $3\sigma_{L_G} = 3\sigma_{T_{Si}} = 10\% L_G$ ). For planar bulk MOSFETs, the impact of random dopant fluctuations alone was studied, because they are expected to cause large spreads in device characteristics at sub-20 nm  $L_G$  [11]. The overall variations in planar bulk MOSFET performance will be higher if the gate length variations are included, but these were ignored in this comparison. While systematic fluctuations dominate variations now, random fluctuations are expected to become significant for sub-45nm technology nodes [39, 40]. The impact of statistical variations in device parameters in FinFETs and planar bulk devices on the cell read margin is illustrated in Figure 5.14. It is clear that dynamic feedback improves the SNM significantly, with comparable spread. The nominal SNM for planar bulk-Si SRAMs is smaller and dopant induced fluctuations alone cause larger SNM spreads than in FinFET-based SRAM designs. If variations in  $L_G$  were to be included, this is expected to be even worse. This indicates that dynamic feedback is promising way for building large functional SRAM arrays.

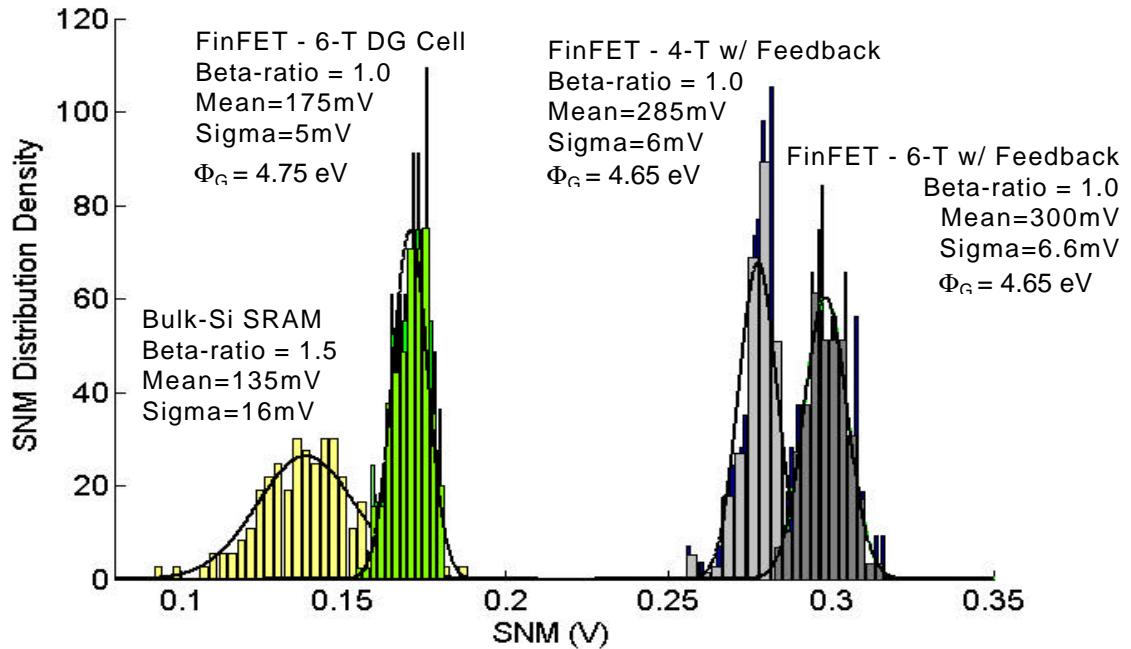


Figure 5.14: Impact of process variations on SNM of SRAM cells at  $V_{DD} = 1V$ . The Monte-Carlo simulations were run using Taurus-Device mixed-mode simulations. FinFET SRAMs have random geometric variations in  $L_G$  and  $T_{Si}$ , whereas bulk-Si SRAMS only have random-dopant fluctuations.

## 5.8 Conclusions

Scaling of planar bulk-Si SRAM cells in recent years has resulted in increased leakage current during standby and performance variations, making it increasingly difficult to achieve both high-speed and low power large functional arrays. FinFET-based SRAM using dynamic feedback is a promising alternative to achieve low leakage and improved SRAM stability.

Conventional FinFET SRAM cells can be made more stable by using more fins in the pull-down devices and/or rotating the pull-down devices to increase the cell  $\beta$ -ratio. 6-T cells with dynamic feedback provide with up to 70% improvement in SNM without

any area, leakage or performance penalty, making them attractive for enabling megabit SRAM. 4-T planar bulk-Si SRAM cells cannot be designed for low power applications, whereas a FinFET-based 4-T SRAM cell with built-in feedback can achieve more than 17% area reduction with 285mV SNM during read and 230mV SNM during standby, making it extremely attractive for high-density, low-power cache memory applications.

The control of process variables does not track the scaling of minimum features, so that design margins would need to be relaxed to achieve large functional memory arrays. This is seen to be the biggest limiter to SRAM scaling. FinFET-based SRAMs do not suffer from intrinsic dopant fluctuations and have higher SNM values and tighter spread than bulk SRAM designs, making FinFET based designs attractive for large arrays. From Figure 5.14, the SNM of the FinFET-based SRAM cells is higher as compared to SRAM cells designed in planar bulk-Si MOSFETs. Conventional FinFET-based 6-T DG designs with high  $V_{TH}$  provide a read SNM of 175mV – a 30% improvement over that of the bulk-Si MOSFET SRAM cell ( $\beta$ -ratio of 1.5). The cell SNM can be further improved by 71% by utilizing built-in feedback to dynamically adjust transistor strengths to improve the cell  $\beta$  ratio. Dynamic feedback helps achieve 300mV SNM in 6-T cells without any area penalty and little performance degradation, while keeping standby leakage current below 0.2nA/cell.

## 5.9 References:

- [1] E. J. Nowak, B. A. Rainey, D. M. Fried, J. Kedzierski, M. Jeong, W. Leipold, J. Wright, and M. Breitwisch, "A functional FinFET-DGCMOS SRAM cell," presented at IEEE International Electron Devices Meeting. San Francisco, CA, 2002.

- [2] T. Park, H. J. Cho, J. D. Choe, S. Y. Han, S. M. Jung, J. H. Jeong, B. Y. Nam, O. I. Kwon, J. N. Han, H. S. Kang, M. C. Chae, G. S. Yeo, S. W. Lee, D. Y. Lee, D. Park, K. Kim, E. Yoon, and J. H. Lee, "Static noise margin of the full DG-CMOS SRAM cell using bulk FinFETs (Omega MOSFETs)," presented at IEEE International Electron Devices Meeting 2003. Washington, DC, 2003.
- [3] R. V. Joshi, R. Q. Williams, E. Nowak, K. Kim, J. Beintner, T. Ludwig, I. Aller, and C. Chuang, "FinFET SRAM for high-performance low-power applications," presented at Proceedings of the 34th European Solid-State Device Research Conference. Leuven, Belgium. 21-23 Sept. 2004, 2004.
- [4] P. Tai-Su, C. Hye Jin, C. Jeong Dong, H. Sang Yeon, P. Donggun, K. Kinam, E. Yoon, and L. Jong-Ho, "Characteristics of the full CMOS SRAM cell using body-tied TG MOSFETs (bulk FinFETs)," *IEEE Transactions on Electron Devices*, vol. 53, pp. 481-7, 2006.
- [5] Z. Guo, S. Balasubramanian, R. Zlatanovici, T.-J. King, and B. Nikolic, "FinFET-based SRAM design," presented at ISLPED '05. Proceedings of the 2005 International Symposium on Low Power Electronics and Design. San Diego, CA, 2005.
- [6] K. Noda, K. Matsui, K. Imai, K. Inoue, K. Tokashiki, H. Kawamoto, K. Yoshida, K. Takeda, N. Nakamura, T. Kimura, H. Toyoshima, Y. Koishikawa, S. Maruyama, T. Saitoh, and T. Tanigawa, "A  $1.9\text{-}\mu\text{m}^2$  loadless CMOS four-transistor SRAM cell in a  $0.18\text{-}\mu\text{m}$  logic technology," presented at International Electron Devices Meeting 1998. Technical Digest. San Francisco, CA, 1998.

- [7] K. Zhang, U. Bhattacharya, Z. Chen, F. Hamzaoglu, D. Murray, N. Vallepalli, Y. Wang, B. Zheng, and M. Bohr, "A 3-GHz 70MB SRAM in 65nm CMOS technology with integrated column-based dynamic power supply," presented at 2005 IEEE International Solid-State Circuits Conference. San Francisco, CA, 2005.
- [8] H. Wakabayashi, S. Yamagami, N. Ikezawa, A. Ogura, M. Narihiro, K. Arai, Y. Ochiai, K. Takeuchi, T. Yamamoto, and T. Mogami, "Sub-10-nm planar-bulk-CMOS devices using lateral junction control," presented at IEEE International Electron Devices Meeting 2003. Washington, DC, 2003.
- [9] A. Hokazono, K. Ohuchi, M. Takayanagi, Y. Watanabe, S. Magoshi, Y. Kato, T. Shimizu, S. Mori, H. Oguma, T. Sasaki, H. Yoshimura, K. Miyano, N. Yasutake, H. Suto, K. Adachi, H. Fukui, T. Watanabe, N. Tamaoki, Y. Toyoshima, and H. Ishiuchi, "14 nm gate length CMOSFETs utilizing low thermal budget process with poly-SiGe and Ni salicide," presented at IEEE International Electron Devices Meeting. San Francisco, CA, 2002.
- [10] A. J. Bhavnagarwala, T. Xinghai, and J. D. Meindl, "The impact of intrinsic device fluctuations on CMOS SRAM cell stability," *IEEE Journal of Solid-State Circuits*, vol. 36, pp. 658-65, 2001.
- [11] A. Asenov, G. Slavcheva, A. R. Brown, J. H. Davies, and S. Saini, "Increase in the random dopant induced threshold fluctuations and lowering in sub-100 nm MOSFETs due to quantum effects: a 3-D density-gradient simulation study," *IEEE Transactions on Electron Devices*, vol. 48, pp. 722-9, 2001.
- [12] H. Pilo, "SRAM Design in the Nanoscale Era," presented at International Solid-State Circuits Conference, 2005.

- [13] H. Qin, Y. Cao, D. Markovic, A. Vladimirescu, and J. Rabaey, "SRAM leakage suppression by minimizing standby supply voltage," presented at Proceedings. 5th International Symposium on Quality Electronic Design. San Jose, CA, 2004.
- [14] E. Seevinck, F. J. List, and J. Lohstroh, "Static-noise margin analysis of MOS SRAM cells," *IEEE Journal of Solid-State Circuits*, vol. SC-22, pp. 748-54, 1987.
- [15] J. M. Rabaey, A. Chandrakasan, and B. Nikolic', *Digital Integrated Circuits*, 2 ed: Prentice Hall, 2002.
- [16] M. Yamaoka, R. Tsuchiya, and T. Kawahara, "SRAM Circuit with Expanded Operating Margin and Reduced Stand-by Leakage Current Using Thin-BOX FD-SOI Transistors," presented at IEEE Asian Solid-State Circuits Conference, Hsinchu, Taiwan, 2005.
- [17] S. Mukhopadhyay, H. Mahmoodi-Meimand, and K. Roy, "Modeling and estimation of failure probability due to parameter variations in nano-scale SRAMs for yield enhancement," presented at 2004 Symposium on VLSI Circuits. Digest of Technical Papers. Honolulu, HI, 2004.
- [18] J. Chang, M. Huang, J. Shoemaker, J. Benoit, S.-L. Chen, W. Chen, S. Chiu, R. Ganesan, G. Leong, V. Lukka, S. Rusu, and D. Srivastava, "The 65nm 16MB On-die L3 Cache for a Dual Core Multi-Threaded Xeon® Processor," presented at 2006 Symposium on VLSI Circuits, Digest of Technical Papers, 2006.
- [19] R. Islam, A. Brand, and D. Lippincott, "Low power SRAM techniques for handheld products," presented at ISLPED '05. Proceedings of the 2005 International Symposium on Low Power Electronics and Design. San Diego, CA, 2005.



- [20] N. Lindert, Y. K. Choi, L. Chang, E. Anderson, W. C. Lee, T. J. King, J. Bokor, and C. Hu, "Quasi-planar FinFETs with selectively grown germanium raised source/drain," presented at 2001 IEEE International SOI Conference. Proceedings. Durango, CO, 2001.
- [21] Y.-K. Choi, N. Lindert, P. Xuan, S. Tang, D. Ha, E. Anderson, T.-J. King, J. Bokor, and C. Hu, "Sub-20 nm CMOS FinFET technologies," presented at International Electron Devices Meeting. Technical Digest. Washington, DC, 2001.
- [22] "Taurus-Device, v. 2003.12," Synopsys Inc., 2003.
- [23] S. Takagi, A. Toriumi, M. Iwase, and H. Tango, "On the universality of inversion layer mobility in Si MOSFET's: Part II-effects of surface orientation," *IEEE Transactions on Electron Devices*, vol. 41, pp. 2363-8, 1994.
- [24] M. Yang, E. P. Gusev, M. Jeong, O. Gluschenkov, D. C. Boyd, K. K. Chan, P. M. Kozlowski, C. P. D'Emic, R. M. Sicina, P. C. Jamison, and A. I. Chou, "Performance dependence of CMOS on silicon substrate orientation for ultrathin oxynitride and HfO<sub>2</sub> gate dielectrics," *IEEE Electron Device Letters*, vol. 24, pp. 339-41, 2003.
- [25] L. Chang, S. Tang, K. Tsu-Jae, J. Bokor, and H. Chenming, "Gate length scaling and threshold voltage control of double-gate MOSFETs," presented at International Electron Devices Meeting. Technical Digest. IEDM. San Francisco, CA, 2000.
- [26] J. Kedzierski, E. Nowak, T. Kanarsky, Y. Zhang, D. Boyd, R. Carruthers, C. Cabral, R. Amos, C. Lavoie, R. Roy, J. Newbury, E. Sullivan, J. Benedict, P. Saunders, K. Wong, D. Canaperi, M. Krishnan, K. L. Lee, B. A. Rainey, D. Fried, P. Cottrell, H. S. Wong, M. Jeong, and W. Haensch, "Metal-gate FinFET and fully-

- depleted SOI devices using total gate silicidation," presented at IEEE International Electron Devices Meeting. San Francisco, CA, 2002.
- [27] P. Ranade, C. Yang-Kyu, H. Daewon, A. Agarwal, M. Ameen, and K. Tsu-Jae, "Tunable work function molybdenum gate technology for FDSOI-CMOS," presented at IEEE International Electron Devices Meeting. San Francisco, CA, 2002.
- [28] Y. Fu-Liang, H. Chien-Chao, C. Hou-Yu, L. Jhon-Jhy, C. Tang-Xuan, C. Hung-Wei, C. Chang-Yun, H. Cheng Chuan, C. Kuang-Hsin, L. Di-Hong, T. Hsun-Chih, W. Cheng-Kuo, C. Shui-Ming, S. Yi-Ming, S. Ke-Wei, C. Chi-Chun, L. Tze-Liang, C. Shih-Chang, C. Chih-Jian, C. Cheng-hung, L. Jhi-cheng, C. Weng, H. Chuan-Ping, C. Ying-Ho, C. Kuei-Shun, L. Ming, K. Li-Wei, C. Yu-Jun, L. Fu-Jye, Y. Jan-Wen, S. King-Chang, C. Bin-Chang, S. Jaw-Jung, C. Chun-Kuang, G. Tsai-Sheng, C. Bor-Wen, H. Yi-Chun, T. Han-Jan, C. Jyh-Huei, C. Yung-Shun, Y. Yee-Chia, S.-H. Fung, C. H. Diaz, C. M. Wu, B. J. Lin, M. S. Liang, J.-C. Sun, and H. Chenming, "A 65nm node strained SOI technology with slim spacer," presented at IEEE International Electron Devices Meeting 2003. Washington, DC, 2003.
- [29] S. Takagi, A. Toriumi, M. Iwase, and H. Tango, "On the universality of inversion layer mobility in Si MOSFET's: Part I-effects of substrate impurity concentration," *IEEE Transactions on Electron Devices*, vol. 41, pp. 2357-62, 1994.
- [30] A. Asenov, "Random dopant induced threshold voltage lowering and fluctuations in sub-0.1  $\mu\text{m}$  MOSFET's: A 3-D "Atomistic" simulation study," *IEEE Transactions on Electron Devices*, vol. 45, pp. 2505-13, 1998.

- [31] Y. K. Choi, T. J. King, and C. M. Hu, "A spacer patterning technology for nanoscale CMOS," *IEEE Transactions on Electron Devices*, vol. 49, pp. 436-441, 2002.
- [32] S. M. Sze, *Physics of Semiconductor Devices*, 2 ed: Wiley-Interscience, 1981.
- [33] J. W. Tschanz, J. T. Kao, S. G. Narendra, R. Nair, D. A. Antoniadis, A. P. Chandrakasan, and V. De, "Adaptive body bias for reducing impacts of die-to-die and within-die parameter variations on microprocessor frequency and leakage," presented at 2002 IEEE International Solid-State Circuits Conference. Digest of Technical Papers. San Francisco, CA, 2002.
- [34] A. Keshavarzi, J. W. Tschanz, S. Narendra, V. De, W. R. Daasch, K. Roy, M. Sachdev, and C. F. Hawkins, "Leakage and process variation effects in current testing on future CMOS circuits," *IEEE Design & Test of Computers*, vol. 19, pp. 36-43, 2002.
- [35] M. Jeong, E. C. Jones, T. Kanarsky, Z. Ren, O. Dokumaci, R. A. Roy, L. Shi, T. Furukawa, Y. Taur, R. J. Miller, and H. S. Wong, "Experimental evaluation of carrier transport and device design for planar symmetric/asymmetric double-gate/ground-plane CMOSFETs," presented at International Electron Devices Meeting. Technical Digest. Washington, DC, 2001.
- [36] L. Mathew, Y. Du, A.-Y. Thean, M. Sadd, A. Vandooren, C. Parker, T. Stephens, R. Mora, R. Rai, M. Zavala, D. Sing, S. Kalpat, J. Hughes, R. Shimer, S. Jallepalli, G. Workman, W. Zhang, J. G. Fossum, B. E. White, B. Y. Nguyen, and J. Mogab, "CMOS Vertical Multiple Independent Gate Field Effect Transistor (MIGFET)," presented at 2004 IEEE International SOI Conference. Charleston, SC, 2004.

- [37] L. Mathew, M. Sadd, B. E. White, A. Vandooren, S. Dakshina-Murthy, J. Cobb, T. Stephens, R. Mora, D. Pham, J. Conner, T. White, Z. Shi, A.-Y. Thean, A. Barr, M. Zavala, J. Schaeffer, M. J. Rendon, D. Sing, M. Orłowski, B. Y. Nguyen, and J. Mogab, "Finfet with isolated n+ and p+ gate regions strapped with metal and polysilicon," presented at 2003 IEEE International SOI Conference. Proceedings. Newport Beach, CA, 2003.
- [38] M. Yamaoka, K. Osada, R. Tsuchiya, M. Horiuchi, S. Kimura, and T. Kawahara, "Low power SRAM menu for SOC application using Yin-Yang-feedback memory cell technology," presented at 2004 Symposium on VLSI Circuits. Digest of Technical Papers. Honolulu, HI, 2004.
- [39] S. Borkar, T. Karnik, S. Narendra, J. Tschanz, A. Keshavarzi, and V. De, "Parameter variations and impact on circuits and microarchitecture," presented at Proceedings 2003. Design Automation Conference. Anaheim, CA, 2003.
- [40] T. Karnik, V. De, and S. Borkar, "Statistical design for variation tolerance: key to continued Moore's law," presented at 2004 International Conference on Integrated Circuit Design and Technology. Austin, TX, 2004.

# Chapter 6 : FinFET SRAM process development

## 6.1 Introduction

Among all DG transistor structures proposed so far as potential solutions for SRAM scaling, the FinFET is the most manufacturable because the front- and back- gates are self aligned and their dimensions can be controlled lithographically [1-3]. Independent gate FinFETs, in which the front- and back-gate can be biased separately have been demonstrated as well [4, 5]. The front gate can be used to switch the device on-off, whereas the back-gate can be used to set the  $V_{TH}$  to the required level. Conventional 6-T cell designs based on FinFETs have also been demonstrated to provide stable, low power SRAMs. [6-9]

In this work, a process has been developed to enable the fabrication of FinFET based SRAMs with dynamic feedback to boost static noise margin with no associated layout area or leakage penalty. This requires the use of a combination of double-gated FinFETs and independent-gated FinFETs within the SRAM cell (Figure 2.1). While double-gated FinFETs and independent-gate FinFETs have been demonstrated separately, a process to integrate both these types of transistors within a dense SRAM cell has not been demonstrated before. The process technology required to implement SRAMs with dynamic feedback is detailed herein.

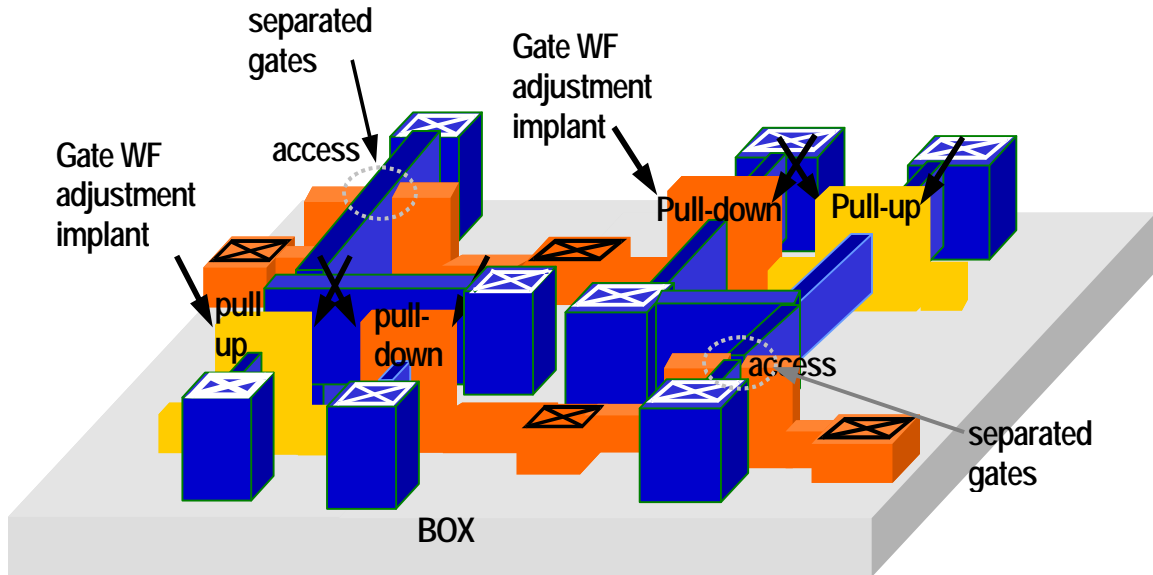


Figure 6.1: (a) 3-D schematic of a 6-T SRAM cell with dynamic feedback using a combination of double-gate and independent gate FinFETs. The gates of the access transistors are to be separated selectively for independent-gate operation.

## 6.2 FinFET SRAM fabrication

The starting material is a (001)-surface p-type ( $N_{\text{body}} = 10^{15} \text{ cm}^{-3}$ ) SOI wafer with a 400nm buried oxide (BOX) produced by SOITEC, Inc [10]. The initial SOI film thickness of 100nm is reduced to 50nm by wet oxidation at 850°C followed by wet etching in HF to remove the thermally grown oxide. Prealignment marks (PM), 120 nm deep (50 nm of Si + 70 nm into the BOX layer), needed for alignment purposes in the ASM Lithography (ASML) 248 nm DUV stepper are etched into the wafer using a  $\text{CF}_4 + \text{O}_2$  plasma in the Lam Research model 9400 TCP Poly-Si etcher (Lam5).

Next, an oxide-nitride-oxide (O-N-O) hard mask stack is deposited using low pressure chemical vapor deposition (CVD) on top of the silicon layer. The O-N-O layer protects the silicon active layer during the gate over etch step, needed to clear the gate

material from the fin sidewalls completely. An O-N-O stack is used instead of oxide alone in order to partially retain some hard mask needed to protect the fin during the subsequent gate-sidewall spacer (oxide) overetch step.

The active areas are defined using the ASML stepper. In order to achieve a higher printed line resolution, a thin photoresist layer (400nm) thick is used. The resist is soft-baked at 130°C for 1 minute before exposure and at 130°C for 1 min after exposure, respectively before it is developed. Then an ultraviolet light assisted hard bake (UVbake) is performed to harden the resist. Resist ashing in the Technics PE II, oxygen-plasma system is performed at low power to reduce the printed linewidth of the resist patterns controllably. The plasma power is set to 30W, with O<sub>2</sub> pressure 300mTorr and the flow rate 51.1 sccm. The resist ashing rate after UVbake is 30nm/min, translating to a linewidth reduction rate of 60 nm/min.

### **6.2.1 Cone defects formed during fin etching**

The fin patterning process involves etching of the O-N-O fin hard mask stack followed by the Si fin etching. When this stack is etched sequentially in Lam5, until the Si endpoint signal is seen indicating the completion of the fin etching, some residue remains on top of the BOX (Figure 6.2). This residue cannot be removed by O<sub>2</sub> plasma ashing, H<sub>2</sub> plasma ashing, or wet cleaning in dilute HF and piranha (hot H<sub>2</sub>SO<sub>4</sub> + H<sub>2</sub>O<sub>2</sub>). The residue looks like pillars that are typically less than ~10-20 nm in diameter, and can only be detected under the scanning electron microscope (SEM), suggesting it is actually comprised of small silicon pillars. The pillars have a characteristic "cone" like appearance, which indicates that they were formed by small residual defects that acted as micromasks during the Si fin etching process.

During the course of investigating these defects, several ways have been found to limit their formation.

1. Cone defects are not seen after the hard mask etch. (Figure 6.3). This together with its etch resistance to dilute HF shows that the cone defect is not an oxide defect, but rather a Si defect.
2. After the fin hard mask etching, a  $\text{Cl}_2+\text{HBr}$  plasma is used to etch the Si, and the cone defects appear (Figure 6.4). Also the use of the  $\text{HBr}+\text{O}_2$  plasma overetch recipe with a high selectivity of Si :  $\text{SiO}_2$  does not remove this defect, suggesting that the Si cones are micromasked, preventing them from being etched. After the O-N-O hard mask etch, the resist is stripped in an  $\text{O}_2$  plasma followed by a piranha clean, resulting the formation of a native oxide. A long native oxide removal step helps to reduce the density of the cone defects, but they are not completely eliminated.
3. If a  $\text{CF}_4 +\text{O}_2$  plasma in the Lam5 etcher is used to etch both the O-N-O stack and the fin, no cone defects are seen (Figure 6.5). However, this has very low selectivity to the underlying buried oxide and can therefore not be used
4. When a  $\text{CF}_4 / \text{CHF}_3$  plasma in the Applied Materials Centura Platform System MxP<sup>+</sup> Chamber (Centura-mxp) is used to etch the O-N-O stack, no cone defects are seen (Figure 6.6). However, this process produces a large sidewall slope in the hard mask making it unsuitable for Si fin etching.



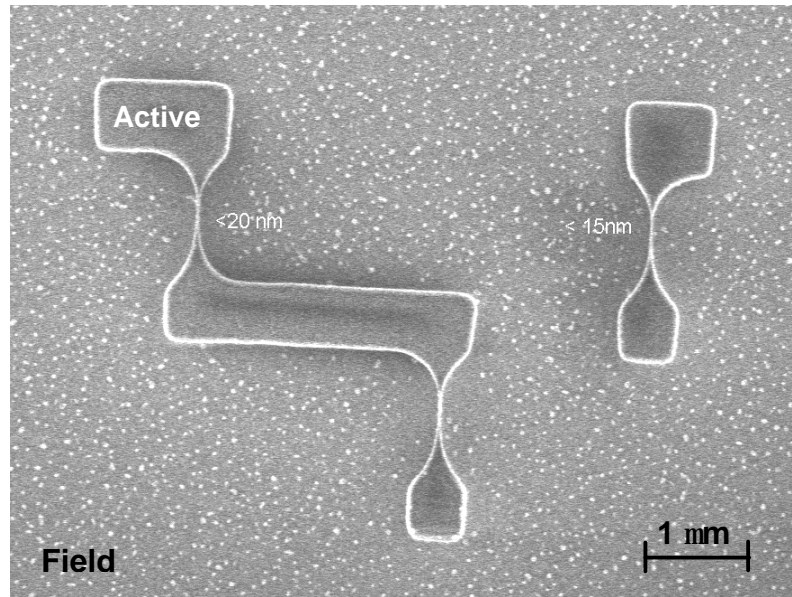


Figure 6.2: Residue in the field (exposed BOX) regions are seen after O-N-O hard mask stack + Si etch.

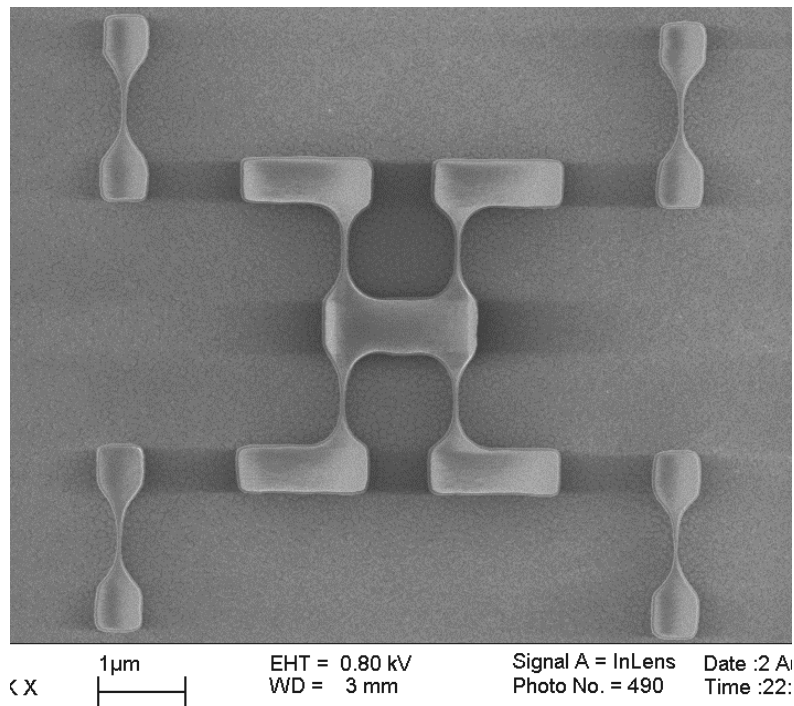


Figure 6.3: No Cone defects are seen after O-N-O hard mask stack etch alone. (No Si fin etch has been done.)

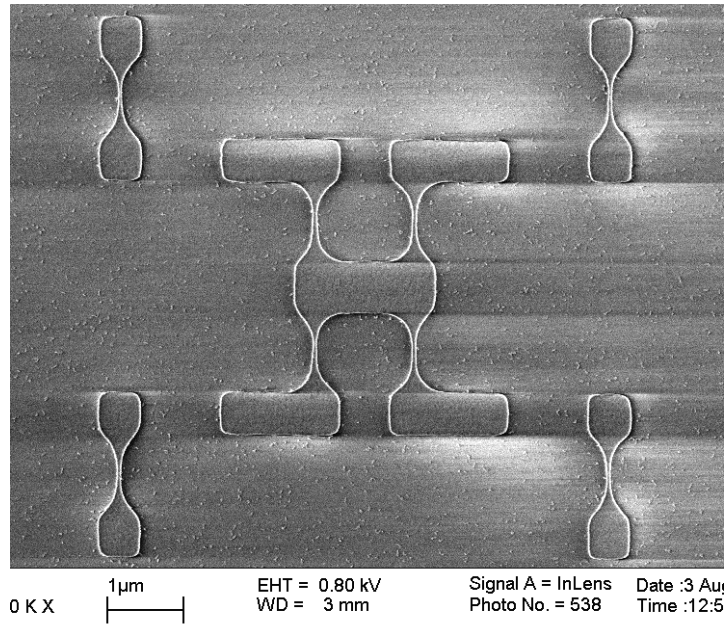


Figure 6.4: Cone defects are seen after Si fin etch using  $\text{Cl}_2+\text{HBr}$  plasma etch following O-N-O hard mask etch.

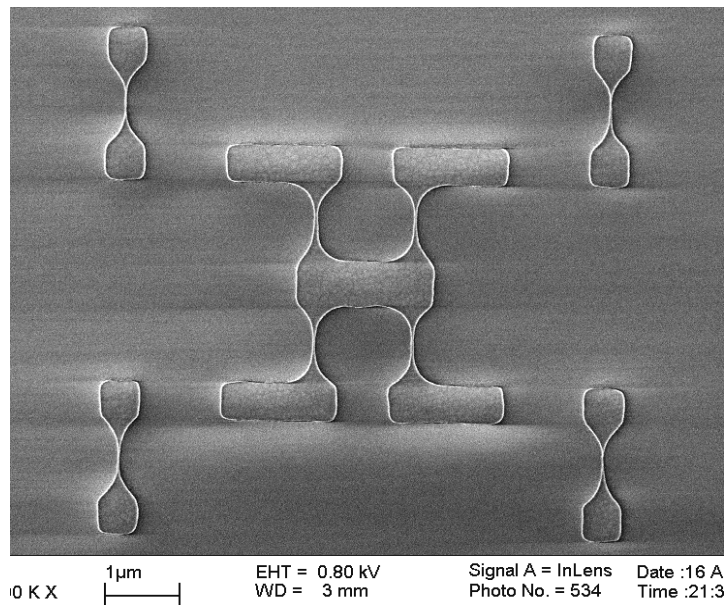


Figure 6.5: No cone defects are seen after using a  $\text{CF}_4+\text{O}_2$  plasma etch (native oxide breakthrough recipe) to etch the O-N-O hard mask and the Si fin. The limitation of a  $\text{CF}_4+\text{O}_2$  plasma etch process is its low Si :  $\text{SiO}_2$  etch selectivity.

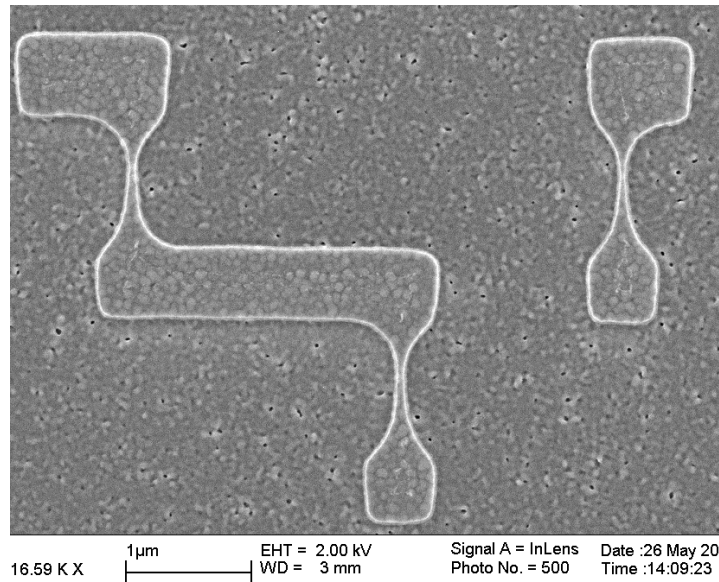


Figure 6.6: No cone defects are seen after O-N-O hard mask stack etch in the Centura-mxp using a  $\text{CF}_4/\text{CHF}_3$  recipe. The large sidewall slope induced during the etching makes it unsuitable for fin patterning, however.

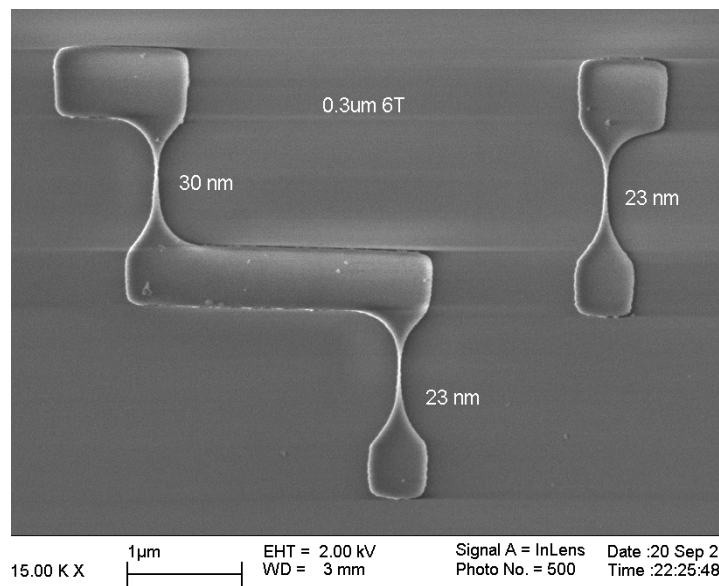


Figure 6.7: SEM image taken after the optimal etch process. A combination of a long  $\text{CF}_4+\text{O}_2$  plasma etch (BT step) to etch the O-N-O hard mask and partially etch the Si fin, and a  $\text{Cl}_2+\text{HBr}$  plasma etch to complete the Si etch was used. The subsequent sacrificial oxidation step removes any organic residue that remains.

The final process developed to pattern the active region consists of a combination of a long  $\text{CF}_4+\text{O}_2$  plasma etch (breakthrough etch) in the Lam5 etcher to etch the O-N-O hard mask and a small part of the Si fin. After resist removal and subsequent wet cleaning, more breakthrough etching is done to remove the native oxide and intentionally etch the Si fin partially, followed by a  $\text{Cl}_2+\text{HBr}$  plasma etch to complete the fin etch. A 3nm sacrificial thermal oxide is subsequently grown to remove any residue as well as to heal any dry etch damage from the fin sidewalls. The sacrificial oxidation followed by dilute HF etching removes all the remaining cone defects as well (Figure 6.7).

### 6.2.2 Gate stack deposition

A 1.8nm gate oxide is thermally grown on the Si fin at  $675^\circ\text{C}$  for 12 min followed by a high temperature anneal at  $900^\circ\text{C}$  for 15min to improve the oxide quality. Then 200nm of in-situ boron doped  $\text{Si}_{0.45}\text{Ge}_{0.55}$  and 100nm of low temperature oxide (LTO) hard mask are deposited by LPCVD, consecutively. The gate hard mask protects the gate from unintentional counter-doping during the source/drain implantation. LTO, deposited at  $450^\circ\text{C}$ , is used for the gate hard mask instead of high temperature oxide (HTO) or silicon nitride, both of which are deposited by CVD at  $800^\circ\text{C}$ . This is to minimize boron penetration from the  $\text{p}^+$ -gate through the gate oxide as the temperature stabilization in the CVD furnace takes a few hours. The workfunction of choice to enable the design of stable low power FinFET-based SRAM is in the range 4.65-4.85 eV, and while there are multiple metal gate candidates available,  $\text{p}^+ \text{Si}_{1-x}\text{Ge}_x$  ( $x > 0.5$ ) has a workfunction  $\sim 4.8$  eV and can be easily integrated with a CMOS process.

In order to determine the workfunction of in-situ boron doped  $\text{Si}_{0.45}\text{Ge}_{0.55}$ , capacitors were fabricated on bulk-Si wafers. The gate workfunction extraction requires

the measurement of the flatband voltage,  $V_{FB}$ , as function of oxide thickness,  $T_{OX}$ , from capacitor measurements. The "metal-to-semiconductor" work-function difference,  $F_{MS}$ , is defined to be the difference in the work functions of the gate material,  $F_M$ , and the Si substrate,  $F_S$ . From a plot of  $V_{FB}$  versus  $T_{OX}$ , the intercept can be used to extract the  $F_M$ , while the slope gives the fixed oxide charge per unit area,  $Q_F$  [11],

$$V_{FB} = F_M - F_S - \frac{Q_F}{e_{OX}} T_{OX} \quad (6-1)$$

Capacitors with multiple oxide thicknesses were fabricated, and the measured C-V curves were fit using the Quantum C-V simulator (QMCV)[12]. The starting wafers were (001) Si with 10 $\Omega$ -cm bulk resistivity and they were oxidized in dry O<sub>2</sub> for 14.5 min at 1000 °C to grow 240 Å of oxide. The oxide was then selectively etched in 25:1 dilute HF (thermal oxide etch rate 65 Å/min) to create 4 different thicknesses on one wafer – 40 Å, 125 Å, 148 Å, and 240 Å. Then 135 nm of the gate material, in-situ boron doped Si<sub>0.45</sub>Ge<sub>0.55</sub> was then deposited using B<sub>2</sub>H<sub>6</sub> for doping, followed by 500 Å of LTO to protect the gate material during rapid thermal annealing (RTA). RTA was then carried out in the RTA chamber (heatpulse3) for 1min at 850 °C followed by LTO removal. Due to relatively the low temperature activation, the sheet resistivity was 2.8 m $\Omega$ -cm corresponding to 3x10<sup>19</sup> cm<sup>-3</sup> active dopant concentration. Gate lithography was carried out followed by dry etching to pattern the capacitor gate electrodes.

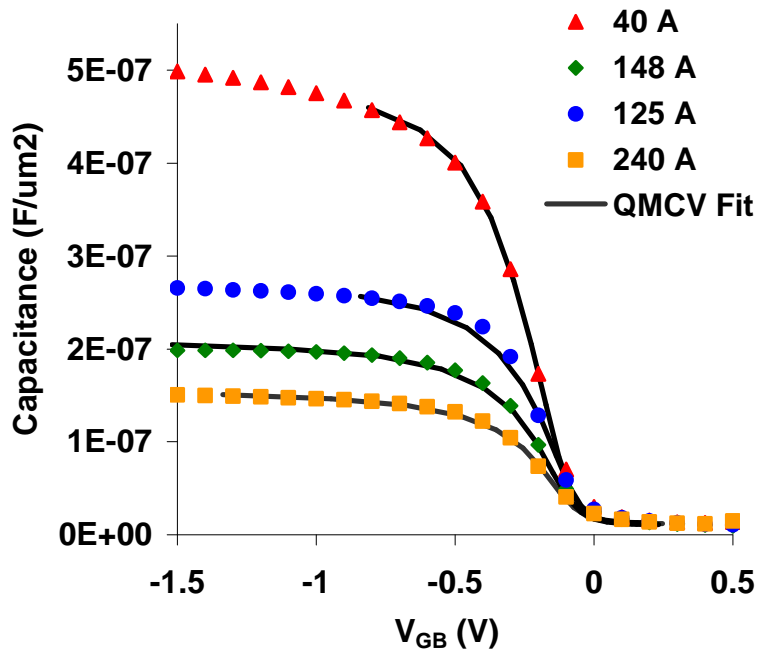


Figure 6.8: HFCV measurements of capacitors with  $p^+-Si_{0.45}Ge_{0.55}$  gate, and their corresponding fit using the QMCV simulator.

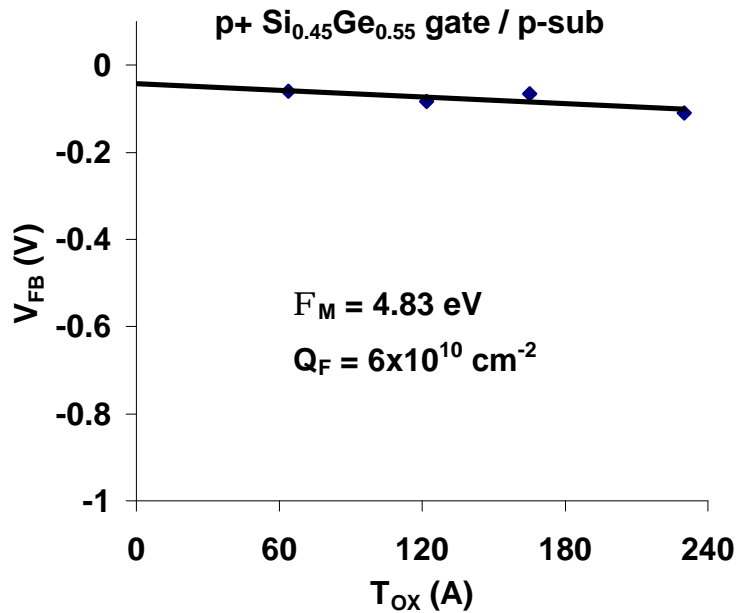


Figure 6.9: When the extracted  $V_{FB}$  of  $p^+ Si_{0.45}Ge_{0.55}$  gate is plotted against  $T_{OX}$ , the  $\Phi_M$  is extracted to be 4.83 eV.

The high-frequency capacitance versus voltage (HFCV) data measured at 100 kHz (Figure 6.8) was used in conjunction with the QMCV simulator to determine the  $V_{FB}$  and extract  $F_M$ . From Figure 6.9, the workfunction of  $p^+$ -Si<sub>0.45</sub>Ge<sub>0.55</sub> gate was extracted to be 4.83 eV, and is found to be consistent with data from King *et al.* [13, 14]

### 6.2.3 Gate patterning

Sub-40nm gate electrodes are defined by DUV lithography, photoresist ashing, hard mask trimming and plasma etch. The gate lithography needs the use of a bottom anti-reflection coating (BARC) to improve the printed line resolution. Standing wave effects seen in lithography arise from the interference between the incoming light wave and the light reflected from the silicon substrate. As the critical dimensions of IC technology become smaller and smaller, the effects of standing waves have a greater impact on sidewall angles, CD control, and exposure intensity. Standing wave effects can be diminished by using a BARC layer to reduce reflectivity within the photoresist system through absorbance or destructive interference. Figure 6.10 shows the shallow sidewall slope of the photoresist feature after development when the BARC is not used.

The BARC is partially removed during photoresist development, sometimes leaving behind a non-uniform surface (BARC islands) on the developed area. An extra step is normally needed to completely remove the BARC before gate etching. However, if O<sub>2</sub> plasma ashing is used to reduce the printed photoresist line width, a separate dry etch step is not needed to remove the organic BARC.

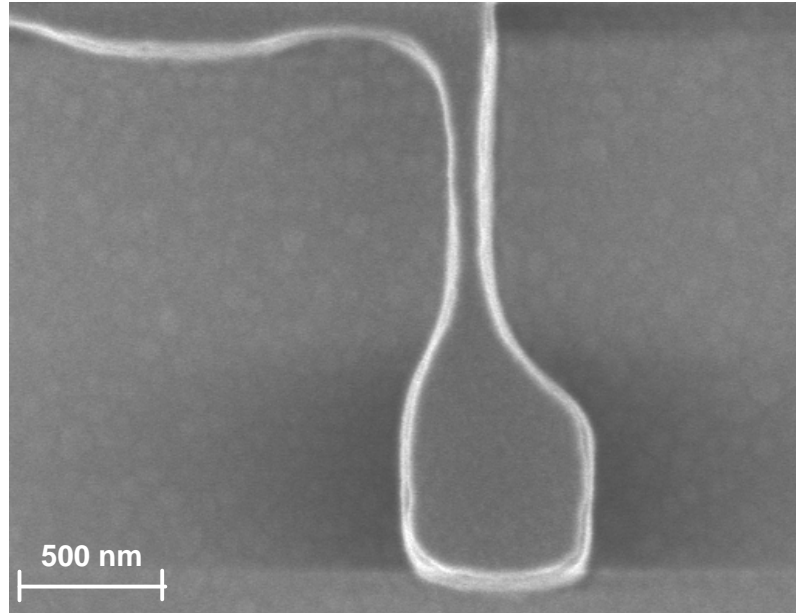


Figure 6.10: Large gate line sidewall slope is seen when the BARC is not used.

After resist ashing to form sub-50 nm gate lines, the oxide hard mask is etched to transfer the pattern. After the photoresist is stripped, oxide hard mask trimming in dilute (100:1) HF reduces the line width from 50nm to 40nm. The  $p^+$ - $\text{Si}_{0.45}\text{Ge}_{0.55}$  gate is etched in two steps: the main etch (ME) with a  $\text{Cl}_2+\text{HBr}$  plasma produces a vertical etching profile but has relatively low etch selectivity (poly-  $\text{Si}_{0.45}\text{Ge}_{0.55}:\text{Oxide} = 25:1$ ); the overetch (OE) with a  $\text{HBr}+\text{O}_2$  plasma that provides a poor sidewall profile, but higher selectivity ( $p^+-\text{Si}_{0.45}\text{Ge}_{0.55}:\text{Oxide} = 400:1$ ) thereby minimizing BOX recess. The OE step has bad selectivity to photoresist because the recipe contains  $\text{O}_2$ . This is the reason why an oxide hard mask that offers excellent etch resistance is used to pattern the gate electrodes. 4-T and 6-T SRAM cells after gate etching are shown in Figure 6.11 and Figure 6.12, respectively.



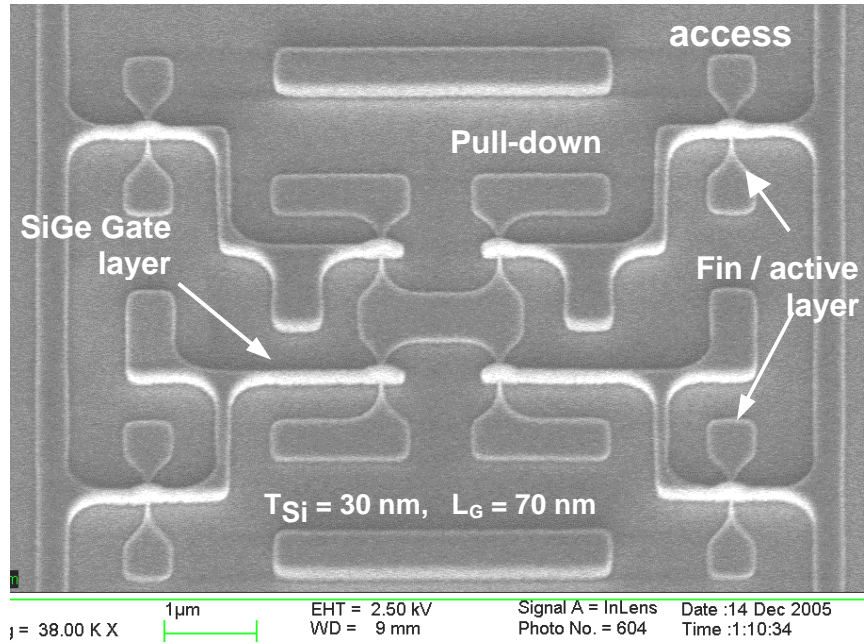


Figure 6.11: Tilted SEM picture of 4T SRAM cell after gate patterning.

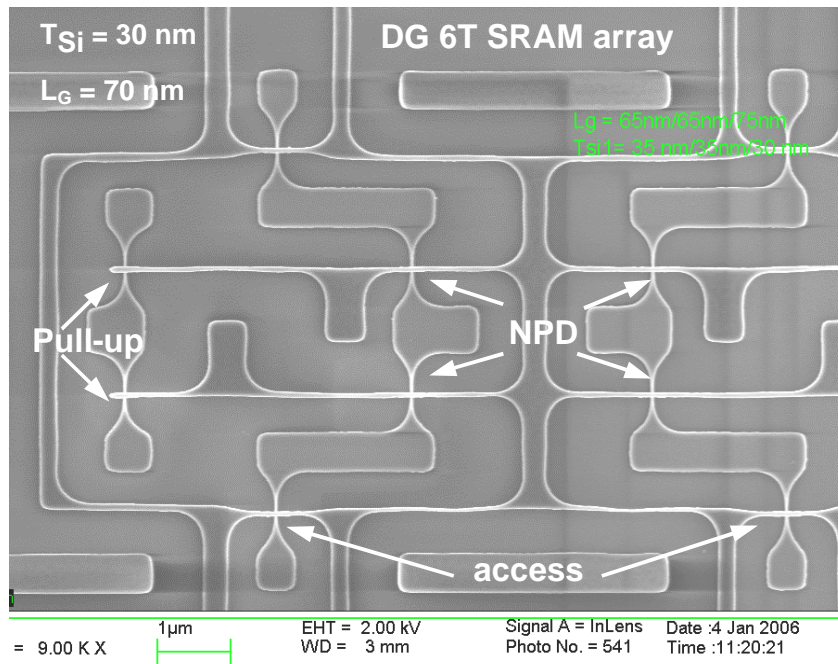


Figure 6.12: SEM picture of 6T SRAM cells w/feedback after gate patterning.

After gate formation, 27nm of LTO is deposited and etched back anisotropically to make gate-sidewall spacers. The spacers offset the n<sup>+</sup> / p<sup>+</sup> implants needed to form the heavily doped source/drain junctions, control the effective channel length from becoming too short and also reduce overlap capacitance between the gate and the source/drain regions. Using n<sup>+</sup> and p<sup>+</sup> select implantation masks, phosphorus is implanted at 30 keV, and 0° tilt (dose = 5 x 10<sup>15</sup>cm<sup>2</sup>) while boron is implanted at 10 keV, and 0° tilt (dose = 2x10<sup>15</sup>cm<sup>2</sup>). The implant energy was chosen so that the peak of the implantation is just below the top of the Si fin to ensure that the fin is not completely amorphized by the heavy dose implantation. The wafers are annealed at 600°C for 4 hours to recrystallize any amorphized portion of the silicon fin using the damage-free part of the fin below as the epitaxial template.

#### **6.2.4 Gate Planarization and Selective Gate Separation**

In order to establish dynamic feedback in 6-T SRAM cells, the storage node needs to be connected to the back-gate of the access transistor, so that the strength of the access transistor can be selectively decreased. In order to do this, the access transistors need to have their gates separated selectively while leaving the other transistors gates connected. Before gate planarization, 50nm of a LTO cap layer is deposited to act as a mask to protect the Si fin during the gate separation etch and is used for widening the process window for the gate separation etch. This is because the O-N-O fin hard mask stack is recessed during the gate over etch step and the gate sidewall spacer etch.

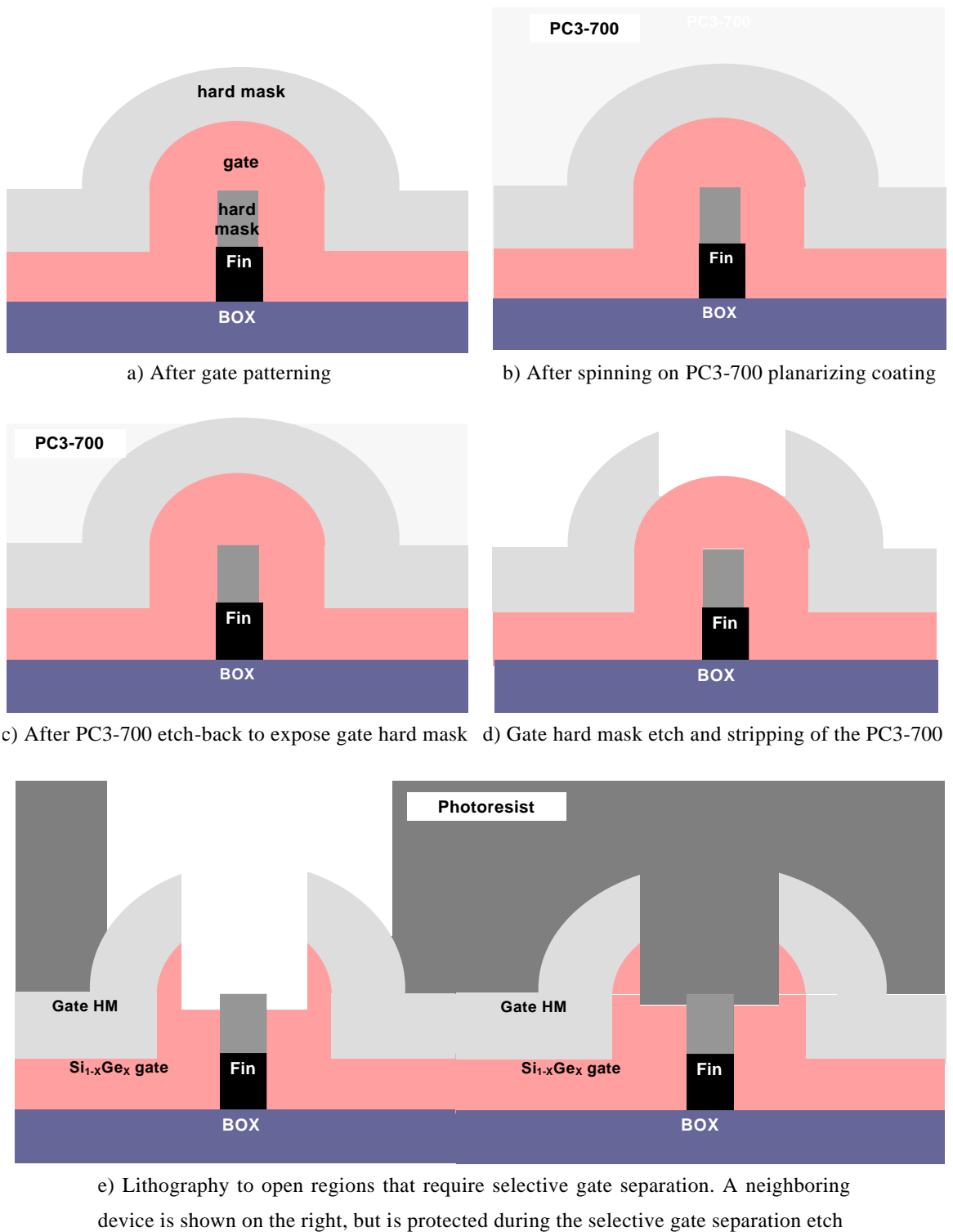


Figure 6.13: Schematic illustrations (cross-sections along gate electrode) of process steps selective gate separation

The selective gate separation etch-back process is broken into the following steps: gate planarization using resist etch-back, hard mask oxide etch, gate separation lithography and gate separation etch as shown in Figure 6.13.

A resist etch-back process with an organic coating, PC3-700 from Futurrex, has been used for gate planarization [15]. The resist was used to planarize the gate layer by taking advantage of its reflow characteristics (resulting in a non-conformal profile after hard bake), and a blanket etch was used to etch back the gate layer. The coating thickness should nominally be more than twice the wafer topography (~300 nm) for the FinFET so that when the resist reflows, the top of the gate hard mask is well covered. 680 nm of the PC3-700 is coated at 3000 rpm / 40 sec. The coating is not very viscous and can be spun down to about 4000 Å thickness without the need for using a solvent or a thinning agent in the mixture. Then a hard bake is done to reflow the resist at 200 °C for 2 min to reflow the coating and planarize the wafer surface.

Blanket etch back of the organic planarization layer is then performed so as to just expose the top of the gate hard mask. This ensures that the hard mask is removed for all transistors in the region where the gate runs over the fin (highest topography), while the fin hard mask is kept intact under the planarizing coating to ensure that the fins are not accidentally etched during the subsequent gate separation etch. Low power O<sub>2</sub> plasma ashing @ 50 W using the Technics-C plasma system was initially used to etch back the resist. When the etched-back resist was examined under the SEM, the surface was found to be rough and non-uniform, making it unsuitable for use in the etch-back process.

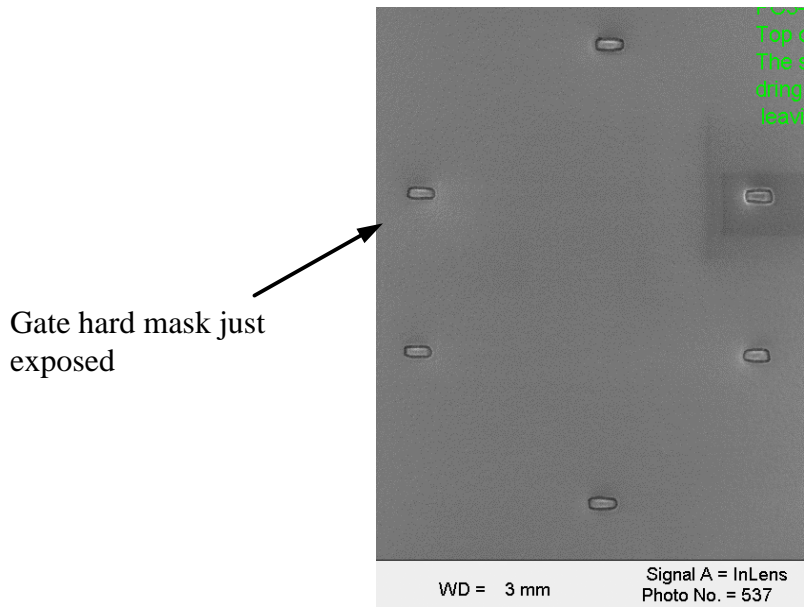


Figure 6.14: SEM picture of 6T SRAM array after planarizing coating etch back in  $\text{CF}_4 + \text{O}_2$  plasma. The etching is timed so as to just expose the top of the gates. The gate-sidewall spacers get etched partially (during over etch) leaving behind a dark ring around the gate.

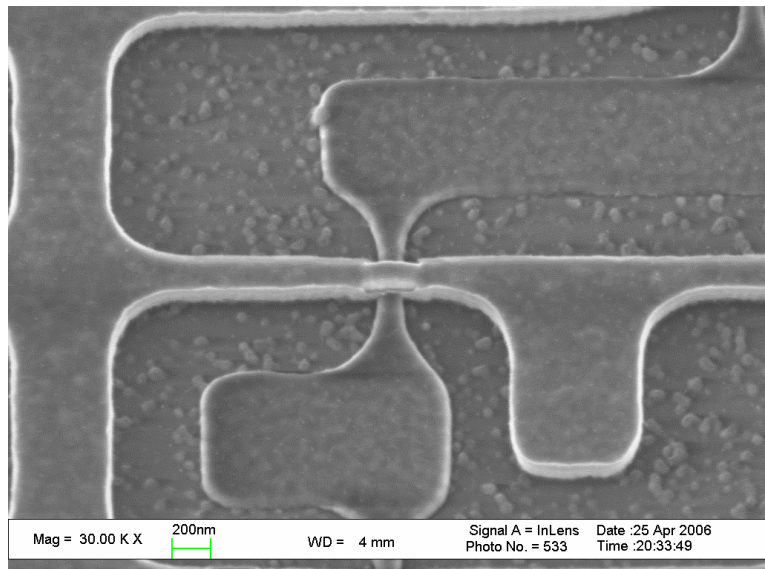


Figure 6.15: SEM picture of 6T SRAM array after gate planarization and hard mask etch. The etch selectivity to oxide is good, so that the  $\text{Si}_{0.45}\text{Ge}_{0.55}$  gate is not etched.

The coating was found to etch in a CF<sub>4</sub> plasma in the Lam5 etcher without roughening up. The etch rate of the coating was found to 1100 Å/min, giving an etch selectivity of 1:1 to oxide. In order to improve the selectivity to oxide, 20 sccm of O<sub>2</sub> was added to the recipe to increase the PC3-700 coating etch rate to 2100 Å/min (Recipe a in Table 6-1). The benefit of a using CF<sub>4</sub> + O<sub>2</sub> etch recipe is a uniform and smooth etching front with reasonable PC3-700:oxide etch selectivity. Figure 6.14 shows the wafer surface after planarization coating etch-back just exposing the top of the gate hard mask.

<b>Etching parameters</b>	<b>Coating etch-back<sup>(a)</sup></b>	<b>Oxide etch-back<sup>(a)</sup></b>	<b>Poly etch-back<sup>(c)</sup></b>
Pressure (mTorr)	15	15	35
RF top power (W)	200	200	250
RF bottom power (W)	40	40	120
CHF <sub>3</sub> (sccm)	0	0	0
Cl <sub>2</sub> (sccm)	0	0	0
HBR (sccm)	0	0	200
O <sub>2</sub> (sccm)	20	0	5
Ar (sccm)	0	0	0

Table 6-1: Lam5 etch recipes used in the gate separation process

After the gate planarization is done, the hard mask oxide is etched in the Centura-MxP<sup>+</sup> dielectric etch chamber using recipe (3) in Table 6-2 that is highly selective to the underlying Si<sub>0.45</sub>Ge<sub>0.55</sub> layer (Figure 6.15). The use of CHF<sub>3</sub> degrades the oxide sidewall slope, but is used because of its high selectivity.

The gate separation lithography is done in the ASML 248 nm DUV stepper using the inverse of the Si fin patterns to create holes in the resist to expose the transistors that need to be made independent-gated (only access transistors). After developing the resist,

the gate separation etch is done in the Lam5 etcher using recipes (b) and (c) in Table 6-2. The etching is timed so as to etch the gate running on top of the fin completely and just expose the fin hard mask as seen in Figure 6.16. In the unexposed regions the gates are left connected as shown in Figure 6.17. The gate hard mask oxide shields the gate line and protects the gate poly-  $\text{Si}_{0.45}\text{Ge}_{0.55}$  during the etch-back outside of the region where it runs over the fin.

Recipe Parameters	MXP-OXIDE-ETCH	MXP-OXSP ETCH	MXP-VAR-ETCH
Purpose	Std. Oxide Etch <sup>(1)</sup>	Oxide Spacer Etch <sup>(2)</sup>	High selectivity <sup>(3)</sup>
Power (W)	700	500	500
Pressure (mT)	200	200	200
Ar flow	150	120	120
CF <sub>4</sub> flow	15	10	-
CHF <sub>3</sub> Flow	45	50	60
Oxide Etch Rate	4500 Å/min	3100 Å /min	2200 Å /min
Selectivity	Oxide:Si = 9:1	Oxide:Si = 11:1	Oxide:Si ~100:1

Table 6-2: Standard oxide etch recipes (1), (2) and modified recipe (3) used in the Centura- MxP+ chamber. The standard recipe was modified to flow only CHF<sub>3</sub> to achieve high selectivity to Si [16]

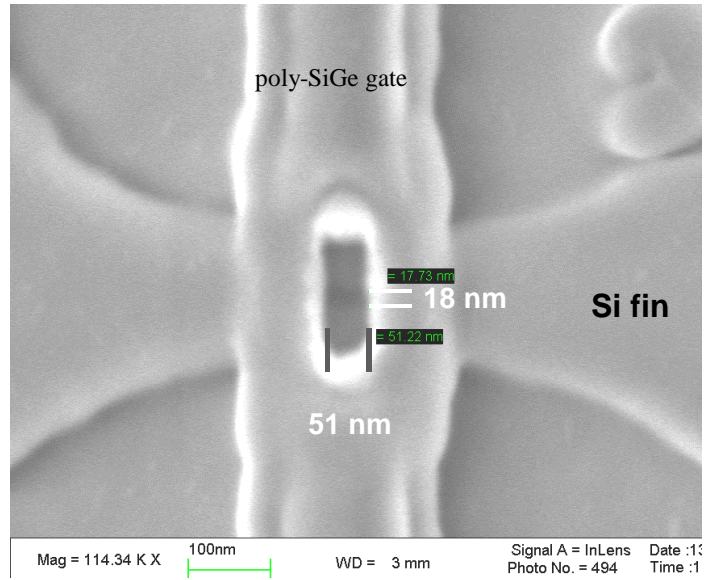


Figure 6.16: SEM image of access transistor after gate separation etch. The gate separation etch is timed to etch the gate on top of the fin completely and just expose the fin hard mask.

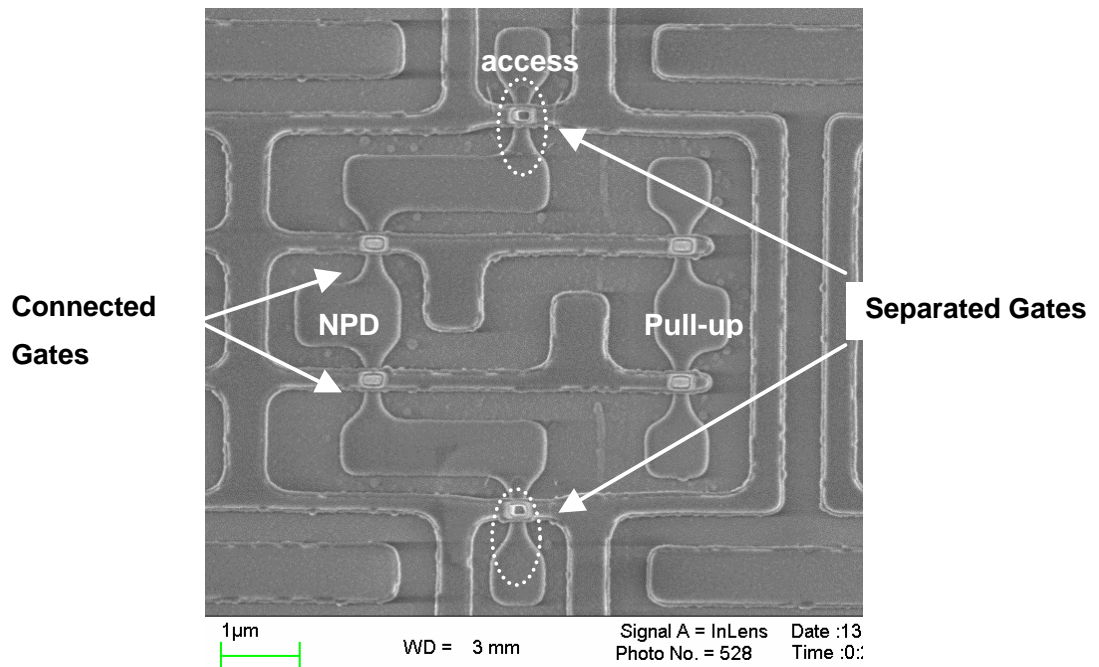


Figure 6.17: SEM picture of 6T SRAM array after timed gate separation etch. The gates of the access transistors are selectively separated to establish dynamic feedback. The roughness is related to the hard etching during the gate planarization.



## 6.2.5 Problems encountered in gate separation etch

Even though a resist etch-back process to implement gate separation is complicated, it does not require novel or advanced equipment. One drawback of the resist etch-back process is the formation of pinholes after the hard bake. This usually happens around the edge of the wafers, leading to a loss of up to 20% of the dies. This can potentially be avoided by further studies on coating reflow characteristics.

Another problem associated with the use of a planarizing agent is the layout dependency on the degree of planarization. The reflow characteristics of the coating are not adequate enough to ensure a truly planar top surface after hard bake. The degree of reflow is affected by the density of features, thereby exhibiting layout dependencies. (Dense features inhibit the free reflow of the coating.) This can only be avoided by using appropriate dummy features like those used in chemical mechanical polishing (CMP).

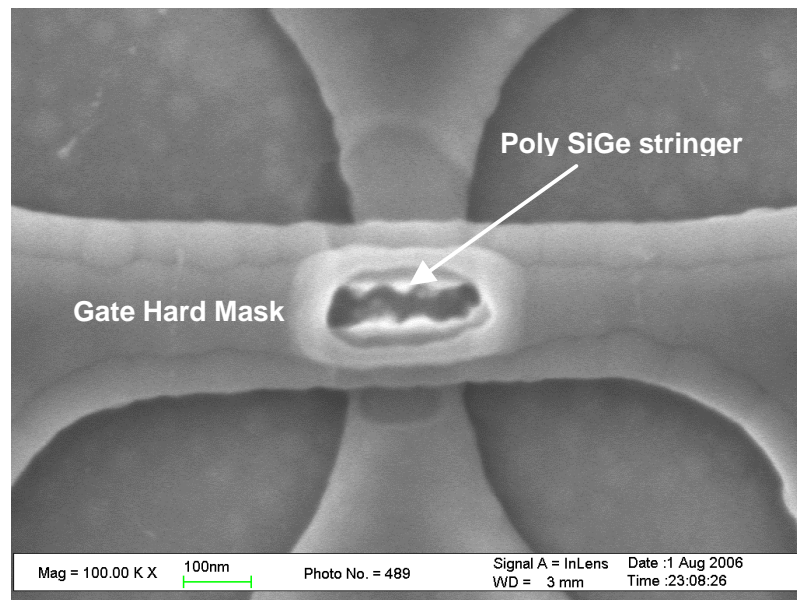


Figure 6.18: SEM picture after a long gate separation etch leaving behind poly stringers along the gate sidewall spacers.

The gate separation etch is done inside a small contact hole that is bounded by the gate hard mask on two sides and the gate sidewall spacers on the other two sides. During the gate separation etch the gate material adjacent to the gate sidewall spacer is not etched completely leaving behind poly-gate stringers. This results in incomplete gate separation and the two gates remain connected through the stringers. Increasing the etch time to get rid of the stringers causes the gate line to be completely etched away along the fin sidewall as seen in Figure 6.18. Also, adequately characterizing the etch depth and sidewall profile can be quite challenging. The small hole size precludes the use of conventional step height profilometers and even an atomic force microscope (AFM) measurement.

This problem can be avoided by using sufficient gate hard mask over etch after gate planarization to also recess the gate-sidewall spacer significantly. However, the fin hard mask may also get etched during this over etch, causing the Si fin to be etched during the subsequent gate separation etch. If the poly-stringer is not too thick, it can be oxidized to ensure electrical isolation between the two gates. However, Boron penetration from the  $p^+$ -doped into the oxide during high temperature annealing presents an upper limit on the thermal budget associated with such a step. In summary, selective gate separation etch can be implemented, but is a fairly complex process with narrow process windows due to the layout dependencies of the planarization and requires good process control to implement successfully and repeatedly.

### **6.2.6 Metallization**

Rapid thermal annealing (RTA) in heatpulse3 is to be used to activate dopants. The thermal budget is to be limited to at 850C/1min or 900C/10 sec, because boron

penetration has been observed at 950 °C 30sec from BF<sub>2</sub> implanted polycrystalline-Si<sub>0.8</sub>Ge<sub>0.2</sub> through 25 Å SiO<sub>2</sub>. (In the first lot, a RTA should be repeatedly used to find the optimized annealing conditions of dopant activation.)

400nm of LTO is deposited using CVD to serve as a passivation layer to avoid shorting transistors and interconnection lines. Contact holes for interconnections are opened using the ASML stepper followed by CF<sub>4</sub>+CHF<sub>3</sub> plasma based oxide etch in centura-mxp with good selectivity (oxide:silicon ~ 9:1). Aluminum, 400 nm thick, can be deposited in the Novellus sputtering system. A pre sputter-etch step is needed to remove native oxide from the bottom of vias or contacts, so that ohmic contacts can be achieved between the Al lines and the underlying active and gate layers. Metal patterning also requires the use of BARC to reduce the surface reflectivity and improve the printability. After metal patterning is done in (Lam3 aluminum etcher or wet etching), the wafers need to be sintered at 400°C in N<sub>2</sub>:H<sub>2</sub>=9:1 before they can be electrically tested.

### **6.3 Summary**

FinFET-based SRAMs w/ dynamic feedback require the simultaneous fabrication of double- and independent- gate FinFETs and special processes needed for their successful integration into a conventional CMOS flow have been demonstrated here. These include gate planarization using etch-back, and selective gate separation. A planarizing agent is used for the etch-back and lithography is used to select transistors whose gates need to be separated. The planarization and etch-back process is a low temperature process and can be therefore be easily used for applications that have constrained thermal budgets. The key to the functionality of the etch-back process is the non-conformality of the coating used. Even though the planarization and etch-back

processes are easy to simple to integrate, layout density dependencies of the planarization process reduce the resist etch-back and gate separation etch process margins. Selective gate separation etching has been demonstrated, but the process complexity together with narrow process margins necessitates good process control to implement successfully and repeatedly.

## 6.4 References

- [1] D. Hisamoto, L. Wen-Chin, J. Kedzierski, E. Anderson, H. Takeuchi, K. Asano, K. Tsu-Jae, J. Bokor, and H. Chenming, "A folded-channel MOSFET for deep-sub-tenth micron era," presented at International Electron Devices Meeting 1998. Technical Digest. San Francisco, CA, 1998.
- [2] X. Huang, W.-C. Lee, C. Kuo, D. Hisamoto, L. Chang, J. Kedzierski, E. Anderson, H. Takeuchi, Y.-K. Choi, K. Asano, V. Subramanian, T.-J. King, J. Bokor, and C. Hu, "Sub 50-nm FinFET: PMOS," presented at International Electron Devices Meeting 1999. Technical Digest. Washington, DC, 1999.
- [3] N. Lindert, L. L. Chang, Y. K. Choi, E. H. Anderson, W. C. Lee, T. J. King, J. Bokor, and C. M. Hu, "Sub-60-nm quasi-planar FinFETs fabricated using a simplified process," *IEEE Electron Device Letters*, vol. 22, pp. 487-489, 2001.
- [4] D. M. Fried, E. J. Nowak, J. Kedzierski, J. S. Duster, and K. T. Komegay, "A Fin-type independent-double-gate NFET," presented at 61st Device Research Conference. Salt Lake City, UT, 2003.
- [5] L. Mathew, Y. Du, A.-Y. Thean, M. Sadd, A. Vandooren, C. Parker, T. Stephens, R. Mora, R. Rai, M. Zavala, D. Sing, S. Kalpat, J. Hughes, R. Shimer, S. Jallepalli, G. Workman, W. Zhang, J. G. Fossum, B. E. White, B. Y. Nguyen, and

- J. Mogab, "CMOS Vertical Multiple Independent Gate Field Effect Transistor (MIGFET)," presented at 2004 IEEE International SOI Conference. Charleston, SC, 2004.
- [6] E. J. Nowak, B. A. Rainey, D. M. Fried, J. Kedzierski, M. Jeong, W. Leipold, J. Wright, and M. Breitwisch, "A functional FinFET-DGCMOS SRAM cell," presented at IEEE International Electron Devices Meeting. San Francisco, CA, 2002.
- [7] T. Park, H. J. Cho, J. D. Choe, S. Y. Han, S. M. Jung, J. H. Jeong, B. Y. Nam, O. I. Kwon, J. N. Han, H. S. Kang, M. C. Chae, G. S. Yeo, S. W. Lee, D. Y. Lee, D. Park, K. Kim, E. Yoon, and J. H. Lee, "Static noise margin of the full DG-CMOS SRAM cell using bulk FinFETs (Omega MOSFETs)," presented at IEEE International Electron Devices Meeting 2003. Washington, DC, 2003.
- [8] R. V. Joshi, R. Q. Williams, E. Nowak, K. Kim, J. Beintner, T. Ludwig, I. Aller, and C. Chuang, "FinFET SRAM for high-performance low-power applications," presented at Proceedings of the 34th European Solid-State Device Research Conference. Leuven, Belgium. 21-23 Sept. 2004, 2004.
- [9] P. Tai-Su, C. Hye Jin, C. Jeong Dong, H. Sang Yeon, P. Donggun, K. Kinam, E. Yoon, and L. Jong-Ho, "Characteristics of the full CMOS SRAM cell using body-tied TG MOSFETs (bulk FinFETs)," *IEEE Transactions on Electron Devices*, vol. 53, pp. 481-7, 2006.
- [10] SOITEC: <http://www.soitec.com>.
- [11] S. M. Sze, *Physics of Semiconductor Devices*, 2 ed: Wiley-Interscience, 1981.
- [12] "QM CV Simulator," <http://www-device.eecs.berkeley.edu/qmcv/index.shtml>.

- [13] T. J. King, J. R. Pfister, and K. C. Saraswat, "A variable-work-function polycrystalline-Si<sub>1-x</sub>Ge<sub>x</sub> gate material for submicrometer CMOS technologies," *IEEE Electron Device Letters*, vol. 12, pp. 533-5, 1991.
- [14] T.-J. King, J. P. McVittie, K. C. Saraswat, and J. R. Pfister, "Electrical properties of heavily doped polycrystalline silicon-germanium films," *IEEE Transactions on Electron Devices*, vol. 41, pp. 228-32, 1994.
- [15] Futurrex, "<http://www.futurrex.com>."
- [16] <http://microlab.berkeley.edu/labmanual/>, "UC Berkeley Microfabrication Facility Lab Manual."

## 6.5 Appendix : Process Flow for FinFET-based SRAMs

Step	Process Name	Process Specification	Equipment	Comment
1.00	SOI Wafers	6 inch prime SOI wafers and test SOI wafers		T <sub>si</sub> = 100nm
1.01	Labeling	SOI test FM 1-2, SOI prime = FD 1-6		
1.02	SOI thickness measurement	all wafers	nanoduv	T <sub>BOX</sub> = 400nm
<b>Make poly-Si on oxide bulk test wafers</b>				
1.03	BOX formation	2WETOXA, 1050 C, 47 min	Tystar2	4000 A
1.04	Poly-Si deposition	Tystar 19, 600C/100sccm SiH4/300 mT/ 7min	Sopra	500 A
<b>Body thinning for SOI wafers (1wet ox + 1dry ox)</b>				
1.05	precleaning	piranha, 120C, 10min	sink6	
1.06	wet oxidation test	2WETOXA, 900C, 35min, 840A target	tystar2	
1.06	Measurement	Tox	nanoduv	836 A
1.07	precleaning	piranha, 120C, 10min	sink6	
1.08	wet oxidation real	2WETOXA, 850C, ??min, 1000A target	tystar2	
1.09	oxide removal	10:1 HF, 6min, 1500A target (50% O/E)	sink6	
1.10	SOI thickness measurement	if SOI thickness is still too thick, repeat wet ox and wet etch process until we have the target SOI thickness (50nm)	nanoduv	BOX = 400nm, all wafers
<b>2.00 Prealignment Marks Formation</b>				
2.01	Prealignment Marks	Coating(HMDS/Shibley UV 210/ 0.4um/Soft bake 130C 60s) Exposure (30mJ/-0.0um) Develop(PEB 130C, 60s/LDD-26W, 45s/No Hard bake)	svgcoat6 asm1 svgdev6	(#1/#2/#1)  (#1/#1/#9)
2.02	Align Key D/E	13mT/200Ws/40Wb/100CF4/75 sec (FT-8, and all remaining)  Poly etching rate 1120 A/min, Oxide etch rate - 960 A/min	lam5	Si & Box trench ~120nm EBR ring etched in SOI wafers
2.03	Ashing	3.75T/500W/250C/45% O2/ 1min30sec	matrix	
2.04	Post Cleaning	Piranha, 120C, 10min	sink8	
2.05	Precleaning	Piranha, 120C, 10min	sink6	
2.06	Thermal oxide	2DRYOXA, 850 C, 13min 30sec	Tystar2	55 A
2.07	HTO deposition	9VHTOA, 15min, 90 N2O, 18 DCS, 300 mT, 800 C	tystar9	55A
2.08	Nitride deposition	9SNITA, 4min 45 sec	tystar10	209 A/sopra
2.09	HTO deposition	9VHTOA, 52min, 90 N2O, 18 DCS, 300 mT, 800 C	tystar9	201 A/sopra
2.10	Measurement	HTO thickness on Si dummy	sopra	
<b>3.00 Active Layer (Fin) Formation</b>				
3.01	Fin lithography	Shibley UV 210/ 0.4um/Soft bake 130C 60s Exposure Develop(PEB 130C, 60s/LDD-26W, 45s/No Hard bake)  Hard Bake - 140 C/30sec + UV light	svgcoat6 asm1 svgdev6 uvbake	(#1/#1/#9)
3.02	Inspection	CD	leo	
3.03	PR trimming	O2 ashing (Low power)	technics-c	repeat until getting target line width.
3.04	Inspection	CD	leo	
3.05	Fin Hard Mask D/E	BT - 13mT/200Ws/40Wb/100CF4/EPD+20%	lam5	
3.06	Polymer removal	(100:1) HF, 15sec	sink7	
3.07	Ashing	3.75T/400W/200C/45% O2/ 1min30sec	matrix	
3.08	Si Fin D/E	BT - 13mT/200Ws/40Wb/100CF4/10s ME - 15mT/300Ws/150Wb/50Cl2/150HBr/EPD OE - 15mT/250Ws/120Wb/5O2/200HBr/20sec	lam5	

3.09	Post Cleaning	Piranha, 120C, 10min	sink8	
3.10	Inspection	CD & Alignment	leo	
3.11	Measurement	BOX Thickness	nanoduv	
3.12	Precleaning	Piranha, 120C, 10min	sink6	
3.13	Sacrificial oxidation	Dry oxidation, 900C, 3min/Post N2 anneal 900C 20min	tystar1	Tox = 3nm
3.14	Tox measurement	Sacrificial oxide thickness measurement	sopra	
<b>4.00 Gate Formation</b>				
4.01	Precleaning	Piranha, 120C, 10min (25:1) HF, 30sec	sink6 sink6	
4.02	Gate Oxidation	Dry, O2, 750C, 13min/Post N2 anneal 900C 20min	tystar1	2~2.5nm
4.03	Measurement	thin oxide Thickness	sopra	
4.04	In-situ p <sup>+</sup> SiGe deposition	SELDEPC, p <sup>+</sup> Si <sub>0.35</sub> Ge <sub>0.65</sub> 150nm (No time delay)	tystar19	
4.05	LTO deposition	11SULTOA, 8min, 150nm	tystar11	
4.06	Measurement	prg#1, LTO thickness on Si dummy	nanoduv	
4.07	Gate lithography	BARC coating, 207 C/1min hard bake Shipley UV 210 .6um/Soft bake 130C 60s Exposure (27&30mJ/-0.2um) Develop(PEB 130C, 60s/LDD-26W, 45s/No Hard bake)	svgcoat6 svgcoat6 asml svgdev6	prog (#1/#1/#1) Negative defocus prog (#1/#1/#9)
4.08	Inspection	CD	leo	
4.09	PR trimming	O2 ashing (30W power)	technics-c	repeat until getting target line width.
4.10	Inspection	CD	leo	
4.11	Gate Hard Mask D/E	13mT/200Ws/40Wb/100CF4/EPD+30%	lam5	100nm - 55 sec + 15 sec OE
4.12	Polymer removal	(100:1) HF, 10sec	sink7	
4.13	Ashing	3.75T/400W/200C/45% O2/ 1min30sec	matrix	
4.14	p <sup>+</sup> SiGe Gate D/E	13mT/200Ws/40Wb/100CF4/10s 12mT/300Ws/150Wb/50Cl2/150HBr/EPD 15mT/250Ws/120Wb/5O2/200HBr/25sec	lam5	
4.16	Post Cleaning	Piranha, 120C, 10min	sink8	
4.17	Inspection	CD & Alignment	leo	
4.18	Measurement	BOX Thickness	nanoduv	
<b>5.00 Gate sidewall Spacer Formation</b>			<b>Single spacer</b>	
5.01	Precleaning	Piranha, 120C, 10min	sink6	
5.02	LTO deposition	11SULTOA, 1sec,30nm	tystar11	300 A
5.03	Measurement	LTO Thickness	nanoduv	
5.04	Gate Sidewall spacer Etch	200 mT, 500W, Ar=120 sccm, CF4:CHF3 = 10:50 sccm	Centura-mxp	oxide : Poly SiGe etch selectivity ~ 4:1
<b>6.00 n<sup>+</sup> &amp; p<sup>+</sup> S/D Formation</b>				
6.01	p <sup>+</sup> S/D mask (Nsel)	Coating(HMDS/Shipley UV 210 .4um/Soft bake 130C 60s) Exposure (30mJ/-0.2um) Develop(PEB 130C, 60s/LDD-26W, 45s/No Hard bake)	svgcoat6 asml svgdev6	(#1/#2/#1)  (#1/#1/#9)
6.02	Hard Bake	Hard Bake - 140 C/30sec + UV light	uvbake	
6.03	n <sup>+</sup> S/D IIP	Phosphorus/5x10 <sup>15</sup> cm-2/30 keV/0degree	Implanter	Core systems Inc.
6.04	Resist Strip	3.75T/400W/200C/45% O2/ 1min30sec	matrix	
6.05	Post Cleaning	Piranha, 120C, 10min	sink8	
6.06	p <sup>+</sup> S/D mask (Psel)	Coating(HMDS/Shipley UV 210 .9um/Soft bake 130C 60s) Exposure Develop (PEB 130C, 60s/LDD-26W, 45s/No Hard bake)	svgcoat6 asml svgdev6	(#1/#2/#1)  (#1/#1/#9)
6.07	Hard Bake	120C, 30min	UV bake	
6.08	p <sup>+</sup> S/D IIP	Boron/5x10 <sup>15</sup> cm-2/10 keV/0degree	Implanter	Core systems Inc.



6.09	Resist Strip	3.75T/500W/250C/45% O2/ 1min30sec	matrix	
6.10	Post Cleaning	Piranha, 120C, 10min	sink8	
6.11	Pre cleaning	Piranha, 120C, 10min	sink6	
6.12	S/D Recrystallization	Furnace anneal, N2, 600 C, 4 hrs	Tystar2	
6.12	S/D activation	RTA, N2, 900 C, 10s	Heatpulse3	Low thermal budget to avoid B penetration
<b>7.00 Gate Planarization</b>				
7.01	Cap LTO deposition	11SULTOA, 450C, 2min, 50nm	Tystar11	
7.02	Planarizing Coating	PC3-700 planarizing coating (3000rpm/40 sec)	svgcoat6	
7.02	Hard Bake	200 C, 2min to reflow the coating	svgdev6	6800 A, nanoduv prog #10, R.I. = 1.6
7.03	Coating Etch-Back	Resist E/B:TP=200W,BP=40W,15mT,CF4:O2=100:20 sccm	Lam5	PC3-700: oxide etch selectivity ~ 2:1
7.04	Inspection	SEM Inspection to check that the top of the gate hard mask is just exposed, if not repeat step 7.03	Leo	
7.06	Gate Hard mask Oxide Etch	200 mT, 500W, Ar:CHF3 = 120:60 sccm	Centura-mxp	oxide : Poly Si etch selectivity ~ 100:1
7.07	Planarizing Coating	3.75T/500W/250C/45% O2/ 1min30sec	matrix	
<b>8.00 Selective Gate Separation etch</b>				
8.01	Inverse active mask	Shibley UV 210 .6um/Soft bake 130C 60s Exposure (14 mJ) Develop(PEB 130C, 60s/LDD-26W, 45s/No Hard bake)	svgcoat6 asml svgdev6	prog (#1/#1/#1) prog (#1/#1/#9)
8.02	Poly-SiGe gate separation etch	BT : TP=200W,BP=40W,I3mT,CF4=100,15sccm ME : TP=300W,BP=150W,I5mT, Cl2:HBr=50:150, Timed	Lam5	
8.03	Post cleaning	Piranha, 120°C, 20min	sink7	
8.04	Inspection	SEM Inspection	Leo	Gate separation etch
<b>9.00 Contacts and Metallization</b>				
9.01	Precleaning	Piranha, 120C, 10min	sink6	
9.02	LTO deposition	11SULTOA, 450C, 8min, 150nm	tystar11	
9.03	Measurement	LTO thickness	nanoduv	
9.04	Contact Mask Photo	Coating(HMDS/Shibley UV 210 .9um/Soft bake 130C 60s) Exposure Develop(PEB 130C, 60s/LDD-26W, 45s/No Hard bake)	svgcoat6 asml svgdev6	(#1/#2/#1) (#1/#1/#9)
9.05	Hard Bake	120C, 30min	vwr	
9.06	Contact Etch (D/E + W/E)	Decide etch amount later (depends on LTO thickness on S/D, Gate)	MxP, sink8	better to do descum before W/E
9.07	Ashing	3.75T/400W/200C/45% O2/ 1min30sec	matrix	
9.08	Post Cleaning	Piranha, 120C, 10min	sink8	
9.11	precleaning	Piranha, 120C, 10min	sink6	
9.12	Al Deposition	Ar:399cc, 6mT, 15cm.min, one pass, 450 nm	Novellus	use back-sputtering
9.13	Metal Mask	BARC coating Coating(Shibley UV 210 .9um/Soft bake 130C 60s) Exposure (30mJ/-0.2um) Develop(PEB 130C, 60s/LDD-26W, 45s/No Hard bake)	svgcoat6 svgcoat6 asml svgdev6	
9.14	UV Bake	Hard Bake - 140 C/30sec + UV light	uvbake	
9.15	Al Etch	Al etchant, manual end point detection with eye	sink8	
9.16	Resist Strip	3.75T/400W/200C/45% O2/ 1min30sec	matrix	
9.17	DI rise	3 cycle rinse	sink8	
9.18	Sintering	VSINT400, 400 C, 30 min, N2:H2 = 10:1	Tylan 13	

# Chapter 7 : Conclusions

## 7.1 Summary

The silicon-based microelectronics industry has been growing rapidly for the past four decades with the continual shrinking of transistor dimensions following Moore's law of scaling. Unfortunately, fundamental physical limits have heralded the end of conventional linear scaling of transistor dimensions, and a new era of MOSFET scaling constrained by power dissipation and process-induced variations is already here. Fundamental changes in device architecture may be necessary to continue scaling trends with UTB-FETs and FinFETs emerging as leading contenders. These devices exhibit excellent control of SCE needed to continue  $L_G$  scaling and offer improved performance and lower leakage over conventional planar bulk-Si MOSFETs. This dissertation has addressed many of the key scaling issues involved in the design and performance optimization of thin-body MOSFETs, and applications that take advantage of their projected benefits.

Given the difficulties in shrinking transistor dimensions, application-specific device optimization becomes critical for maximizing the benefits in transitioning to these new transistor designs. While the generic benefits of thin-body devices are well known, the design optimization method has not been studied in detail. In assessing the role of

thin-body MOSFETs, it is not adequate just to look at standalone device metrics, but practical issues related to manufacturability, and circuit performance implications such as power, performance and robustness to process-induced variations. In this work, this methodology has been detailed to optimize thin-body FET performance through the use of device simulation and mathematical modeling to better understand the degree of performance enhancement that can be provided by these new device structures.

Double-gate MOSFET design optimization performed to minimize circuit delay shows that DG-FETs need to have an effective channel length larger than the physical gate length for scaling into the sub-10nm  $L_G$  regime. This is the result of a tradeoff between short-channel effects and parasitic resistances and capacitances.

Back-gated thin-body MOSFETs (BG-FETs) with the capability of dynamic  $V_{TH}$  control have great promise in controlling power dissipation as well as in compensating for process-induced variations. The gate delay versus energy consumption tradeoffs study shows that adaptive  $V_{TH}$  control in BG-FETs makes them span a wider range in energy-delay space over DG-FETs, making them cost-effective and attractive single technology solutions for variable throughput applications ranging from high performance to low power.

The design of BG-FETs was further refined with the derivation of a quantum – corrected back-gate bias dependent scale length that can characterize short channel effects and thereby device scalability. It has been shown that reverse-back gate biasing improves short channel effects and can be used to improve the scalability of the BG-FET so as to make it comparable to FinFET in terms of performance while relaxing the body-thickness ( $T_{Si} \sim 2/3 L_G$ ) requirement. The buried oxide thickness for optimal delay is

shown to be about 40A for 13nm  $L_G$  device. It is also shown that back-gate biasing can be used to partially compensate for the impact of process-induced variations. There is an associated delay penalty (up to 25%) with the back-gated device arising from the additional back-gate capacitance, however, such a device provides additional design flexibility in  $V_{TH}$  control making it an attractive alternative worthy of further exploration.

Designing large SRAM arrays is getting harder due to lowered cell stability with technology scaling and increased degree of process-induced variations. Various SRAM design considerations including tradeoffs in read margin, write margin, and cell area for different FinFET based designs have been presented. In addition, a new FinFET-based SRAM cell design with dynamic feedback is shown to provide significant improvement in cell static noise margin, without area or leakage penalty. Implementing dynamic feedback in FinFET-based 4-T and 6-T SRAMs involves the integration of double-gate FinFETs and independent-gate FinFETs. Required process modules such as resist planarization, etch-back and selective gate separation have been demonstrated to enable the fabrication of these SRAM designs. The SRAM designs with dynamic feedback hold great promise to enable SRAM scaling have been transferred to other industrial fabrication facilities, including Freescale Semiconductor and LETI.

## **7.2 Suggestions for Future Research**

Planar FDSOI-devices on ultra-thin BOX have been demonstrated, but these designs are not optimal. Demonstrating the benefits of reverse back-gate biasing implemented using a well-biasing strategy for power savings and control of process-induced variations will require a) the development of a process that minimizes parasitic capacitances (self-aligned bottom gate) and resistance and b) the design of appropriate

logic and memory circuits to quantify the tradeoffs involved with the power and area overhead required to implement back gate biasing.

One of the main challenges in bringing FinFETs into manufacturing is the difficulty in reducing the external parasitic resistance. The use of thin silicon channels in FDSOI devices and FinFETs needed for control of SCE implies that these devices suffer from severe series resistance. While the use of raised source/drain regions can reduce the extension resistance, wrapped around contact technology will eventually have to be developed to maximize the performance of these devices.

The benefits of using of a mix of double-gate and independent gate FinFETs has been showcased in the case of dynamic feedback for improving noise margins in SRAM cells. The use of such a mix of devices can be extended to other logic and memory applications for power savings, simplified logic implementations, etc. and is worthy of further exploration.

### **7.3 Conclusions**

Silicon-based CMOS technology has plenty of room for continued scaling into the sub-10nm regime, but paradigm changes in device and circuit design that address power consumption and immunity to variations are needed to continue reaping the benefits of shrinking transistor dimensions. Fundamental physical limits are expected to limit  $L_G$  scaling to ~5 nm, however, it is likely that other considerations such as technology development costs and the costs of state-of-the-art semiconductor fabrication facilities needed for high-yield manufacturing will slow technology advancements, except for a handful of high-volume applications that can justify the investment. It is also likely that practical design considerations stemming from statistical fluctuations in device

parameters will slow down CMOS scaling at least for applications that require a high degree of robustness. The migration to thin-body MOSFETs is likely to happen first for low power applications such as memory rather than for logic because these MOSFET designs inherently show good control of leakage and short channel effects. Until the parasitic resistance problems associated with these devices can be minimized to meet high performance targets, their adoption for logic applications cannot be justified. With power-aware design in the presence of variations (statistical design) taking on a bigger role, extensive collaboration between circuit design, system architects and semiconductor device and process engineers will be crucial to translate the promises of these new device technologies into actual chip performance.

## Appendix - Sample simulation input files

**# Taurus-Device 13nm back-gated FDSOI NMOS with raised source/drain regions**

# Structure generation

# Enable device mode

Taurus { device }

Define (Lgate=0.013)

Define (Lgate2=\$Lgate)

Define (Lsd=0.04)

Define (Lsp=0.0119)

Define (Leff=\$Lgate)

Define (workfun\_fg=4.231)

Define (workfun\_bg=5.17)

Define (Tpoly=0.03)

Define (Tox1=0.0015)

Define (Tox2=0.004)

Define (Tsi=0.008)

Define (Tepi=0.005)

Define (Tsili=0.01)

Define (pdope=1e20)

Define (bdope=1e16)

Define (sddope=1e20)

Define (xoffset=expr(Lgate/2+Lsp-15/10000))

Define (xoffset\_qmb=expr(Lsp+Lgate/2-5/10000))

Define (sdxchar=0.004)

Define (sdychar=0.004)

# tags

Define (xmin=expr(0-Lsd-Lsp-Lgate/2))

Define (xmax=expr(Lsd+Lsp+Lgate/2))

Define (ymin=expr(0-Tox1-Tpoly-Tsi/2))

Define (ymax=expr(Tox2+Tsi/2))

Define (cont=0.005)

# Define the device size, list the regions, and specify fixed mesh lines

DefineDevice (

minX=expr(xmin), maxX=expr(xmax),

minY=expr(ymin), maxY=expr(ymax+cont),

```

Region (name=silicon1, material=silicon),
Region (name=oxideFR, material=oxide),
Region (name=oxideFL, material=oxide),
Region (name=gox1, material=nitride),
Region (name=BOX, material=oxide),
Region (name=gate1, material=electrode),
Region (name=gate2, material=electrode),
Region (name=source, material=electrode),
Region (name=drain, material=electrode),

x=$xmin, x=expr(xmin+Lsd), x=expr(0-xoffset), x=expr(0-Lgate/2), x=0nm,
x=expr(Lgate/2), x=$xoffset, x=expr(xmax-Lsd), x=$xmax,
y=$ymin, y=expr(0-Tsi/2-Tepi-Tsili), y=expr(0-Tsi/2-Tepi), y=expr(0-Tsi/2-Tox1),
y=expr(0-Tsi/2), y=0nm, y=expr(Tsi/2), y=$ymax, y=expr(ymax+cont)
)

# Define the silicon substrate region
DefineBoundary (
  region=silicon1,
  Polygon2D (
    Point (x=$xmin, y=expr(0-Tsi/2)), Point (x=$xmin, y=expr(0-Tsi/2-Tepi)),
    Point (x=expr(xmin+Lsd), y=expr(0-Tsi/2-Tepi)), Point (x=expr(xmin+Lsd),
y=expr(0-Tsi/2)),
    Point (x=expr(xmax-Lsd), y=expr(0-Tsi/2)), Point (x=expr(xmax-Lsd), y=expr(0-
Tsi/2-Tepi)),
    Point (x=expr(xmax), y=expr(0-Tsi/2-Tepi)),
    Point (x=$xmax, y=expr(0-Tsi/2)), Point (x=$xmax, y=expr(Tsi/2)), Point (x= $xmin,
y=expr(Tsi/2))
  )
)

# Define the source region
DefineBoundary (
  region=source,
  Polygon2D (
    Point (x=expr(xmin), y=expr(0-Tsi/2-Tepi)), Point (x=expr(xmin+Lsd), y=expr(0-
Tsi/2-Tepi)),
    Point (x=expr(xmin+Lsd), y=expr(0-Tsi/2-Tepi-Tsili)), Point (x=expr(xmin),
y=expr(0-Tsi/2-Tepi-Tsili))
  )
)

# Define the drain region
DefineBoundary (
  region=drain,
  Polygon2D (

```



```

    Point (x=expr(xmax), y=expr(0-Tsi/2-Tepi)), Point (x=expr(xmax-Lsd), y=expr(0-
Tsi/2-Tepi)),
    Point (x=expr(xmax-Lsd), y=expr(0-Tsi/2-Tepi-Tsili)), Point (x=expr(xmax),
y=expr(0-Tsi/2-Tepi-Tsili))
)
)
# Define the left front oxide spacer region

DefineBoundary (
    region=oxideFL,
    Polygon2D (
        Point(x=expr(xmin), y=$ymin),Point (x=expr(0-Lgate/2), y=$ymin),
        Point(x=expr(0-Lgate/2),y=expr(0-Tsi/2-Tox1)), Point(x=expr(xmin+Lsd),y=expr(0-
Tsi/2-Tox1))
        Point(x=expr(xmin+Lsd),y=expr(0-Tsi/2-Tepi-Tsili)), Point(x=expr(xmin),y=expr(0-
Tsi/2-Tepi-Tsili))
    )
)

# Define the front right oxide spacer region
DefineBoundary (
    region=oxideFR,
    Polygon2D (
        Point(x=expr(Lgate/2),y=expr(0-Tsi/2-Tox1)), Point(x=expr(Lgate/2),y=$ymin),
        Point(x=expr(xmax), y=$ymin), Point(x=expr(xmax), y=expr(0-Tsi/2-Tepi-Tsili))
        Point(x=expr(xmax-Lsd), y=expr(0-Tsi/2-Tepi-Tsili)), Point(x=expr(xmax-Lsd),
y=expr(0-Tsi/2-Tox1))
    )
)

# Define the back oxide region
DefineBoundary (
    region=BOX,
    Polygon2D (
        Point(x=expr(xmin),y=expr(Tsi/2)), Point(x=expr(xmax),y=expr(Tsi/2)),
        Point(x=expr(xmax), y=$ymax), Point(x=expr(xmin), y=$ymax)
    )
)

# Define the front gate oxide region
DefineBoundary (
    region=gox1,
    Polygon2D (
        Point(x=expr(0-Lgate/2-Lsp),y=expr(0-Tsi/2-Tox1)), Point
(x=expr(Lgate/2+Lsp),y=expr(0-Tsi/2-Tox1)),

```

```

    Point(x=expr(Lgate/2+Lsp), y=expr(0-Tsi/2)), Point(x=expr(0-Lgate/2-Lsp),y=expr(0-
Tsi/2))
  )
)

# Define the front electrode gate region
DefineBoundary (
  region=gate1,
  Polygon2D (
    Point (x=expr(0-Lgate/2), y=expr(ymin)), Point (x=expr(Lgate/2), y=expr(ymin)),
    Point (x=expr(Lgate/2), y=expr(0-Tox1-Tsi/2)), Point (x=expr(0-Lgate/2), y=expr(0-
Tox1-Tsi/2))
  )
)

# Define the back electrode gate region
DefineBoundary (
  region=gate2,
  Polygon2D (
    Point (x=expr(xmin), y=expr(ymax)), Point (x=expr(xmax), y=expr(ymax)),
    Point (x=expr(xmax), y=expr(ymax+cont)), Point (x=expr(xmin), y=expr(ymax+cont))
  )
)

QuantumBox ( name=channelBox,
  minX=expr(0-xoffset_qmb), maxX=expr(xoffset_qmb),
  minY=expr(0-Tsi/2-Tox1/2), maxY=expr(Tsi/2+Tox1/2),
  # minY=expr(0-Tsi/2), maxY=expr(Tsi/2),
  sliceDirection=Y,
  useBoundaryNodes=true,
  ymesh(depth=expr(Tox1/2), h1=2A, h2=0.5A),
  ymesh(depth=expr(Tsi), h1=2A, h2=4A),
  ymesh(depth=expr(Tox1/2), h1=0.5A, h2=2A),
  ElectronSchrodinger( NLadders=2, NSubbands=4),
  HoleSchrodinger( NLadders=2, NSubbands=4)
  storeWavefunctions=true
)

# Substrate Doping: P-type Uniform
Profile (name=Ptype, region=silicon1, Uniform (value=$bdope))

# Source doping: N-type Gaussian
Profile (
  name=Ntype, region=silicon1, addtoexisting=true
  Gauss (
    peakValue=$sddope, sigma=$sdxchar, lateralRatio=1,

```

```

    Polygon (Point (x=expr(0-xoffset), y=expr(0-Tsi/2-Tepi)), Point(x=expr(0-xoffset),
y=expr(Tsi/2)),
    Point(x=$xmin, y=expr(Tsi/2)), Point(x=$xmin, y=expr(0-Tsi/2-Tepi)))
)
)

```

```

# Drain gaussian doping: N-type Gaussian

```

```

Profile (
  name=Ntype, region=silicon1, addtoexisting=true
  Gauss (
    peakValue=$sd dope, sigma=$sd xchar, lateralRatio=1,
    Polygon ( Point (x=expr(xoffset), y=expr(0-Tsi/2-Tepi)), Point (x=$xoffset
,y=expr(Tsi/2)),
    Point (x=$xmax ,y=expr(Tsi/2)),Point (x=$xmax ,y=expr(0-Tsi/2-Tepi)))
  )
)

```

```

# Initial coarse regrid

```

```

Regrid (gridProgram=taurus, meshSpacingX=expr(Lgate/6),
meshSpacingY=expr(Lgate/6))

```

```

# Regrid in channel

```

```

Regrid (
  gridProgram=taurus, meshspacingy=expr(Tsi/20), meshspacingx=expr(Lgate/16.5),
  minX=expr(xmin+Lsd), maxX=expr(xmax-Lsd), minY=expr(0-Tsi/2-Tox1/0.9),
  maxY=expr(Tsi/2+Tox1/1.8)
)

```

```

#Regrid (

```

```

# gridProgram=taurus, meshspacingy=expr(Tox2/8), meshspacingx=expr(Lgate/20),
# minX=expr(xmin), maxX=expr(xmax), minY=expr(0-Tsi/2+Tox1/1.8),
maxY=expr(Tsi/2+Tox2/0.9)
#)

```

```

# Regrid in source electrode

```

```

Regrid (
  gridProgram=taurus, meshspacingy=expr(Tsi/7.5), meshspacingx=expr(Lgate/8.25),
  minX=expr(xmin), maxX=expr(xmin+Lsd), minY=expr(0-Tsi/2-Tepi),
  maxY=expr(Tsi/2)
)

```

```

# Regrid in drain electrode

```

```

Regrid (
  gridProgram=taurus, meshspacingy=expr(Tsi/7.5), meshspacingx=expr(Lgate/8.25),
  minX=expr(xmax-Lsd), maxX=expr(xmax), minY=expr(0-Tsi/2-Tepi),
  maxY=expr(Tsi/2)
)

```

```

)

# Regrid in BOX
Regrid (
  gridProgram=taurus, meshspacingy=expr(Tox2/8), meshspacingx=expr(Lgate/11),
  minX=expr(xmin+Lsd), maxX=expr(xmax-Lsd), minY=expr(Tsi/2), maxY=expr(ymax)
)

# Regrid in back electrode
Regrid (
  gridProgram=taurus, meshspacingy=expr(cont/2), meshspacingx=expr(Lgate/11),
  minX=expr(xmin), maxX=expr(xmax), minY=expr(ymin), maxY=expr(ymin+cont)
)

# Zero-carrier solve at equilibrium
Symbolic (carriers=0)
Solve {}

# Regrid on potential
#Regrid (
# gridProgram=taurus, meshSpacing=0.5nm,
# Criterion (name=ElectricPotential, delta=.1, type=linear)
#)

# Regrid to desired grading factor and maximum element angle
#Regrid (
# gridProgram=pm, region=silicon1,
# gradingFactor=2.01, MaximumAngle (value=90)
#)

# Redo zero-carrier solve
#Solve {}

# Save structure
Save (meshfile=nfin.tdf)

# Select Lombardi mobility model
Physics(
  Global(
    Global(
      FermiStatisticsActive=true
      DirectTunneling(
        #PostProcessing=false,
        TCMethod=Gundlach
        #, GridSpacing=5A, MaxDistance=100A,
        CBET( Active=true, Barrier(UseAffinity=true)),

```

```

#VBHT( Active=true, Barrier(UseAffinity=true)),
#VBET( Active=true, ConductionBarrier(UseAffinity=true),
#ValenceBarrier( UseAffinity=false, Height=4.30 )
# )
)
)
)
)
Nitride(
Poissons(
    ElectronQMMModel (
        active=false,
        qmmodel=Schrodinger,
        #Schrodinger(
        # tailActive=true, tailModel=tail3)
    )
)
)
)
Silicon(
Poissons(
    Bandgap
    (
        BGNActive=true,
        BGNModel=Slotboom
        BandgapNarrowing (v0=6.92e-3 n0=1.3e17 con=0.5)
    )
    ElectronQMMModel (
        active=true,
        qmmodel=Schrodinger,
        #Schrodinger(
        # tailActive=true, tailModel=tail3)
    )
    HoleQMMModel(
        active=true,
        qmModel=Schrodinger,
        # Schrodinger(
        # scaleMxy=true, tailActive=true, tailModel=tail3,
        # )
    )
)
)
ElectronContinuity(
RecombinationWithTunneling()
Recombination
(
    SRHRecombination(
    ElectronLifeTime(

```

```

        Cdependent=True
    )
    HoleLifeTime(
        Cdependent=True
    ))
    AugerRecombination
)
ImpactIonizActive=false, ElectronImpactIonization ( PostProcessing=false)
BTBTunneling( BTBTActive=True, BTBTModelType=3 )
Mobility(
    LowFieldMobility(
        #ConModelActive=True,
        #CCSModelActive=True,
        #CCSModel=KlaassenModel,
        SurfModelActive=True,
        SurfModel=LombardiSurfaceModel,
    )
    HighFieldMobilityActive=True,
    HighFieldMobility (
        HighFieldModel=CaugheyThomasModel,
        #HighFieldModel=HanschModel,
    )
)
)
)
HoleContinuity(
    ImpactIonizActive=false,
    HoleImpactIonization( PostProcessing=false)
    Mobility(
        LowFieldMobility(
            #ConModelActive=True,
            #CCSModelActive=True,
            #CCSModel=KlaassenModel,
            SurfModelActive=True,
            SurfModel=LombardiSurfaceModel,
        )
        #highFieldMobility=true
        HighFieldMobilityActive=True,
        HighFieldMobility (
            HighFieldModel=CaugheyThomasModel,
        )
    )
)
)
)
)
)
# Set gate workfunction

```

```

Contact (name=gate1, workfunction=$workfun_fg)
Contact (name=gate2, workfunction=$workfun_bg)
Contact (name=source, con.res=2e-8)
Contact (name=drain, con.res=2e-8)

Symbolic (carriers=2)

# Zero bias, Poisson-only solve
Solve{ couple(iterations=25) {Poissons} }
#Solve{ couple(iterations=25) {Poissons, electroncontinuity} }
Solve{ couple(iterations=20) {Poissons, electroncontinuity, holecontinuity} }
# Do IdVg simulation at Vd=50mV
# Set drain to 50mV

#Ramp (
#Voltage (electrode=drain, startValue=0.0, vStep=0.45, nSteps=2)
#)

Save(MeshFile=nfin1a.tdf)

## VBG = 0V #####
Ramp (
Voltage (electrode=gate2, startValue=0.0, vStep=-0.4, nSteps=2)
)
Save(MeshFile=nfin1b.tdf)

Solve{
acanalysis( logfile=nfin_cv.data, frequency=1e5, terminal(gate1),
  ContactVoltage(electrode=gate1, startvalue=0, endValue=1.0, nsteps=10)
)}
Save(MeshFile=nfincv.tdf)
Ramp (
Voltage (electrode=gate1, startValue=0.0, vStep=0.1, nSteps=9)
#Voltage (electrode=gate2, startValue=0.0, vStep=0.1, nSteps=9)
)

Save(MeshFile=nfin1c.tdf)

Ramp (
Voltage (electrode=drain, startValue=0.65, vStep=-0.3, nSteps=2)
)

Ramp (
Voltage (electrode=gate1, startValue=0.9, vStep=-0.1, nSteps=9)
#Voltage (electrode=gate2, startValue=0.9, vStep=-0.1, nSteps=9)
)

```

## # Taurus-Device 6-T FinFET SRAM mixed-mode setup

```
Taurus {device}
# Read in the device mesh files
DefineDevice (name=n_pdn, MeshFile=n110_hi_pdn.tdf, PhysicsFile=n110_phy)
DefineDevice (name=n_acc, MeshFile=n110_hi.tdf, PhysicsFile=n110_phy)
DefineDevice (name=p_load, MeshFile=p110_hi.tdf, PhysicsFile=p110_phy)

#netlist
DefineCircuit (name=sram,
netlist(
vdd(n1=vdd, n0=0, value=0),
vsnb(n1=snb, n0=0, value=0),
vwl(n1=wl, n0=0, value=0),
vbl(n1=bl, n0=0, value=0),
PNMOS1 ( source=0, drain=sn , gate1=snb, gate2=snb, device=n_pdn, area=.03),
PPMOS1 ( source=vdd, drain=sn , gate1=snb, gate2=snb, device=p_load, area=.03),
PNMOS2 ( source=sn, drain=bl , gate1=wl, gate2=wl, device=n_acc, area=.03),
)

#Set initial node values
nodeset(
    V( num=vdd, value=0 ),
    V( num=wl, value=0 ),
    V( num=bl, value=0 ),
    V( num=sn, value=0 )
)

#Solve
symbolic (carriers=0)
solve{init}

symbolic (carriers=2)
solve{ }
#Solve{
circuit_ramp(VoltageSource(
    element=vbl,startvalue=0,endValue=1,nsteps=2) )
    { couple(iterations=10,LinearSolver=direct)
      { Poissons,ElectronContinuity,HoleContinuity }
    }
circuit_ramp(VoltageSource(
    element=vwl,startvalue=0,endValue=1,nsteps=4) )
    { couple(iterations=10,LinearSolver=direct)
      { Poissons,ElectronContinuity,HoleContinuity }
```



```

}
circuit_ramp(VoltageSource(
    element=vdd,startvalue=0,endValue=0.5,nsteps=2) )
    { couple(iterations=10,LinearSolver=direct)
      { Poissons,ElectronContinuity,HoleContinuity }
    }
circuit_ramp(VoltageSource(
    element=vdd,startvalue=0.6,endValue=1.0,nsteps=2) )
    { couple(iterations=10,LinearSolver=direct)
      { Poissons,ElectronContinuity,HoleContinuity }
    }
}
circuit_ramp(VoltageSource(
    element=vsnb,startvalue=0,endValue=.32,nsteps=4) )
    { couple(iterations=10,LinearSolver=direct)
      { Poissons,ElectronContinuity,HoleContinuity }
    }
}
circuit_ramp(VoltageSource(
    element=vsnb,startvalue=0.36,endValue=0.45,nsteps=3) )
    { couple(iterations=10,LinearSolver=direct)
      { Poissons,ElectronContinuity,HoleContinuity }
    }
}
circuit_ramp(VoltageSource(
    element=vsnb,startvalue=0.47,endValue=0.55,nsteps=4) )
    { couple(iterations=10,LinearSolver=direct)
      { Poissons,ElectronContinuity,HoleContinuity }
    }
}
circuit_ramp(VoltageSource(
    element=vsnb,startvalue=0.6,endValue=0.84, nsteps=3) )
    { couple(iterations=10,LinearSolver=direct)
      { Poissons,ElectronContinuity,HoleContinuity }
    }
}
}
circuit_ramp(VoltageSource(
    element=vsnb,startvalue=0.87,endValue=0.9,nsteps=1) )
    { couple(iterations=10,LinearSolver=direct)
      { Poissons,ElectronContinuity,HoleContinuity }
    }
}
circuit_ramp(VoltageSource(
    element=vsnb,startvalue=0.95,endValue=1.0,nsteps=1) )
    { couple(iterations=10,LinearSolver=direct)
      { Poissons,ElectronContinuity,HoleContinuity }
    }
}
}

```